SANDIA REPORT
SAND2008-0878
Unlimited Release
Printed February 2008

Innovative Solar Thermochemical Water Splitting

Richard B. Diver, Nathan P. Siegel, Timothy A. Moss, James E. Miller, Lindsey Evans, Roy E. Hogan, Mark D. Allendorf, John N. Stuecker, Darryl L. James

Prepared by
Sandia National Laboratories
Albuquerque, New Mexico 87185 and Livermore, California 94550

Sandia is a multiprogram laboratory operated by Sandia Corporation,
a Lockheed Martin Company, for the United States Department of Energy's
National Nuclear Security Administration under Contract DE-AC04-94AL85000.

Issued by Sandia National Laboratories, operated for the United States Department of Energy by Sandia Corporation.

Available to DOE and DOE contractors from
U.S. Department of Energy
Office of Scientific and Technical Information
P.O. Box 62
Oak Ridge, TN 37831

Telephone: (865) 576-8401
Facsimile: (865) 576-5728
E-Mail: reports@adonis.osti.gov
Online ordering: http://www.osti.gov/bridge

Available to the public from
U.S. Department of Commerce
National Technical Information Service
5285 Port Royal Rd.
Springfield, VA 22161

Telephone: (800) 553-6847
Facsimile: (703) 605-6900
E-Mail: orders@ntis.fedworld.gov
Online order: http://www.ntis.gov/help/ordermethods.asp?loc=7-4-0#online

SAND2008-0878
Unlimited Release
Printed February, 2008

Innovative Solar Thermochemical Water Splitting

Richard B. Diver
Nathan P. Siegel
Timothy A. Moss
Solar Technologies Department 6337
Sandia National Laboratories
Albuquerque, NM 87185-1127

James E. Miller
Lindsey Evans
Ceramic Processing & Inorganic Department 1815
Sandia National Laboratories
Albuquerque, NM 87185-1349

Roy E. Hogan
Thermal and Reactive Processes Department 1516
Sandia National Laboratories
Albuquerque, NM 87185-0836

Mark D. Allendorf
Microfludics Department 8324
Sandia National Laboratories
Livermore, CA 04550-9291

John N. Stuecker
Robocasting Enterprises
4501 Bogan #4
Albuquerque, NM 87109

Darryl L. James
Texas Tech University
Department of Mechanical Engineering
Lubbock, TX 79409

Abstract

Sandia National Laboratories (SNL) is evaluating the potential of an innovative approach for splitting water into hydrogen and oxygen using two-step thermochemical cycles. Thermochemical cycles are heat engines that utilize high-temperature heat to produce chemical work. Like their mechanical work-producing counterparts, their efficiency depends on operating temperature and on the irreversibility of their internal processes. With this in mind, we have invented innovative design concepts for two-step solar-driven thermochemical heat engines based on iron oxide and iron oxide mixed with other metal oxides (ferrites). The design concepts utilize two sets of moving beds of ferrite reactant material in close proximity and moving in opposite directions to overcome a major impediment to achieving high efficiency -- thermal recuperation between solids in efficient counter-current arrangements. They also provide inherent separation of the product hydrogen and oxygen and are an excellent match with high-concentration solar flux. However, they also impose unique requirements on the ferrite reactants and materials of construction as well as an understanding of the chemical and cycle thermodynamics.

In this report the Counter-Rotating-Ring Receiver/Reactor/Recuperator (CR5) solar thermochemical heat engine and its basic operating principals are described. Preliminary thermal efficiency estimates are presented and discussed. Our ferrite reactant material development activities, thermodynamic studies, test results, and prototype hardware development are also presented.

ACKNOWLEDGMENTS

This work is supported by the U.S. Department of Energy under contract DE-AC04-94-AL85000. The authors would like to acknowledge the contributions of JJ Kelton, Daniel Ray, and Blaine Emms in the restoration of the NSTTF solar furnace and CR5 fabrication and the contributions of Barry Boughton for numerical analysis support. We would also like to acknowledge Steve Lockwood for scaling-up production of the ferrite reactant. We are most grateful to the Sandia LDRD committee for enabling this exciting opportunity.

TABLE OF CONTENTS

INTRODUCTION

Solar and nuclear energy are the world's only viable long-term energy options and hydrogen production from these sources is potentially an environmentally advantageous, long-term alternative to fossil fuels. As a result, hydrogen research is currently receiving a great deal of interest. [1] Solar power is clean and abundant and is technically capable of supplying all of the world energy needs utilizing a few per cent of the world's desert area. Solar thermal power concentrates direct solar radiation to produce high-temperature thermal energy, which can be used in a heat engine or other thermal applications. Parabolic dish and high-performance power tower systems are capable of supplying high-temperature thermal energy. [2, 3] When mass-produced, concentrating solar power systems can be cost competitive with conventional energy sources. [4]

Thermochemical processes for converting solar energy into hydrogen are potentially more straightforward, efficient, and lower cost than using electric power to electrolyze water. Thermochemical cycles are heat engines that utilize high-temperature heat to produce chemical work in the form of hydrogen. [5] Like their mechanical work-producing counterparts, their efficiency depends on operating temperature and the irreversibility of their internal processes. Thermochemical water-splitting cycles utilize a series of chemical reactions with the overall reaction $H_2O \rightarrow H_2 + 1/2O_2$. All of the other chemicals are recycled within the process. Hundreds of unique cycles have been proposed over the past 40 years, but substantial research has been done on only a few. [6] Most of the development has envisioned nuclear heat being used as the primary heat source. As a result, temperature limitations of approximately 1000^{o}C have resulted in most work focused on a few cycles. [7] Solar thermochemical processes offer the potential for much higher temperatures than are being considered for nuclear-based cycles.

Recent solar thermochemical research has focused on metal oxide cycles. The metal oxide cycles are attractive in that they involve fewer and less complex chemical steps than lower temperature processes, thereby resulting in less irreversibility and potentially higher cycle efficiency. The ferrite cycles utilize cyclic thermal-reduction and water-hydrolysis reactions with an iron-based metal oxide spinel to split water. They are particularly attractive because they involve a minimum number of steps and reactants; have solid-gas reactions; use non-corrosive materials; lend themselves to direct solar irradiation of the working material; and can avoid the recombination reactions and irreversibility associated with quenching needed with volatile-metal oxides such as zinc or cadmium oxides.

Iron oxide has been of interest since Nakamura described the FeO/Fe_3O_4 cycle. [8] The two steps in the FeO/Fe_3O_4 (Iron Oxide) cycle are

$$Fe_3O_4 \rightarrow 3FeO + 1/2O_2 \qquad (1)$$

$$3FeO + H_2O \rightarrow Fe_3O_4 + H_2 \quad (2)$$

Reaction (1) is the thermal reduction (TR) step. It is highly endothermic and requires temperatures of over 1600 K. Reaction (2) is the water oxidation (WO) or hydrolysis step. It is slightly exothermic and is spontaneous at ambient temperature to about 1200 K. In recent years, research has focused on mixed-metal oxides called ferrites that have a spinel crystal structure involving Fe and a second metal A (where A = Mn, Mg, Co, Zn, and/or Ni) as a way to lower the temperatures required to reduce the oxide. [9-13] Recently, Kodama et al., [14, 15] and Ishihara et al., [16] have demonstrated that dispersing the ferrite in zirconia enhances reactivity and improves reduction and hydrolysis kinetics. They have also shown that the supported materials maintain reactivity when repeatedly cycled between TR and WO reactions. Other researchers have begun to explore solar receiver/reactor designs for the ferrite cycles in which the reactant is supported on a matrix. [17, 18]

Recuperation of the sensible heat between the hydrolysis and reduction reactors is essential for high efficiency, especially for designs in which the ferrite is supported. Without recuperation, the energy required for sensible heating between the WO and TR temperatures is a substantial fraction of the energy input to the cycle. In addition, a significant amount of high quality sensible heat must be rejected from the cycle to cool the reactant material from the TR temperature to the WO temperature. The importance of recuperation on thermal efficiency for two-step Iron Oxide thermochemical cycles is discussed in Appendix A.

Until recently, metal oxide thermochemical reactors have envisioned using particles. From the point of view of receiver/reactor design the use of particles is an obvious choice. Nakamura [8] and Steinfeld, et al., [19] both recognized the need for recuperation in order to achieve high thermal performance. However, neither developed practical approaches to recuperate heat in metal oxide particle streams. For the recently introduced matrix supported reactor designs, there is no apparent consideration of recuperation.

As in thermal-to-mechanical work producing heat engines, such as Stirling and Ericsson cycle machines, recuperation is critical. Rather than recuperate a reactor, our approach is to reactorize a recuperator. This requires development of concepts for solid-to-solid counter-current heat exchangers and adapting them to the TR and WO reactions. This approach results in thermochemical analogs to Stirling and Ericsson cycle heat engines and provides a framework for minimizing irreversibilities. As a result, these devices are potentially efficient. However, they also place unique requirements on materials and involve numerous engineering tradeoffs. To understand and design these engines also requires an understanding of chemical and cycle thermodynamics.

THE CR5 HEAT ENGINE

To address recuperation between solids and reactor requirements for ferrite cycles, we conceived several configurations. A preferred arrangement is shown in figure 1. The Counter-Rotating-Ring Receiver/Reactor/Recuperator (CR5) uses a stack of counter-rotating rings or disks with fins along the perimeter. The fins contain the ferrite reactant, presumably on a support. Each ring rotates in the opposite direction to its neighbor at a rotational speed on the order of one RPM or less. The thickness of the reactant fins is a fraction of the thickness of the rings to permit solar flux to penetrate in depth and allow for water and products to be transported to and from the ferrite reactant material of the fins. Solar flux illuminates the fins on the stack of rings on edge along nominally 1/4 of the perimeter. The moving "volumetric absorber" has the advantage of effectively smoothing non-uniform flux distributions inherent from reflective solar concentrators. In addition, because the reactant is supported, the CR5 is compatible with variable orientations relative to gravity on parabolic dishes and their relatively higher concentration ratio compared to power towers. On the opposite side of the stack, the WO reaction takes place. The remaining half of the stack (two 1/4 sections between) is adiabatic and is utilized for counter-current recuperation occurs, primarily by thermal radiation. Equal pressures are maintained in the two reactors to minimize flow through the recuperator sections.

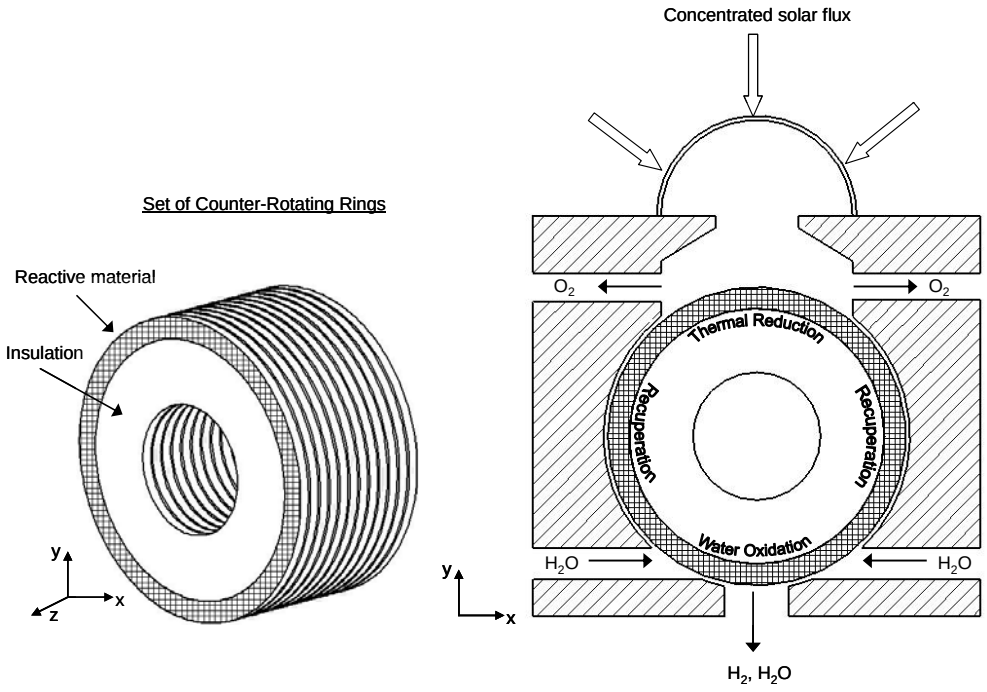

Figure 1. Schematic of the Counter-Rotating-Ring Receiver/Reactor/Recuperator (CR5).

As the oxidized ferrite material in the fins leaves the WO reactor and enters the recuperator it "sees" hotter fins leaving the TR reactor on both sides. In the recuperator it heats up as the neighboring fins moving in the opposite direction cool. In the sunlit section, the concentrated solar radiation continues to

heat the reactant fin and provides the heat of reaction for the endothermic TR oxygen-producing reaction as well as any additional sensible heating that is required. A vacuum pump removes the evolved oxygen. In the WO reactor, water vapor re-oxidizes the ferrite to produce hydrogen. Near the exit of the WO reactor, we envision directing fresh steam over the reactant fins. The lower hydrogen partial pressure from the steam over the ferrite should enable the hydrolysis reaction to proceed further by maintaining non-equilibrium conditions.

A key feature of the CR5 is that it facilitates continuous removal and sweeping of the product gases. The moving reactants and the potential of fluidically establishing isolated reaction zones allow the solid and gas products to be separated. Furthermore, by careful introduction of a sweep gas, it is possible to cause counter-current flow between the sweep gas and solid reactant. This ensures that the last environment seen by the solid reactant as it leaves the reactor is the most favorable thermodynamically for driving the reaction. The effectiveness of this approach, however, depends on fast reaction kinetics.

We envision using steam for sweeping. Nitrogen, argon, or other non-condensable gases require energy to separate and dramatically increase the pumping requirements for sub-atmospheric operation. In the WO reactor, steam oxidizes the reduced ferrites and produces hydrogen. Increasing the steam flow reduces the hydrogen partial pressure and increases the extent of reaction. With the oxidized ferrite in the TR reactor, steam is essentially inert and could be used as a sweep gas. However, we envision the use of little or no sweep gas in the TR reactor. Oxygen would be continually removed by pumping. A sweep gas results in an additional thermal parasitic load and could actually slow the TR reaction by inhibiting mass transport of product oxygen from the surface. Thermal reduction kinetic studies of Fe_3O_4 indicate that the rate of reaction is limited by gas phase mass transport of the O_2 from the surface. [19] Introducing small amounts of steam within the internal drives and/or within the recuperator is a way to counteract diffusion of product gases and mitigate crossover between the reactors.

Waste heat from the recuperator and hydrolysis reaction would be used to vaporize and preheat the water. Waste heat results from the exothermic WO reaction, recuperator inefficiencies, and sensible heat in the product hydrogen and oxygen. As in mechanical-work producing heat engines, cooling of the low-temperature step and rejection of waste heat to the environment are required.

Depending on the amount and effectiveness of recuperation, reaction extent, and/or a reduced amount of inert carrier (ZrO_2), our analyses suggest that HHV thermal efficiencies of up to about 50% are possible. The thermodynamic model also suggests that the product oxygen partial pressures need to be higher than about 0.1 atm. Otherwise, pump work becomes excessive. This means that the ferrite TR equilibrium oxygen and the WO hydrogen/steam partial pressures must be greater than 0.1 atm at operating conditions for this approach to be viable. The system model also suggests that receiver temperatures need to be less than about 2100K. The system model is described in Appendix B.

CR5 DEVELOPMENT

In addition to our system studies, SNL is also trying to identify, engineer, and characterize redox materials/supports with the best possible thermodynamic and structural characteristics to establish whether suitable materials can be developed and fielded. We are also numerically modeling various thermal and flow aspects of the CR5 and are building and plan to test a prototype CR5 device.

We have evaluated the thermodynamics of three promising iron ferrite systems based on Mg, Co, and Ni with a commercially available thermodynamic database called FactSage. The FactSage data represent the state of the art for spinel ferrites. [20] The calculations incorporate thermodynamic data for the non-ideal solid- and liquid-phase solutions that form both the ferrites and their thermal decomposition products. The results indicate that complex solution phases form in addition to the ferrite, and the zirconia support is not completely inert. Some of the iron oxide and other metals in these systems form solutions with ZrO_2, and oxide solutions with each other. We are interested in the temperature and volume-dependent oxygen partial pressures to understand what is needed to meet the conditions identified in our system studies and the potential for pumping and sweeping to increase reaction extent. We are also interested in the effect of composition on the ferrite melting point, reaction extent, and hydrogen yields. The results indicate that nickel ferrite (Fe_2NiO_4) produces the highest oxygen partial pressures relative to its melting point. Cobalt ferrite is also a good choice. See figure 2. Zinc ferrite is not of interest because of its volatility. Results from our thermodynamic studies are given in appendix C.

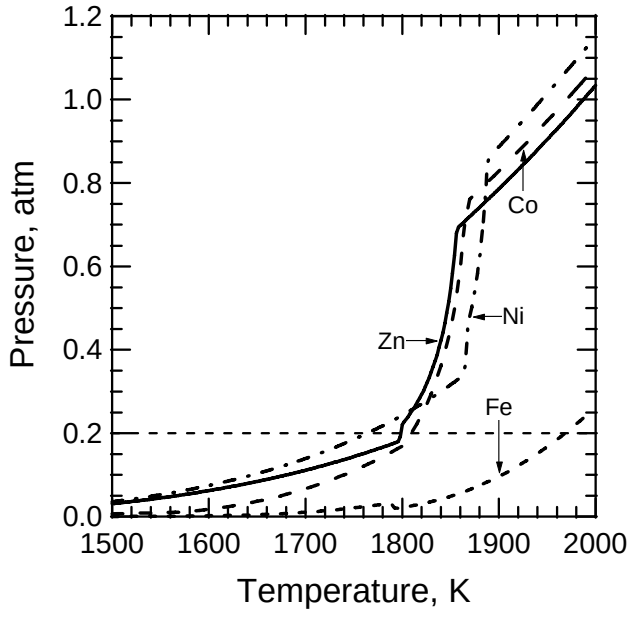

Figure 2. Equilibrium oxygen partial pressures over Ni, Co, Zn, and Fe ferrites.

The CR5 design places unique demands on materials. The ferrite fins must maintain structural integrity and high reactivity over thousands of thermal cycles and exposure to temperatures in excess of 1700 K. In addition, the design of the fins must have high surface area for gas-solid interactions and for absorption of incident solar radiation, and should have high solar absorptivity. To address some of these requirements, we are characterizing the effect of a number of material parameters on performance in a test system for cyclic TR and WO with concurrent quantification of hydrogen and oxygen evolution.

To address redox materials/supports, our approach was to start with promising mixed-metal ferrites identified in the literature and to establish an experimental capability for thermal reduction and hydrolysis of candidate material while measuring oxygen and hydrogen evolution rates. A test system used for evaluating reactant materials incorporated into a cyclic water splitting process was designed and built. The test system was designed to allow independent flow of the coupled gases argon/hydrogen and helium/oxygen without the mixing of hydrogen and oxygen under any of the test modes. The use of hydrogen or oxygen feeds is for calibrating a HP 5890 gas chromatograph (GC) equipped with a thermal conductivity detector (TCD). The argon or helium inert gas is used as a carrier for the reaction products during the oxidation or reduction phases of the cyclic water splitting reaction. Argon saturated with 80^{o}C water vapor is used in the hydrolysis (WO) reaction, and helium is used during oxygen generation (TR) reaction. The reactor is a high-temperature tube furnace, with temperature capabilities of up to 1500^{o}C and is equipped with a 1” OD by 26” long mullite tube. A line drawing of the test system is shown in figure 3.

Early in the testing we started using Robocasted samples. Robocasting is a Sandia-developed technique for free-form processing of ceramics to manufacture monolithic structures with complex three-dimensional geometries for chemical, physical, and mechanical evaluation. [21] As part of our testing we demonstrated that ferrite/zirconia mixtures can be fabricated into small three-dimensional lattice structures; hydrogen and oxygen can be produced using these monolithic structures; and structural integrity can be maintained over successive cycles. Probably because of enhanced mass transport geometries, we have been able to produce more hydrogen and oxygen at faster rates with these monolithic structures than with equivalent amounts of powders. We have also fabricated reactant fin sections for the CR5 prototype. Design objectives for the fin sections include high geometric surface area, thermal shock resistance, and allowing for light penetration. The design of these monolithic structures is being guided by our CFD studies.

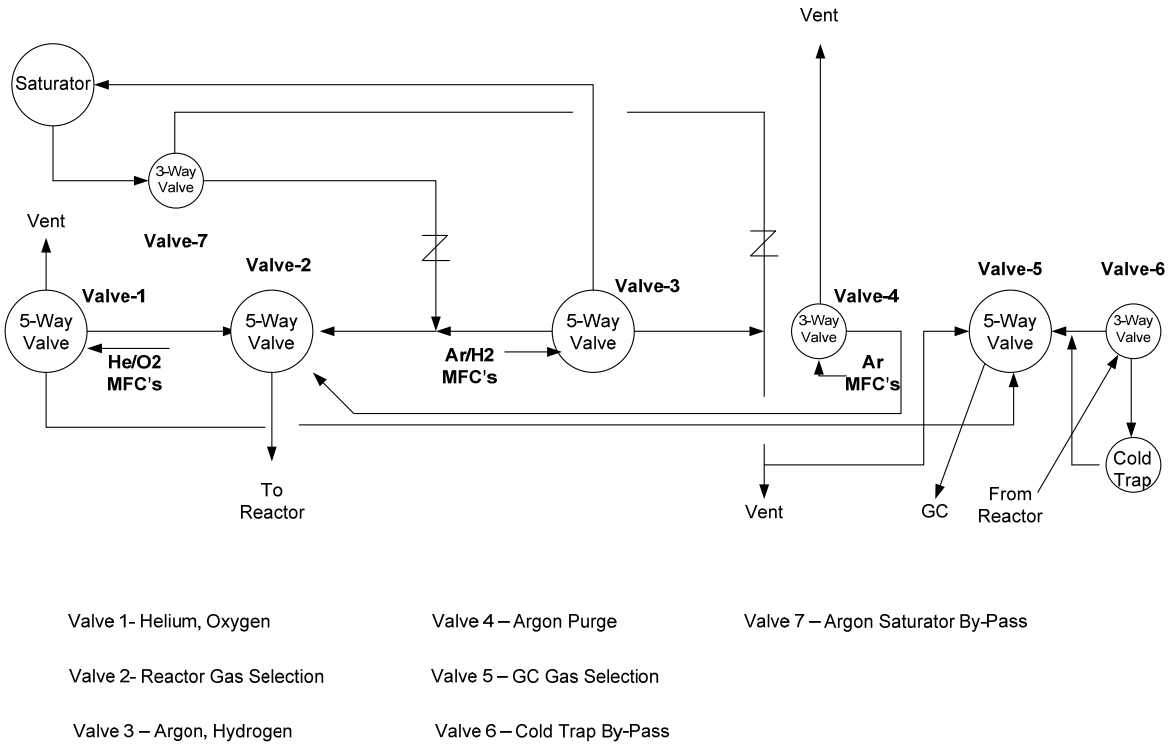

Figure 3. Line drawing of the test apparatus used for ferrite redox material studies.

Our early test results were encouraging but in some cases reproducibility was a problem. For example, our initial tests using the nickel manganese iron oxide reactant material, hydrogen production varied from 32 to 49 cc for a 1.6 gram sample (20-30.6 cc/gm). However, hydrogen production dropped to zero after one cycle l. Summary results from our initial testing are given in table 1. Mainly because results were consistent, we decided to focus our testing on a baseline cobalt ferrite to understand the design variables. Processing parameters such as synthesis procedure and particle size as well as the impact of supporting the ferrite in a zirconia matrix were studied. Hydrogen and oxygen yields over successive cycles were the primary metric. Figure 4 shows hydrogen production yields of a cobalt ferrite sample for 31 redox cycles. An encouraging result was that performance improved with increased cycling. We also applied characterization techniques such as X-ray diffraction, microscopy, and temperature programmed reduction and oxidation to provide insights into the chemical and physical processes occurring in the ferrites during operation. Figure 5 shows photographs of (a) prototype reactant fin segments, and Robocast test parts (b) as cast, and (c) after 31 redox cycles. This is the test part subjected to the 31 thermal cycles in figure 4. During testing it lost porosity and shrank by 18%. Additional results from our ferrite material studies are given in Appendix D.

Table 1. Results of initial screening test for water splitting (Powders).

Sample	Reduction/Oxidation Temperatures (°C)	Maximum H_2 Yield w/o ZrO_2 (cm^3/g ferrite)	Maximum H_2 Yield w/ ZrO_2 (cm^3/g ferrite)
$Mn_{O.36}Fe_{2.64}O_4$	1100/800	0.03	N/A
$Ni_{0.5}Mn_{0.5}Fe_2O_4$	1100/800	0.0	N/A
$Ni_{0.39}Mn_{0.35}Fe_{2.26}O_4$	1100/800	29	28
$Co_{0.67}Fe_{2.33}O_4$	1400/1100	1.7	2.3
$Ni_{0.67}Fe_{2.33}O_4$	1400/1100	0.11	2.7

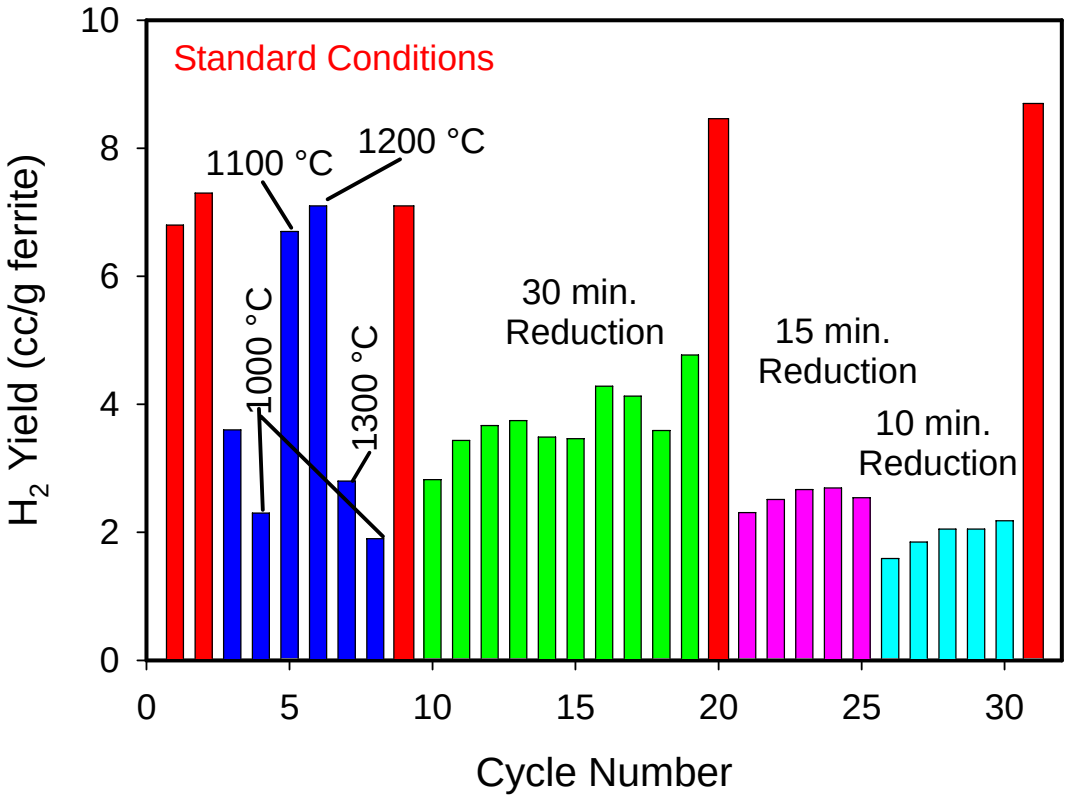

Figure 4. Summary results for a Robocast cobalt ferrite sample for 31 redox cycles. The colors correspond to various test conditions. Note that performance improved with the number of cycles.

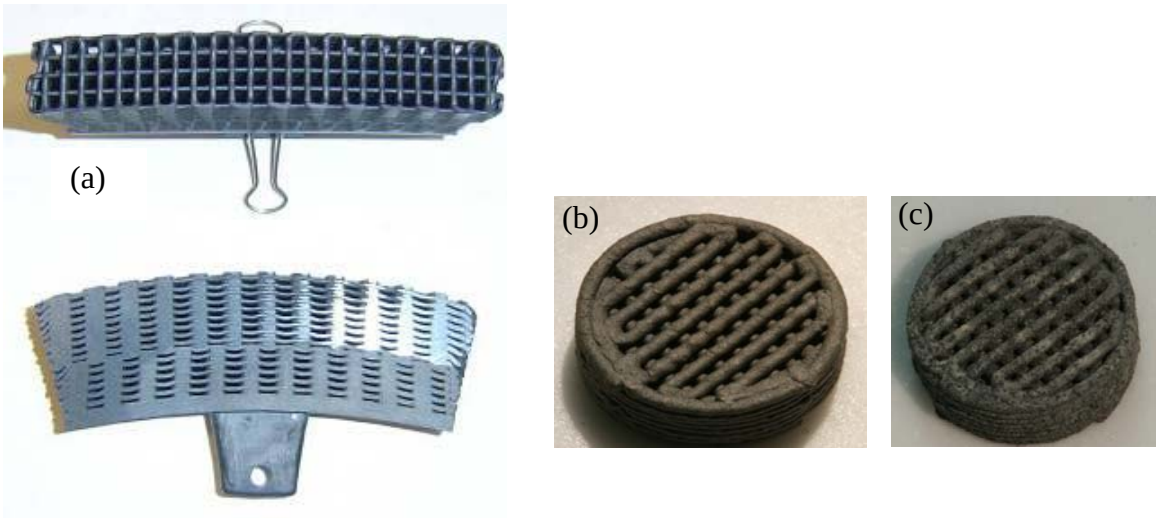

Figure 5. Photograph of Robocast (a) prototype reactant fin segments, (b) as-cast cobalt ferrite/zirconia test sample and (c) the cobalt ferrite/zirconia test sample after 31 thermal reduction and water oxidation cycles. The as-cast test sample is approximately 15-mm diameter and 5.4-mm thick.

A key result of our materials studies is an appreciation of the importance of the zirconia support in enhancing the reduction reaction and avoiding issues associated with melting. Studies with iron oxide suspended in stabilized zirconia indicate a small amount of the iron oxide would be expected to go into solid solution with the zirconia support. It is possible that any remaining liquid iron oxide phase might "wet" or be suspended within the zirconia. In addition, the high oxygen mobility through zirconia may enhance kinetics. An important consequence is that high porosity may not be needed and sintering of the porous zirconia may not be an issue. These observations appear to be in good agreement with those obtained by Ishihara et al., [16] and may be a key to the CR5 concept viability. They suggest a new type of redox material with high internal oxygen mobility for transport of oxygen to and from dispersed redox sites.

In preparation for CR5 prototype testing, we upgraded National Solar Thermal Test Facility (NSTTF) solar furnace at SNL in Albuquerque, NM and performed small-scale solar experiments. In addition to gaining on-sun operational experience, these experiments allowed us to extend the thermal reduction temperature well beyond the 1425^{o}C operational limit of our electric furnace test facility. As with our lab-scale experiments small-scale solar testing involves alternately thermally reducing and re-oxidizing with steam small ferrite samples. Figure 6 is a photograph of the NSTTF solar furnace facility. In these tests a nominal 3 gram Robocast ferrite sample is heated on sun as an argon carrier gas flows through it at a rate of 60 standard cm^3 per minute. The Robocast sample (similar to those previously tested) is supported at the end of a 16 mm (5/8 inch) outside diameter (O.D.) mullite tube. The mullite tube is enclosed in a 35 mm. (1-3/8-inch) O.D. closed-ended fused-silica tube. A schematic of the experimental setup is shown in figure 7. Oxygen from the reduced cobalt ferrite ($Fe_{2.33}Co_{0.67}O_4$) is sampled through a

capillary tube with a Dycor residual gas analyzer (RGA). During the TR step, the sample temperature of approximately 1580^{o}C is maintained by attenuating the solar power delivered to the sample. After 10 minutes the temperature is reduced to approximately 1050^{o}C by partially closing the solar-furnace attenuator. Steam is then introduced into the argon carrier gas. Sample temperatures are measured with a platinum/rhodium (Type S) thermocouple embedded in the sample and a Mikron MI-GA5 IP65 400-2500^{o}C pyrometer. Because the pyrometer senses in the 1.45-1.8 μm range, its signal is contaminated with reflected solar flux. Assuming a sample emissivity of 0.85, correlation of the two measurements indicates that the pyrometer over predicts sample temperature by about 20^{o}C at the TR temperature and by about 120^{o}C at the WO temperature.

Figure 8 shows test results with a 20 wt. % cobalt ferrite in yttria stabilized zirconia (YSZ) Robocast part. Quantification of the amount of product hydrogen with the Dycor RGA ranged from 3.5 to 4 standard cm^{3} per gram of ferrite for the three cycles shown in figure 8. The hydrogen/oxygen ratio ranged from 1.98 to 2.57. These results are consistent with our previous electric furnace testing on Robocast parts. The most important result from the solar testing is that the Robocast ferrite structures are robust and maintain integrity though repeated cycles at elevated temperatures. Results have also been largely independent of how the ferrite is formulated. This is an important consideration as we scale-up ferrite production for the CR5 and modify the synthesis technique to minimize hazardous waste. Although, we continue to investigate alternative reactant materials, we selected Robocast cobalt ferrite as our baseline material for CR5 prototype testing.

Figure 6. Photograph of the NSTTF solar furnace facility. A large Venetian-blind like attenuator located between the flat heliostat and parabolic dish concentrator allows the solar power to the experiment to be varied.

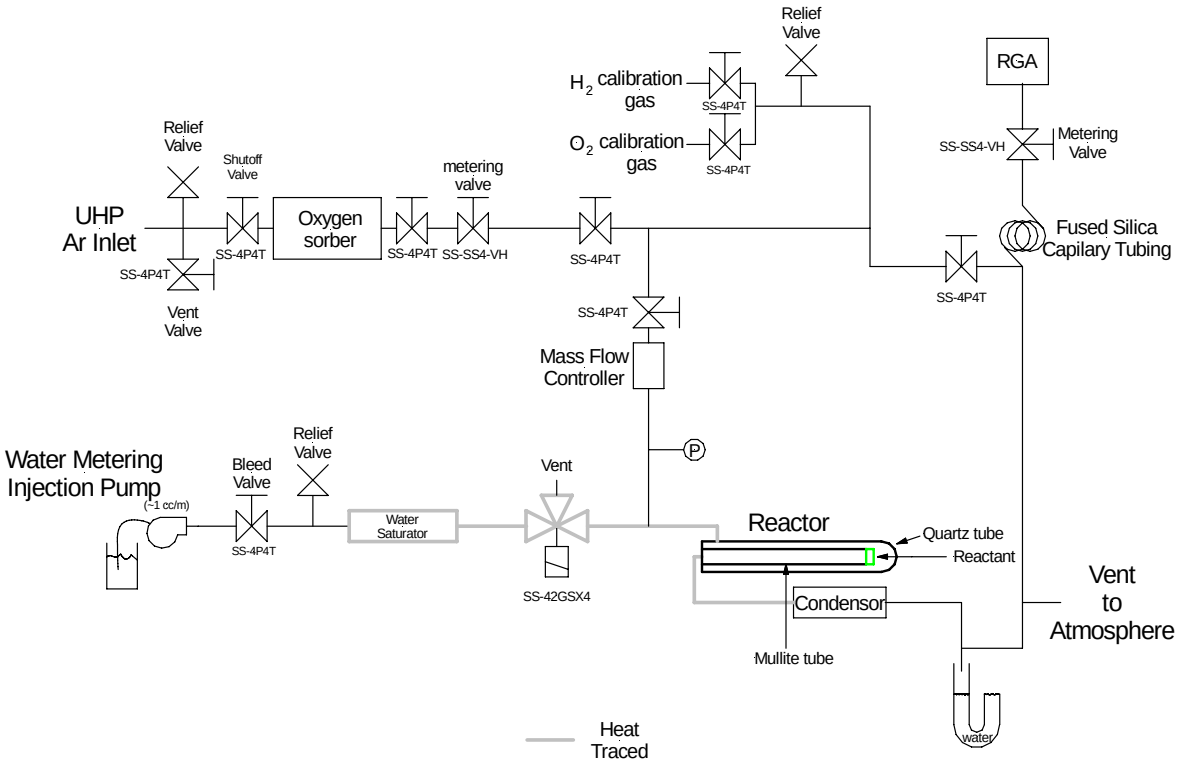

Figure 7. Schematic of the solar furnace small-scale solar testing apparatus.

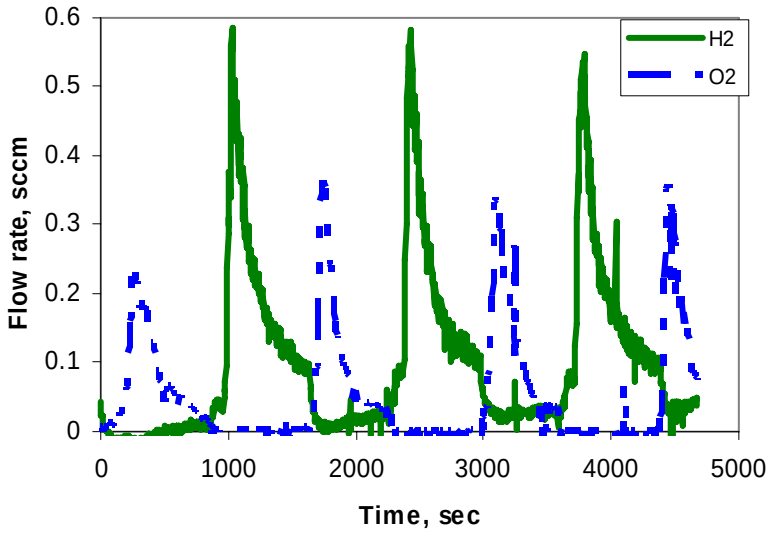

Figure 8. Hydrogen and oxygen production as measured by a residual gas analyzer in a solar furnace experiment. The integrated hydrogen production was approximately 3.5 to 4.0 scc/gram ferrite/cycle in these experiments. The TR and WO reactor temperatures were approximately 1580 ^{o}C and 1050 ^{o}C, respectively, during the 10 minute stages.

Numerical simulations were used to address key thermal and fluid dynamic aspects of the CR5. Because detailed radiation modeling in this device is extremely computer intensive and the kinetics are not known, we did not developing a comprehensive model incorporating radiation, chemical reactions,

advection, multi-species flow, etc. Instead, our approach was to model key aspects of the design, specifically recuperator performance and the potential for buoyancy driven flow between reactors through the recuperators. Benchmark comparisons of the simple recuperator sub-model in the thermodynamic cycle model described in Appendix B with a detailed recuperator model that accounts for solid-state heat conduction; uses temperature-dependent properties for candidate materials of construction; and detailed enclosure radiation are in good agreement. Because neither model accounts for conduction/convection heat transfer through the gas between fins or additional recuperation within the reactor sections, both of which can enhance recuperation, we have concluded that the counter rotating-ring-recuperator concept is viable. To evaluate the potential for cross flow through the recuperator, separate flow models that use the results from the thermal model to define the temperature field were developed. We used the FLUENT computational fluid dynamics (CFD) code to simulate the flow field within the device. [22] The simulation was used primarily to assess the potential for cross flow through the recuperators. Because the two reactors are connected through the recuperators, there is a possibility for hydrogen or oxygen generated in the WO and TR reactors, respectively, to cross over to the opposite reactor. Results from the simulations indicate that ring rotation has no effect on crossover and the potential for buoyancy-driven crossover is minor. Figure 9 shows FLUENT simulation results for hydrogen and oxygen concentrations for the case in which the pressure difference between reactors is zero. For this case cross over is less than 1%. With a pressure difference of 5 Pascal cross over is about 20%.

Experimental investigations of ferrite thermochemical cycles, including ours, have generally involved cyclic operation of small samples in which an inert gas “sweeps” the reactant material. In these experiments small samples of ferrite reactant (on the order of grams) are alternately thermally reduced and re-oxidized with steam. An inert sweep gas such as argon, helium, or nitrogen facilitates transport of the product hydrogen and oxygen through the experimental apparatus. While results from these tests are promising, the use of an inert sweep gas artificially reduces the partial pressures of the product gases. Although, in principal, it is possible to evaluate reactivity under more realistic oxygen or hydrogen partial pressures by sweeping with oxygen or hydrogen, this would add significant uncertainty to the measurement of the amount of product gases. In addition, as the reactant is cycled between reaction steps, the presence of hydrogen and oxygen would re-oxidize or re-reduce the reactant material as the temperature changes. Quenching the reactions by introducing an inert gas also changes the operational conditions and introduces uncertainty.

Because the CR5 provides for simultaneous operation of the TR and WO reactors with large quantities of reactant material (on the order of kilograms), it provides operational environments that are more characteristic of what is needed in real devices. With potentially large amounts of product gases, the need for sweeping for transport purposes is diminished. It also facilitates continuous and controlled

sweeping of the product gases with steam and/or inert gas, if desired. Therefore, given the numerous uncertainties, we believe a proof-of-concept prototype CR5 thermochemical heat engine is needed to establish feasibility and to evaluate many of the unknowns. For these reasons, a proof-of-concept device with the overall objective of demonstrating the key features of the CR5 at a reasonable scale was designed and built. Unfortunately, it has not been tested yet. We anticipate a successful demonstration might produce as much as 100 standard liters per hour of hydrogen from water and be capable of absorbing up to 9 kW of concentrated solar from the SNL NSTTF solar furnace. The design is a first attempt to address high-temperature moving parts and other design issues. Ancillary hardware such as steam generation equipment and pumps and their integration into the system will not be addressed initially. The prototype CR5 design and performance predications are presented in Appendices F and G, respectively.

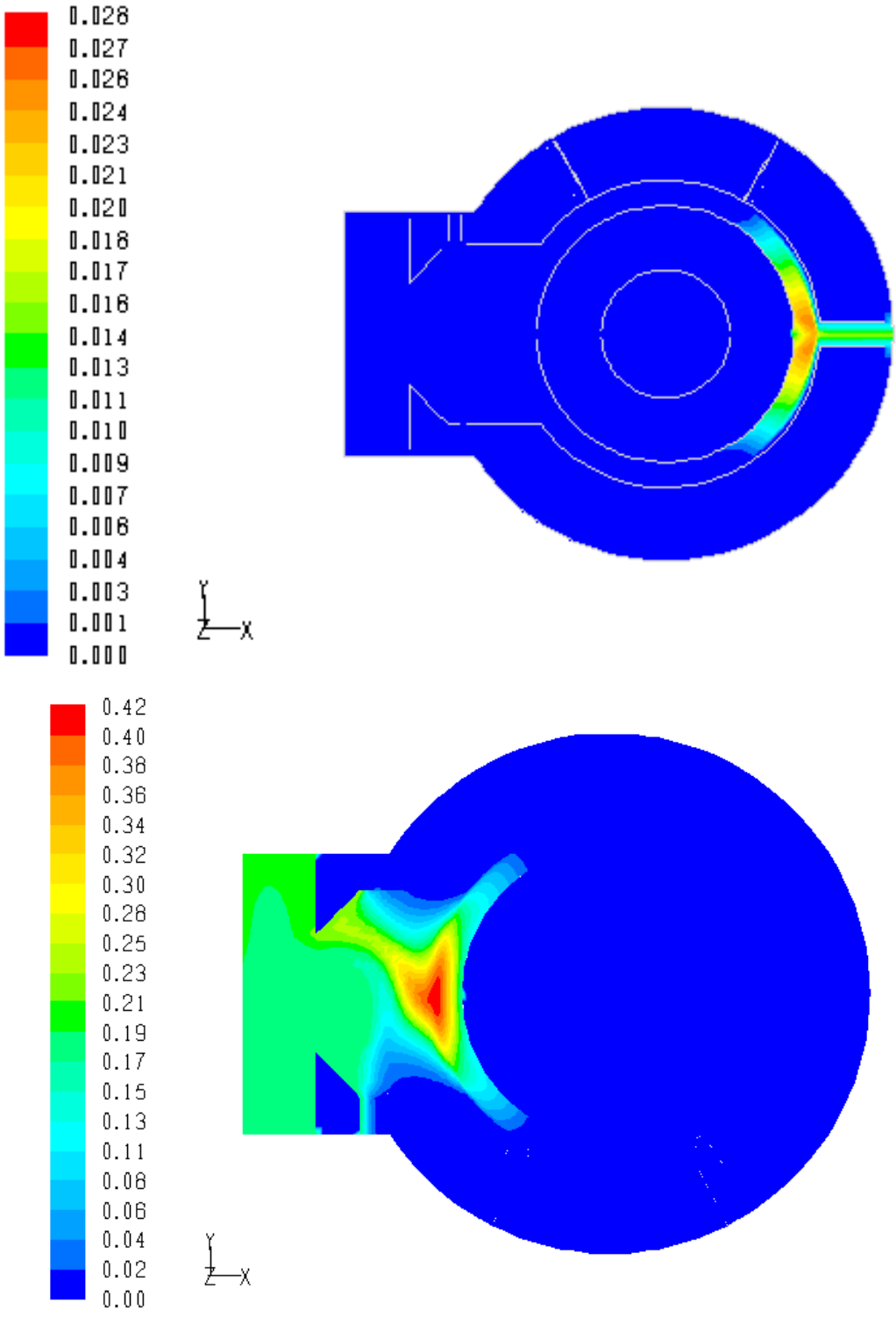

Figure 9. FLUENT simulation result of the CR5 prototype showing hydrogen (top) and oxygen (bottom) concentration fractions assuming a zero pressure differential between reactors.

CONCLUSIONS

Solar hydrogen production from water by the use of solar driven two-step thermochemical cycles is potentially an alternative to fossil fuels. Recognizing that thermochemical cycles are heat engines that convert thermal energy into chemical energy and are, therefore, analogous to mechanical work producing machines, we have conceived a new kind of heat engine. As in Stirling and Ericsson cycle mechanical work producing counterparts, counter-current recuperation of sensible heat within the cycle is key to high efficiency in the CR5. Investigations of the efficiency potential of the CR5 concept suggest solid-to-solid counter-current recuperation can be effective and that the cycle can potentially be efficient. Furthermore, recuperation mitigates the need for complete reaction extent and permits the use of a support for the ferrite working material. These investigations also suggest that the underlying thermodynamic properties of the iron oxide redox materials are marginal at the temperatures dictated by materials and that a number of schemes will probably be required to compensate. These include adjusting the redox thermodynamics by substituting other metals for iron in the spinel; taking advantage of solid-gas reactions by continuous removal of the product gases; and effectivily lowering the product gas partial pressure by counter-current sweeping. Like other engines, the CR5 involves numerous design issues and tradeoffs. It places extraordinary demands on materials and involves high-temperature moving parts. In addition, the CR5 must be designed and operated to avoid crossover through the recuperator. In the process of evaluating materials for the CR5 heat engine, we have developed a new kind of reactant material in which ferrite particles are dispersed in a monolithic zirconia structure. These materials appear to enhance and maintain reactivity and kinetics, as well as provide the structural support needed in the CR5 heat engine.

To establish the practicality of the CR5 concept, we experimentally evaluated materials, explored the thermodynamic of ferrite spinel/zirconia mixtures, evaluated temperature and fluid flow within a device, and designed and built a CR5 prototype. Depending on its test results and if suitable materials can be developed and the design challenges can be met, the CR5 heat engine concept appears to provide an integrated approach for potentially efficient and low-cost solar hydrogen.

REFERENCES

1. Dunn, S., 2001, “Hydrogen Futures: Toward a Sustainable Energy System,” Worldwatch Paper 157, Worldwatch Institute, Washington, D.C.
2. O’Gallagher, J.J., Lewandowski, A., 2005, “Achieving Ulta-High Solar Concentration for the Production of Hydrogen in a Central Receiver Plant Using A Nonimaging CPC type Secondary,” Proceedings of the ASES 2005 Solar World Congress, Orlando, FL.
3. Diver, R.B., Andraka, C.E., Rawlinson, K.S., Goldberg, V., Thomas, G., 2001, “The Advanced Dish Development System Project,” ASME Proceedings of Solar Forum 2001, Washington, D.C.
4. National Academies of Science Report to DOE, 2002, “Critique of the Sargent and Lundy Assessment of Cost and Performance Forecasts for Concentrating Solar Power Technology”, Washington, D.C.
5. Fletcher, E.A., Moen, R.L., 1977, “Hydrogen and Oxygen from Water,” *Science*, Vol. 197, pp. 1050-1056.
6. Brown L., Besenbruch, G.E., Chen, Y., Diver, R., Earl, B., Hsieh, S., Kwan, K., McQuillan, B.W., Perkins, C., Pohl, P., Weime, A., 2005, "A Database of Solar Thermochemical Hydrogen Cycles," Proceedings of the National Hydrogen Association, Washington, D.C.
7. Brown, L.C., Funk, J.F., Showalter, S.K., 2000, “High Efficiency Generation of Hydrogen Fuels Using Nuclear Power,” GA-A23451, San Diego, CA.
8. Nakamura, T., 1977, “Hydrogen Production from Water Utilizing Solar Heat at High Temperatures,” *Solar Energy*, Vol. 19 pp. 467-475.
9. Lundberg, M., 1993, “Model Calculations on Some Feasible Two-Step Water Splitting Processes,” *Int. J. Hydrogen Energy*, Vol. 18, No. 5 pp. 369-376.
10. Tamura, Y., Steinfeld, A., Kuhn, P., and K. Ehrensberger, 1995, “Production of Solar Hydrogen by a Novel, 2-Step, Water-Splitting Thermochemical Cycle,” *Energy*, Vol. 20, No. 4, pp. 325-330.
11. Steinfeld, A., Kuhn, P., Reller, A., Palumbo,R., Murry, J., Tamaura, Y., 1998, “Solar –Processed Metals a Clean Energy Carriers and Water-Splitters,” *Int. J. Hydrogen Energy*, Vol. 23, No. 9, pp. 767-774.
12. Ehrensberger, K., Frei, A., Kuhn, P., Oswald, H.R., and P. Hug, 1995, “Comparataive Experimental Investigations of the Water-Splitting Reaction with Iron Oxide Fe1-yO and Iron Manganese Oxides (Fe1-xMnx)1-yO,” *Solid State Ionics* 78 pp. 151-160.
13. Aoki, H., Kaneko, H., Hasegawa, Ishihara, H., Takahashi, Y., Suzuki, A, and Y. Tamaura, “Two-Step Water Splitting with Ni-Ferrite System for Solar H2 Production Using Concentrated Solar Radiation,” Proceedings of ISES 2004 in Solar 2004, ASME: International Solar Energy Conference, Portland, OR, 2004.
14. Kodama, T., et al., 2003, “Hydrogen Production by Solar Thermochemical Water-Splitting/Methane-Reforming Process, Proceedings of the ASME ISES Conference, Hawaii.
15. Kodama, T., Kondoh, Y., Yamamoto, R., Andou, H., Satou, N., 2005, “Thermochemical hydrogen production by redox system of ZrO2-supported Co(II)-ferrite,” *Solar Energy* 78, pp. 623-631.
16. Ishihara, H., Kaneko, H., Yokoyama, T., Fuse, A., Tamaura, Y., 2005, “Hydrogen Production Through Two-Step Water Splitting Using YSZ (Ni, Fe) System for Solar Hydrogen Production,” Proceedings of ISEC 2005 International Solar Energy Conference, Orlando, FL.

17. Kaneko, H., Miura, T., Fuse, A., Ishihara, H., Taku, S., Fukuzumi, H., Naganuma, Y., Tamaura, Y., 2007, “Rotary-Type Solar Reactor for Solar Hydrogen Productin with Two-step Water Splitting Process,” *Energy & Fuels*, 2007, 21, 2287-2293.
18. Roeb, M., Sattler, C., Kluser, R., Monnerie, L., Konstandopoulos, A.G., Agrafiotis, C., Zaspalis, V.T., Nalbandian, L., Steele, A., Stobbe, 2005, “Solar Hydrogen Production by a Two-Step Cycle Based on Mixed Iron Oxides,” ASME Proceedings ISEC 2005 International Solar Energy Conference, Orlando, FL.
19. Steinfeld, A., Sanders, S., and R. Palumbo, “Design Aspects of Solar Thermochemical Engineering –A Case Study: Two-Step Water-Splitting Cycle Using the Fe3O4/FeO Redox System,“ *Solar Energy* Vol. 65, No. 1, pp43-53, 1999.
20. Bale, C. W., Chartrand, P., Degterov, S. A., Eriksson, G., Hack, K., Mahfoud, R. B., Melançon, J., Pelton, A. D., and Petersen, S., 2002, "FactSage Thermochemical Software and Databases," *Calphad* 26, 189.
21. Cesarano III, J., Segalman, R., Calvert, P., 1998, “Robocasting Provides Moldless Fabrication from Slurry Deposition,” *Ceramic Industry*, 148: p. 94-102.
22. FLUENT Version 6.2, FLUENT Inc., 2005

APPENDIX A

CR5 CYCLE THERMODYNAMICS

Appendix A - CR5 Cycle Thermodynamics

The basic premise of thermochemical water splitting cycles is that the desired water splitting reaction (H_2O $H_2 + ½ O_2$) can be accomplished with a thermal energy input under more reasonable conditions than direct thermolysis by replacing the single reaction that has unfavorable thermodynamics at most conditions with two or more reactions that sum to water splitting and that each have favorable thermodynamics. In other words for each step in the thermochemical cycle the Gibbs free energy change (G) of the reaction should be negative in a temperature range far below that of water thermolysis. Restating this for the hypothetical two-step metal oxide cycle shown, G_1 and G_2 should be < 0 at $298K < T << T_{WS}$, where T_{WS} is the temperature of water thermolysis (> 2500K for a significant degree of dissociation)

MOx $MO(x-1) + ½ O_2$ $G_1 = H_1 - T S_1$ (A-1)

$MO(x-1) + H_2O$ $MOx + H_2$ $G_2 = H_2 - T S_2$ (A-2)

H_2O $H_2 + ½ O_2$ $G_{WS} = H_{WS} - T S_{WS}$ (A-3)

As shown, if the reactions sum to the water splitting reaction, at any given temperature the Gibbs free energy change (G) of the reactions must also sum to G of water splitting at that temperature. (The G of the reactions can be increased to some extent by operating at reduced pressures or sweeping.) This fact combined with the temperature requirement and the fact that G_{WS} is always positive at temperatures of interest and has a negative slope with temperature (see figure A-1), has several implications. First, at any temperature where G_1 is negative, G_2 must be a positive number equal to $G_{WS} - G_1$. Conversely, at any temperature where G_2 is negative, G_1 must be a positive number equal to $G_{WS} - G_2$. In other words, G_1 and G_2 must have opposite slopes (one positive, one negative) as a function of temperature (refer to curves A and B in figure A-1), or one reaction must have a positive entropy change and the other negative (for this discussion we make the reasonable assumption that H and S of each reaction are relatively constant over the temperature range). From a more practical standpoint, this translates into a general requirement for the two steps to be carried out at different temperatures.

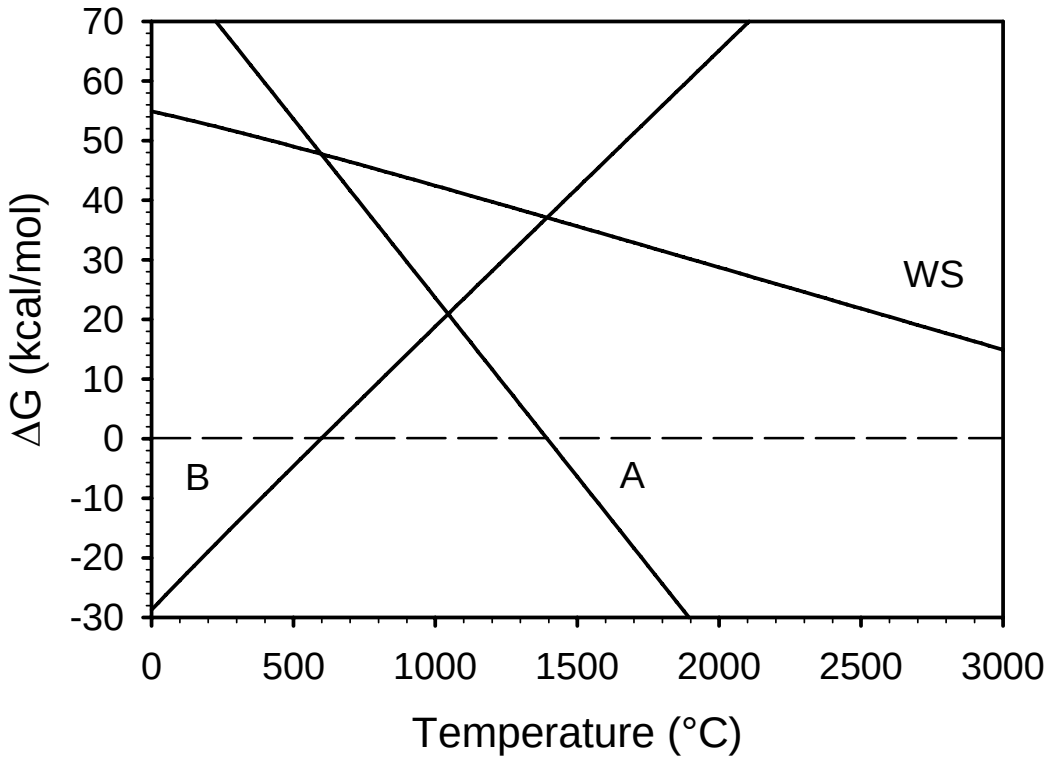

Figure A-1. Plot of the thermodynamics of the water splitting reaction (WS, $H_2O \rightarrow H_2 + ½ O_2$) and a hypothetical two step thermochemical cycle (A and B) illustrating the relationship between the three.

Going further, to meet all the constraints, G for the higher temperature reaction must have a negative slope (a positive S) and must at some point cross the G_{WS} curve(as shown for curve A). To achieve this, the high temperature reaction must be more endothermic than WS ($H_A >$ H_{WS}) and must have a slope that is more negative than that of WS ($S_A >$ S_{WS}). The low temperature step will be mildly exothermic ($H_B =$ $H_{WS} -$ H_A) and have a shallower slope ($S_B =$ $S_{WS} -$ S_A). It is generally true that metal oxide reduction is endothermic, and thus the high temperature step (curve A) corresponds to TR, and the low temperature step (curve B) to WO. Ideally S of TR will be large as this has the effect of bringing the favorable temperature ranges for the two reactions (TR and WO, curves A and B) closer together and drives the G more negative with smaller temperature changes.

To understand the requirements for efficient two-step ferrite thermochemical cycles, it is instructive to consider simple thermodynamic models for the iron oxide system like that described by Nakamura. [A-1] Figure A-2 is a simple model of the iron oxide system and illustrates some fundamental considerations. In it, iron oxide is cycled between 600 K where it is reacted with steam in a WO reactor to produce hydrogen at one atmosphere and magnetite (Fe_3O_4), and 2300 K where the magnetite is thermally reduced

in a TR reactor to produce oxygen, also at one atmosphere, and wustite (FeO) as in equations 1 and 2. For the purpose of illustration, we assume that 100% of the magnetite is converted to wustite and the water/wustite has a reaction extent of 100%. (In reality, this is an unrealistically optimistic assumption at these temperatures and pressure.) Utilizing the thermodynamic data in HSC Chemistry ® for Windows (HSC) [A-2] we calculate that the amount of energy needed to heat the one mole of magnetite exiting the WO reactor from 600 K to 2300 K is 118.78 kcal; the amount of energy needed to drive the TR reaction to produce 3 moles of wustite and ½ mole of oxygen is 57.86 kcal; the amount of energy that needs to be rejected from the 3 moles of wustite to cool back to 600 K is 94.36 kcal; and the amount of exothermic heat that needs to be rejected from the hydrolysis reactor where one mole of hydrogen is produced and one mole of magnetite is regenerated is 16.46 kcal. In addition, 2.08 kcal of sensible heat in the product hydrogen and 8.44 kcal in the product oxygen need to be rejected. To heat and boil one mole of water from ambient (298.15 K) to produce water vapor at 373.15 K requires 11.12 kcal and to heat it to 600 K requires another 1.90 kcal. The higher and lower heating values of the product hydrogen and oxygen are 68.31 and 57.80 kcal, respectively. For comparison to heat engines, it is appropriate to base output on the change in Gibbs free energy, G, of reaction, 56.68 (liquid) or 54.63 kcal (gas). [A-3]

Without recuperation of the rejected heat, the amount of energy that must be supplied is 57.86 + 118.78 + 1.90 + 11.12 = 189.66 kcal. If we define efficiency as the energy content in the product hydrogen and oxygen, the higher heating value (HHV) efficiency is at most 68.31/189.66 = 36.0 %. If the round-trip reaction extent of magnetite to wustite and back is a more realistic 35%, then the amount of thermal energy needed to heat the magnetite from 600 K to 2300 K is 118.78/0.35 = 339.37 kcal and the resulting HHV efficiency is only 16.7%. If the iron oxide is supported on a substrate such as zirconia, even more energy is required for sensible heating and the efficiency is even lower.

With recuperation the amount of heat required can be substantially reduced. However, because of a pinch point that results from the different melting points of Fe_3O_4 (1870K) and FeO (1650 K) the net heat required is not simply 57.86 + 118.78 - 94.36 – 8.44 = 73.84 kcal. Instead, to ensure a positive temperature gradient throughout the recuperator, 89.88 kcal of solar energy must be added resulting in a HHV efficiency of 76.0 %. Without recuperating the high-temperature sensible heat in the product oxygen, a maximum HHV efficiency of 74.4 % is possible. (See the pinch point diagram in figure A-3.) As Nakamura pointed out in Ref. 8, there is sufficient energy from the hydrolysis reaction to vaporize the water and preheat it to 600 K.

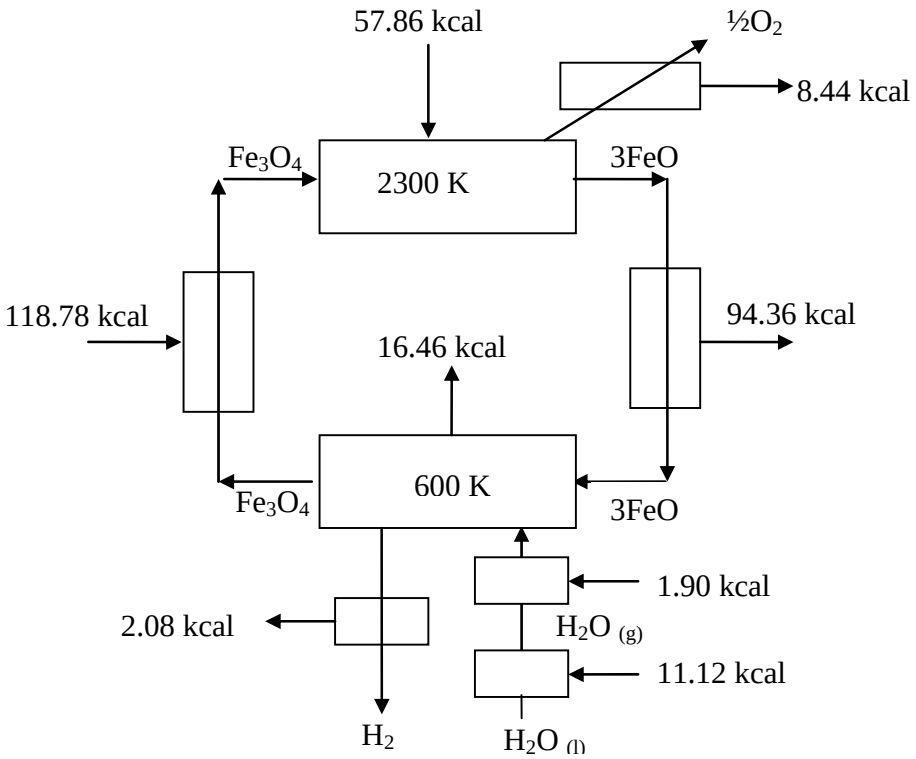

Figure A-2. Schematic showing heat flows of an ideal Iron Oxide cycle operating between 600 and 2300 K.

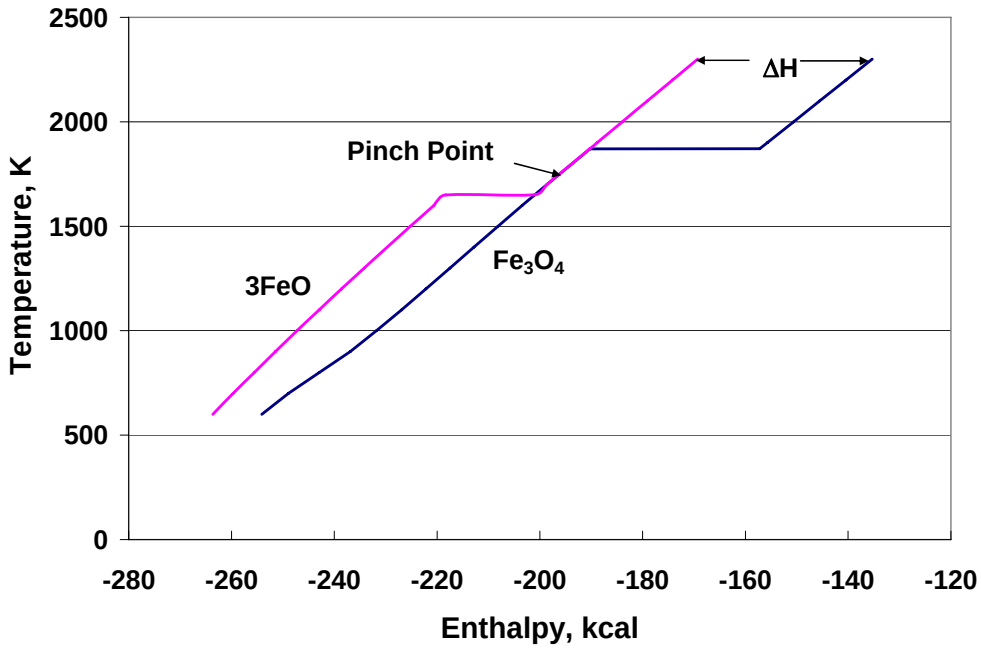

Figure A-3. Pinch-point diagram for an ideal Iron Oxide cycle operating between 600 and 2300K. The amount of sensible energy that must be added to the high-temperature step, H, must be high enough to ensure a positive temperature gradient in all parts of the counter-current heat exchanger. In addition, the heat of reaction, 57.86 kcal, must also be added to the high-temperature step to convert magnetite into wustite.

It is important to note that with efficient recuperation between the WO and TR reactors, the cycle can be efficient even with less than complete reaction and with an inert support. In fact, assuming ideal recuperation the ideal efficiencies above are theoretically possible with any level of conversion and mass of support. In reality, recuperation is never ideal and achieving high conversion extent and minimizing the amount of inert support are important.

References

A-1 Nakamura, T., 1977, "Hydrogen Production from Water Utilizing Solar Heat at High Temperatures," *Solar Energy*, Vol. 19 pp. 467-475.

A-2 Computer program, "Outokumpu HSC Chemistry for Windows", 2002, Version 5.1 (HSC 5), Antti Roine, 02103-ORC-T, Pori, Finland.

A-3 Fletcher, E.A., Moen, R.L., 1977, "Hydrogen and Oxygen from Water," Science, Vol. 197, pp. 1050-1056.

APPENDIX B

SYSTEM ANALYSIS

Appendix B - System Analysis

A simple system performance model was developed to understand the efficiency potential and requirements of the CR5 thermochemical heat engine. The system model includes a thermodynamic cycle and a solar collection model. For the thermodynamic cycle model we developed conceptual CR5 engine designs to estimate the potential for recuperation and understand other key design parameters. The designs assume 36 kW of net solar-thermal energy delivered to the TR section of the reactor. The 36 kW is a nominal value for the 10 kW_e Advanced Dish Development Systems (ADDS). [B-1] The ADDS are dish/Stirling systems with high performance parabolic dish concentrators suitable for the CR5.

Sample design parameters for a CR5 engine using iron oxide as a reactant material are listed in Table B-1. In the design, the fin outside diameter is 0.61 m (24 inch). Recuperation heat rate, Q_r, was modeled assuming radiation heat transfer according to equation B-1 as in the analysis of radiation heat transfer between parallel plates.

$$Q_r = \sigma A F_{1-2} (T_1^4 - T_2^4) / ((2/\varepsilon) - 1) \qquad \text{(B-1)}$$

Based on the close proximity between fins, a fin-to-fin view factor, F_{1-2}, of 1.0 was assumed. A fin emissivity, , of 0.9 was also assumed. is the Stefan-Boltzmann constant. The recuperator radiation heat transfer area, A, was determined from the geometry of the 68 (34 pairs) of 25.4-mm (1-inch) tall fins. For these calculations the TR and WO reactor sections and the two recuperator sections each used one-quarter of the ring circumference. The ring spacing is 6.4 mm center-to-center (¼ inch). This is the smallest spacing we believe to be reasonable in a practical device. In the analysis, the recuperators are divided into 20 equal temperature-difference sections and the average temperatures of each section are iteratively calculated by finding the temperature difference (T_1-T_2) between counter-rotating fins such that the recuperation heat rate in equation B-1 for the 20 sections in the two recuperators equals the recuperator burden, Q_b, in equation B-2.

$$Q_b = \dot{m} c_p (T_{approach} - T_{WO}) \qquad \text{(B-2)}$$

In equation B-2, $\dot{m}$ is the mass flow rate of the reactant fins, c_p is the fin average heat capacity, $T_{approach}$ is the temperature of the fins as they enter the TR reactor, and T_{WO} is the WO reactor temperature.

The use of an average fin heat capacity simplifies the analysis and means that $T_1 - T_2$ is constant across the recuperator and is equal to $T_{TR} - T_{appraoch}$. T_{TR} is the TR reactor temperature. Ring speeds of 0.5 to 1 revolutions per minute (RPM) and reactant fin thicknesses on the order of 0.5 to 1 mm and containing 75% weight percent zirconia (ZrO_2) are typical. With an estimated reactant fin density of 3500 kg/m^3 the void fraction of the fin stack is nearly 90%. Increasing the amount of reactant fin

material (reducing the fin void fraction) and proportionally reducing the ring speed results in the same performance and is potentially a way to increase residence time in the WO and TR reactors to accommodate kinetics.

Table B-1. Baseline Iron Oxide CR5 heat engine design parameters.

Design Parameter	Value	Description
Q_{solar} (kW)	36	Net solar input into TR reactor.
T_{TR} (K)	2300	Temperature of the TR reactor.
T_{WO} (K)	600	Temperature of the WO reactor.
Pressure (atm)	0.2	Operating pressure.
Fin O.D. (m)	0.61	Outside diameter of the reactant fin.
Fin I.D. (m)	0.56	Inside diameter of the reactant fin.
Fin height (mm)	25.4	Height of reactant fins.
Ring spacing (mm)	6.4	Center-to-center ring spacing.
Fin thickness (mm)	0.775	Thickness of the reactant fins.
Ring Speed (RPM)	0.75	Revolutions per minute of the rings.
Fin inert fraction	0.75	Reactant fin zirconia mass fraction.
Fin ave c_p (J/kgK)	800.8	Reactant fin average heat capacity.
Fin density (kg/m^3)	3500	Reactant fin density.
Reactor width (m)	0.43	Distance across rings.
Number of rings	68	Number of rotating rings.

The thermodynamic cycle evaluations used HSC to evaluate ferrite spinels included in the HSC database to determine equilibrium compositions and state points across the reactors. The compositions in the reaction zones were calculated by iteratively solving for equilibrium composition of the ferrite reactant alternately subjected to thermal reduction and hydrolysis at 1 atmosphere and removal of the product oxygen and hydrogen, respectively. After several iterations compositions did not change between iterations and the extent of reaction, state-point properties, and thermal inputs could then be determined. With this approach and the HSC data, a TR temperature of 2300 K and a WO temperature of 600 K result in a reaction extent of 0.35 for Fe_3O_4. That is, for every mole of Fe_3O_4, 0.35 moles of hydrogen are produced. Comparable reaction extents could be obtained at 2100 K and 1900 K for Fe_2MgO_4 and Fe_2CoO_4, respectively, also at a WO reaction temperature of 600 K. It is important to note that this approach is conservative in that it does not account for the benefits of solid-gas reactions, e.g. the ability to drive the reaction by continuously removing the product gases. In calculating the state points, it is assumed that there are no reactions taking place in the recuperator. All of the thermal reduction occurs in the TR reactor. We also assume recuperation stops inside the reactor sections. (In reality reactions can occur within the recuperator sections and recuperation would continue at a diminishing rate until the counter rotating reactant fins crossover in the center of the two reactors.)

Although equilibrium is calculated at a pressure of 1 atmosphere, it is assumed that the TR and WO reactors operate at 0.2 atmospheres and the oxygen is compressed to 1 atmosphere and the hydrogen is

compressed to 15 atmospheres. We assume an isothermal compression efficiency of 40% at 300 K based on commercially available vacuum pump data.

Thermal efficiency is defined as

$$\eta_{th} = \frac{\dot{n}_{H_2} \times HHV_{H_2}}{Q_{solar} + \dot{W}_p / 0.4} \qquad \text{(B-3)}$$

Where $\dot{n}_{H_2}$ is molar hydrogen production rate, HHV_{H_2} is the higher heating value of hydrogen, Q_{solar} is the net solar power into the reactor (36 kW), and $\dot{W}_p$ is the compressor power. The compressor itself is assumed to be driven by a heat engine with a thermal-to-mechanical conversion efficiency of 40%. Power requirements for driving the counter-rotating rings are assumed to be negligible.

Table B-2 lists the performance parameters for the iron oxide CR5 design outlined in Table 1. The net HHV thermal efficiency is 29.9%. Note that about 146 kW of power is required for sensible heating of the reactant with most of it supplied by recuperation. (For heating the reactant 125.06 kW is supplied by the recuperator and an additional 20.96 kW of solar power is needed to heat it to temperature.) Only about 10% of the power needed for heating and reducing the oxidized ferrite actually drives the reaction (15.04 kW).

Table B-3 are parametric results are for three metal oxide systems (Fe O), (Fe Mg O), and (Fe Co O); at various temperatures; reaction extents; recuperator heat transfer factors; and inert fractions (zirconia weight fraction). For these calculations, recuperation within the two reactors was accounted for by increasing the recuperation time by 50%. These results indicate that HHV efficiencies of over 50% are theoretically feasible if optimistic estimates are assumed. In the table the reaction extent and the equilibrium reaction extent are listed. The equilibrium reaction extent refers to the percentage of hydrogen, per mole of ferrite calculated iteratively with HSC, as described above. The reaction extent is the moles of hydrogen per mole of ferrite in the simulation. The recuperator factor is relative to our baseline design, including within the reactors. Numerous approaches for enhancing heat transfer are possible. The results indicate that reducing the amount of inactive material, either inert or un-reacted ferrite, is key to high efficiency. Enhancing recuperation heat transfer also helps thermal efficiency.

The thermodynamic model also suggests that the product partial pressures need to be higher than about 0.1 atm. Otherwise, pump work becomes excessive. This means that the ferrite TR equilibrium oxygen and the WO hydrogen/steam partial pressures must be greater than 0.1 atm at operating conditions for this approach to be viable.

It is important to note that the potential for reducing the TR temperature or increasing the WO temperature by continuously removing the product gases by pumping or sweeping was not accounted for

in this analysis. In this respect the results of our system efficiency studies are conservative. Because the extents of reaction depend on kinetics, we do not know how to properly account for this effect. Reducing the TR temperature and increasing the WO temperature to values similar to those currently being experimentally investigated (assuming no reduction in conversion) improves thermal efficiency. For example, changing the TR and WO temperatures to 1800 K and 1000 K, respectively, and assuming the same reaction extent, 0.35, for the example in the tables B-1 and B-2, results in a HHV net thermal efficiency of over 44%. (This is intended to illustrate the importance of recuperation on efficiency. Although hydrogen production on a gram of material basis in this example is comparable to what has been demonstrated by Kodama [B-2], whether or not this reaction extent can actually be obtained in a CR5 device at these temperatures needs to be demonstrated.) The reason efficiency improves is that while the driving potential for recuperation decreases with reduced temperature, equation B-1, lower TR temperatures reduce recuperator burden, equation B-2, especially if phase change can be avoided. Increasing the WO temperature increases the driving potential for recuperation and reduces the thermal burden on the recuperator. Figure B-1 shows the calculated recuperator temperature profiles for the example in the tables. As can be seen in figure B-1, recuperation at high temperatures requires less recuperator length than at low temperatures.

Ring speed is an important parameter. At low speeds recuperation efficiency improves. There is more time for transferring heat. However, if the ring speed is too low the reactant flow rate is inadequate for the thermal input. We anticipate that for any given solar input, there exist optimum speeds for power and efficiency, not unlike conventional engines.

Table B-2. Baseline Fe_3O_4 CR5 heat engine performance parameters.

Operational Parameters	Value	Description
Recuperator T (K)	244	Recuperator temperature difference.
Recuperator Effectiveness (%)	85.6	Percent of sensible energy in reactant fins recuperated.
Recuperator Power (kW)	125.06	Recuperator power for sensible heating of reactant fins.
Ave. solar flux (W/cm2)	17.44	Average incident solar flux on TR section.
Q rec. sensible (kW)	20.96	Amount of incident solar power for sensible heat to T_{TR}.
Q rec. reaction (kW)	15.04	Amount of incident solar power for TR reaction.
Fin array porosity (%)	87.8	Apparent porosity of volumetric reactant fin absorber.
$\dot{m}$ (gm/sec)	107.3	Mass flow rate of reactant/zirconia material.
Reaction extent (%)	35	Effective extent of reaction.
$\dot{n}_{H_2}$ (moles H_2/sec)	0.0412	Hydrogen production rate.
Liters H_2/hour	3320	Hydrogen production rate in standard liters per hour.
HHV H_2 (kW)	11.77	Higher heating value rate of the produced hydrogen.
Compressor power $\dot{W}_p$ (kW)	1.32	Pump power needed to compress the H_2 (15 atm) and O_2 (1 atm).
Gross efficiency (%)	32.7	H_2 HHV rate divided by solar input.
Net efficiency $_{th}$ (%)	29.9	H_2 HHV rate divided by solar input plus power needed for pumps.
Q hydrolysis (kW)	3.67	Exothermic power from WO reactor.
Q fin-sensible (kW)	20.96	Rejected fin sensible power.
Q reject (kW)	24.63	Total recuperator rejected power.
Q H_2O (kW)	2.24	Power needed to vaporize and heat water to T_{WO}.
Q O_2 sensible (kW)	1.49	Sensible power in oxygen stream.
Q H_2 sensible (kW)	0.36	Sensible power in hydrogen stream.

Table B-3. Summary results of metal oxide thermodynamic analysis.

Chemical System	Temp, K	Reaction Extent	Equil. Extent	Recup. Factor	Inert Fraction	HHV Efficiency
Fe O	2300	0.36	0.36	1X	0.75	33.8%
Fe O	2300	0.36	0.36	2X	0.75	40.0%
Fe O	2300	0.50	0.36	1X	0.75	40.3%
Fe O	2300	0.19	0.36	1X	0	40.1%
Fe O	2300	0.24	0.36	2X	0	50.9%
Fe Mg O	2100	0.27	0.27	1X	0.75	31.5%
Fe Mg O	2100	0.27	0.27	2X	0.75	37.3%
Fe Mg O	2100	0.42	0.27	1X	0.75	39.7%
Fe Mg O	2100	0.22	0.27	1X	0	46.1%
Fe Mg O	2100	0.26	0.27	2X	0	53.3%
Fe Co O	2100	0.55	0.55	1X	0.75	39.5%
Fe Co O	2100	0.54	0.55	2X	0.75	43.9%
Fe Co O	2100	0.72	0.55	1X	0.75	43.4%
Fe Co O	2100	0.24	0.55	1X	0	43.1%
Fe Co O	2100	0.27	0.55	2X	0	48.4%
Fe Co O	1900	0.27	0.27	1X	0.75	28.6%
Fe Co O	1900	0.27	0.27	2X	0.75	33.5%
Fe Co O	1900	0.40	0.27	1X	0.75	34.7%
Fe Co O	1900	0.14	0.27	1X	0	38.2%
Fe Co O	1900	0.27	0.27	2X	0	47.8%

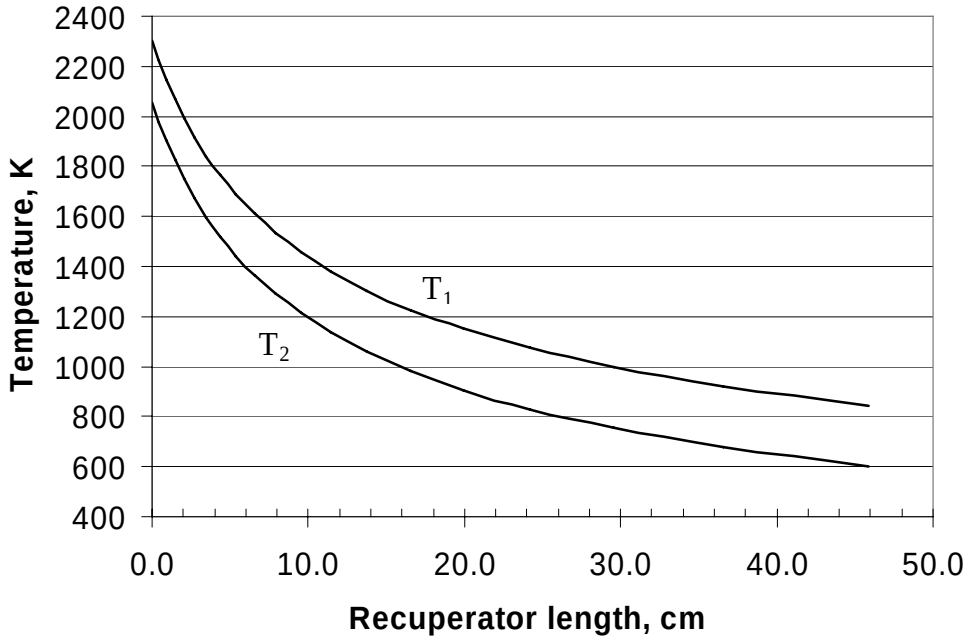

Figure B-1. Recuperator temperature profile for the case presented in tables 1 and 2. Because of the constant heat capacity assumption, each incremental temperature has the same H. Recuperation at high temperatures requires less of the recuperator than at low temperatures.

Analysis of collector efficiencies assuming an average concentration ratio of 4000 with 95% intercept, as demonstrated by the ADDS [B-1], indicate operating temperatures of up to about 2100 K are practical from a solar collection efficiency perspective. Radiation losses from the solar receiver cavity are excessive at temperatures much higher than about 2100 K. (See figure B-2.) From a system efficiency perspective, the mixed-metal ferrites and other approaches for reducing the TR temperature are, therefore, desirable. Furthermore, issues associated with volatilization and melting of the reactant material also encourage lower TR temperatures. Our HSC magnesium and cobalt ferrite results suggest that system efficiency can potentially be substantially better than a high-efficiency dish/Stirling system driving an electrolyzer.

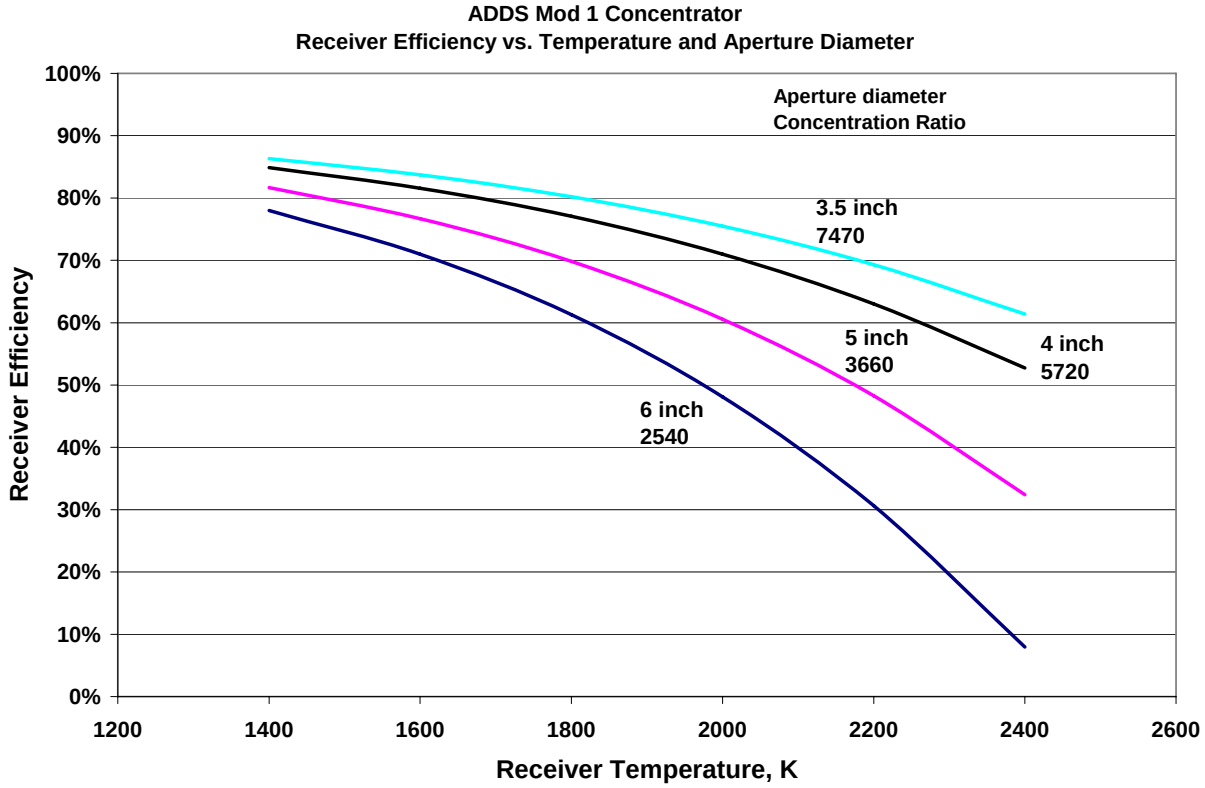

Figure B-2. ADDS Mod 1 concentrator receiver efficacy as a function of receiver temperature and aperture diameter at a direct normal insolation of 1000 W/m^2. The Dish-Stirling system has an aperture diameter of 14 cm (5.5 inches). A "trumpet" secondary concentrator would be needed to reduce aperture diameter to 9 cm (3.5 inches).

References

B-1 Diver, R.B., Andraka, C.E., Rawlinson, K.S., Goldberg, V., Thomas, G., 2001, "The Advanced Dish Development System Project," ASME Proceedings of Solar Forum 2001, Washington, D.C.

B-2 Kodama, T., Kondoh, Y., Yamamoto, R., Andou, H., Satou, N., 2005, "Thermochemical hydrogen production by redox system of ZrO2-supported Co(II)-ferrite," *Solar Energy* 78, pp. 623-631.

Nomenclature

A = recuperator radiation heat transfer area (m^2)

c_p = average reactant fin heat capacity (J/kgK)

CR5 = counter-rotating-ring receiver/reactor/recuperator

$F_{1\text{-}2}$ = view factor between recuperators

HHV_{H_2} = higher heating value of hydrogen (kcal/mole)

HSC = HSC Chemistry ® for Windows

$\dot{m}$ = mass flow rate of reactant (gm/sec)

$\dot{n}_{H_2}$ = hydrogen production rate (moles/sec)

Q_b = recuperator burden (kW)

Q_r = recuperator heat transfer rate (kW)

Q_{solar} = net solar power (kW)

$T_{approach}$ = recuperator temperature at the entrance to the TR reactor (K)

T_{TR} = thermal reduction reactor temperature (K)

T_{WO} = water oxidation reactor temperature (K)

T_1 = heat emitting recuperator temperature (K)

T_2 = heat absorbing recuperator temperature (K)

$\dot{W}_p$ = compressor power.(kW)

= fin emissivity

= Stefan-Boltzmann constant (5.668×10^{-8} $W/m^2/K^4$)

$_{th}$ = thermal efficiency (%)

APPENDIX C

FERRITE THERMODYNAMICS

Appendix C - Ferrite Thermodynamics

Redox cycles using iron-containing ferrites with the spinel structure (AB_2O_4) are being proposed for two-step water-splitting cycles for the production of hydrogen from solar energy [1,2]. These cycles consist of a thermal reduction (TR)step; reaction (C-1) in which solar energy is used to reduce the Fe(III) to the Fe(II) state with release of O_2, followed by a water oxidation step (WO; reaction (2)) in which the reduced oxide reacts with steam to form hydrogen and regenerate the ferrite:

$$A_xFe_{3-x}O_4 \xleftrightarrow{\Delta} xAO + (3-x)FeO + 0.5\ O_2 \qquad \text{(C-1)}$$

$$xAO + (3-x)FeO + H_2O \xleftrightarrow{\Delta} A_xFe_{3-x}O_4 + H_2 \qquad \text{(C-2)}$$

As will be discussed below, these equations represent only the stoichiometric redox reactions. In actuality, solid solutions form that contain various metal oxides. In the simplest case, A = Fe and the redox system comprises the reduction of iron ferrite (magnetite) to ferric oxide (wustite). The TR step for this system occurs at temperatures in excess of the decomposition-melting point of Fe_3O_4. This leads to a variety of materials problems, including loss of oxide by vaporization. To solve this problem, numerous other redox systems have been proposed, including ones using mixed-metal ferrites to reduce the temperature of the TR step. Among them, the spinel systems with A = Mn [C-3], Co [C-4], Ni [C-5, C-6], and Zn [C-7, C-8] have been reported. Stabilizing these materials on yttria-stabilized zirconia (YSZ) is advantageous since it minimizes sintering and deactivation of the oxide [C-9]. Although proof-of-concept experiments support the feasibility of using these materials for hydrogen production, more detailed and quantitative information concerning the thermodynamics of the process are required to define appropriate operating conditions for such a system. Thermodynamic investigations of these systems to date have been limited in scope [C-7, C-10].

In this project, we studied the thermodynamics of three promising iron ferrite systems: A = Co, Ni, and Zn. Equilibrium calculations based on minimization of the Gibbs free energy were performed. The calculations incorporate thermodynamic data for the non-ideal solid- and liquid-phase solutions that form both the ferrites and their thermal decomposition products. The results indicate that, in contrast with the relatively simple picture of discrete oxide phase formation suggested by reactions (C-1) and (C-2), complex solution phases form in addition to the spinel and the zirconia support is not completely inert. Some of the iron in these systems forms a solution with ZrO_2, and both Fe and A form oxide solutions with each other. We also discuss O_2 partial pressures resulting from thermal oxidation, the effect of composition on the melting point, reaction efficiencies for the TR step, and hydrogen yields. The results suggest optimal conditions for material synthesis, thermal reduction, and hydrogen production.

Computational Methods

Thermodynamic calculations were performed using the FactSage program [C-11]. Thermodynamic data for solution phases were obtained from version 5.3 of the FactSage oxide solution database [C-11]. The following solutions were included in the calculations: spinel (Fe_3O_4, MFe_2O_4, and M_3O_4, M=Fe, Co, Ni, or Zn, accounting for the distribution of metal cations among octahedral and tetrahedral sites), slag (molten oxide phase: MO-FeO-Fe_2O_3), metal monoxide phase (CoO-FeO-Fe_2O_3-NiO-ZnO) and iron-zirconia phase (FeO-ZrO_2). The spinel, slag, and monoxide data are those of Pelton and coworkers for the Fe-Co-O [C-12], Fe-Ni-O [C-11], and Fe-Zn-O [C-13] systems. The Fe-ZrO_2 data are valid for ZrO_2-rich solutions. Hematite (Fe_2O_3) was included as a pure solid and its data were obtained from the Fact5.3 database. Only the cubic phase of zirconia was included in the calculations, since this form corresponds to using high-yttria (8 mole %) stabilized ZrO_2, which does not undergo phase transformation to the monoclinic and tetragonal phases at high temperatures and should thus be the most beneficial for redox production of H_2. Note, however, that the use of other forms to stabilize redox systems for H_2 production is reported in the literature, including monoclinic [C-4] and 3 mole % yttria [C-5, C-9], which includes some tetragonal phase. Using these data and the FactSage program, we can reproduce published phase diagrams for the systems of interest.

Composition of Prepared Materials

Mixed-metal ferrite materials for hydrogen production have been prepared a variety of ways, including solution methods and mixing of powders, followed by calcination at high temperatures. As-made materials are typically characterized by x-ray diffraction (XRD) and elemental analysis. Powder XRD does not have sufficient sensitivity to detect minor components; at best, a lower limit of 2 –5 wt% is typically achieved and even this can be difficult to detect in the presence of overlapping peaks or when samples are poorly crystalline. Elemental analysis only confirms that the metal content of the reactants was captured in the products. We thus performed equilibrium calculations to determine whether components other than the spinel could be present in significant quantities, and to predict the effects of varying the relative amounts of AO and FeO. As described in the methods section above, it is possible for both pure solids (e.g., Fe_2O_3) and solutions (both liquids and solids) to form from these mixtures. We simulate laboratory preparation methods by establishing the input stoichiometry with reactant mixtures containing varying amounts of FeO and MO (M=Co, Ni, Zn), with or without ZrO_2. When ZrO_2 is included, a mixture that is 80 wt% ZrO_2 is used as the reactant. The calcination step is then simulated by calculating the equilibrium composition as a function of input moles of MO, using air at 1 atm total pressure as the gas phase at a fixed temperature.

At typical calcination temperatures reported in the literature (1173 K), the calculations predict that the quantity of spinel formed increases as the relative amounts of MO and FeO approach stoichiometric spinel (i.e., n(FeO)/n(NiO) = 2, where n is the number of moles, yielding MFe_2O_4). An example is shown in figureC-1A for the Ni-Fe-O system.

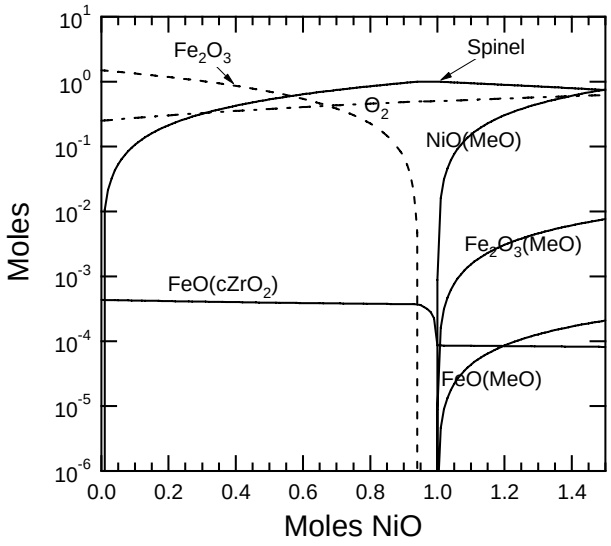

Figure C-1A. Simulation of ferrite sample preparation in air at 1173 K and 1 atm using input species amounts (moles): $N_2/ZrO_2/O_2/NiO$ = 4.0/7.78/1.0/(0 – 1.5). The plot shows equilibrium moles of phases and species within phases. Note: "Spinel" is a solid solution com-prised of 12 species; the curve for this solution is the sum of the species mole values, not simply the number of moles of $NiFe_2O_4$. "MeO" refers to a solid solution of the metal oxides FeO, Fe_2O_3, and NiO; "cZrO_2" refers to a solid solution of FeO in cubic ZrO_2.

In this series of calculations, the input moles of NiO were varied such that n(FeO) + n(NiO) = 3. For low amounts of NiO (n(NiO) < 0.55 moles), the most stable iron phase is Fe_2O_3, not the spinel. As n(NiO) increases, however, the spinel phase replaces Fe_2O_3 until the latter disappears entirely at n(NiO) = 0.94. Figure C-1B shows the elemental composition of the spinel phase, which is essentially fixed at $Ni_{0.937}Fe_{2.056}O_4$ until n(NiO) reaches 0.94, at which point the composition adjusts slightly to be essentially $NiFe_2O_4$. Similar behavior is predicted for M = Co and Zn.

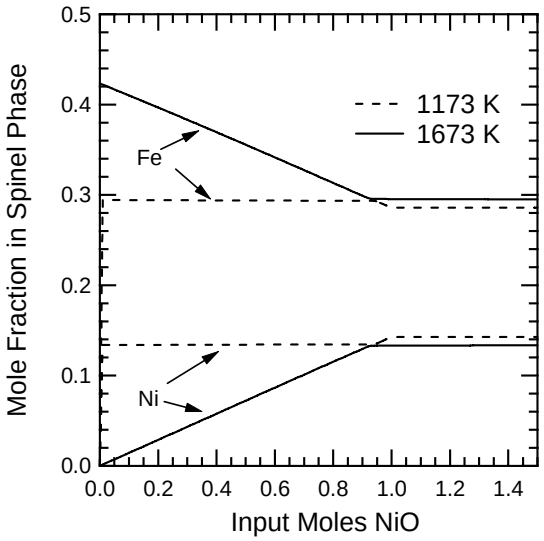

Figure C-1B. Mole fractions of the elements Fe and Ni in the spinel phase for two different calcination temperatures. Total pressure is 1 atm; input species amounts (moles): $N_2/ZrO_2/O_2/NiO/FeO$ = 4.0/7.78/1.0/(0 – 1.5)/(3.0 – 1.5).

This result indicates that at relatively low calcination temperatures, varying the relative amounts of MO and FeO does not significantly affect the composition of the spinel itself, but only changes the amount of Fe_2O_3 in the system, until the quantity of MO in the reactant mixture closely approaches that needed to make stoichiometric MFe_2O_4.

The calculations also predict, however, that increasing the calcination temperature shifts the point at which Fe_2O_3 disappears to lower *n*(MO). Using the M = Ni as an example, only the spinel phase is stable at 1673 K and no Fe_2O_3 forms at any value of *n*(NiO) up to 1.5, as seen in figure C-2.

Under these conditions, the relative amounts of Ni and Fe in the spinel vary linearly, with the mole fraction of Ni increasing with increasing *n*(NiO) (figure C-1B), until the composition $NiFe_2O_4$ is reached, at which point the relative amounts of Ni and Fe in the spinel do not change.

Regardless of the relative amounts of MO and FeO used, small amounts of FeO dissolve in the ZrO_2 support material. The amount dissolved increases with temperature and is highest when the input amount of MO is small. The ability of zirconia to form solid solutions containing iron oxides is known [C-14 C-,15] and Kodama et al. reported formation of an FeO-ZrO_2 phase during thermal reduction of Fe_3O_4 supported on YSZ [C-9]. Also, in the related manganese-iron redox system, Ehrensberger et al. reported phase segregation of Fe and Mn into wustite and spinel phases [C-16]. Again using the NiO-FeO system as an example, the mass fraction of the input FeO that becomes dissolved in ZrO_2 is predicted to be only ~ 0.01 % at 1173 K for an input *n*(FeO)/*n*(NiO) = 29. At 1673 K, however, this increases to 1.6 %. Thus, the zirconia support is not completely neutral. Once *n*(MO) exceeds 1.0, a new metal oxide phase forms. For M = Ni or Co, this phase is comprised of FeO, MO, and Fe_2O_3 in solution with each other (see figures

C-1 and C-2); when M=Zn, excess ZnO forms. Importantly, no melting is predicted over the range 1000 – 1700 K, indicating that it should be possible to maintain the mixed-metal ferrites as a powder even after high-temperature calcination.

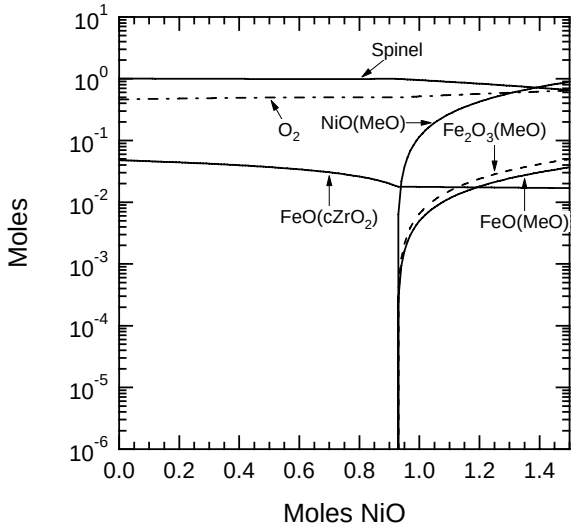

Figure C-2. Simulation of ferrite sample preparation in air at 1673 K and 1 atm using the following input species amounts (moles): $N_2/ZrO_2/O_2/NiO$ = 4.0/7.78/1.0/variable. The plot indicates the equilibrium moles of various phases and species within phases. "MeO" refers to a solid solution of the metal oxides FeO, Fe_2O_3, and NiO, while "$cZrO_2$" refers to a solid solution of FeO in cubic ZrO_2.

Thermal reduction

In the thermal reduction (TR) step (reaction 1), the ferrite is heated to a temperature sufficient to drive off oxygen, forming a mixture of reduced metal oxides. Two factors must be considered to optimize this process. First, it is desirable to maximize the equilibrium O_2 partial pressure, $p(O_2)$, at a given temperature, i.e., to maximize the conversion of ferrite to FeO. In particular, $p(O_2) \geq 0.2$ atm allows TR to occur in air or minimizes pumping power if TR is performed under a vacuum. Additionally, high $p(O_2)$ makes it easier to keep the system out of equilibrium by pumping away the gas or by sweeping it away with diluent gas, facilitating conversion of the ferrite to FeO and MO.

Second, it is probably best to select the chemical system with the highest melting point. Melting the material is advantageous in that it increases both the extent of reduction and the $p(O_2)$ at equilibrium, as will be seen below. (Note that all MFe_2O_4 spinels melt incongruently, i.e., they decompose, forming a liquid solution of various oxides and O_2 gas.) However, the formation of molten material may also lead to material problems such as corrosion and formation of solid materials with low permeability, thereby limiting the ability of gases to escape and steam to penetrate during the water oxidation step. This problem makes Fe_3O_4 unattractive for hydrogen production via solar redox. In general, it is best to operate at the highest temperature practical, since this leads to higher $p(O_2)$, shifts the equilibrium toward FeO,

and increases the kinetics of the reduction. The equilibrium calculations allow us to address both of these points.

Thermodynamic calculations suggest that the nickel ferrite system is the best of the three considered here with respect to optimizing the factors just discussed. As seen in figure C-3, fixed-volume and temperature calculations for the M-Fe (M = Fe, Co, Ni, Zn) ferrite systems predict that it is possible to achieve $p(O_2) \geq 0.2$ atm for all four metals, but that the most favorable conditions exist for M = Ni.

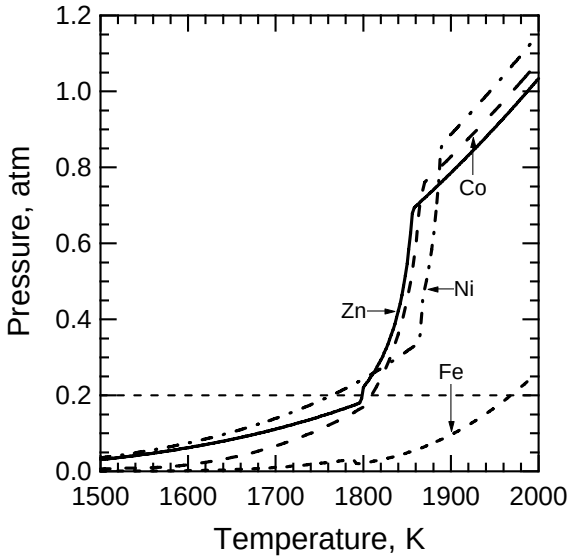

Figure C-3. Total system pressure at equilibrium for thermal reduction. Since essentially 100% of the gas is O_2, this is essentially equivalent to $p(O_2)$. The total volume of the system is 20 cm^3. The input mixture for the calculation simulates a sample of ferrite obtained by calcining 0.2 g of MFe_2O_4 in 0.8 g cubic ZrO_2 at 1173 K and 1 atm. The resulting mixture of phases predicted by Factsage is approximately 20 wt% spinel.

For this metal, the O_2 partial pressure exceeds 0.2 atm at a temperature of only 1760 K for a system volume V of 20 cm^3. In contrast, iron spinel, Fe_3O_4, does not achieve $p(O_2) \geq 0.2$ atm until temperatures in excess of 1970 K, well above the predicted temperature (1800 K at V = 20 cm^3) at which it decomposes and forms a molten phase. (Note: this calculated decomposition temperature is lower than that typically reported for Fe_3O_4, ~ 1870 K, because the fixed volume used here shifts $p(O_2)$ to lower a value than predicted by a 1 atm, fixed-pressure calculation). These results are consistent with the general experimental observation that mixed-metal ferrites can be thermally reduced at lower temperatures than Fe_3O_4 and without melting. In particular however, they agree with the observation of Aoki et al. that the nickel-ferrite system can be reduced in air at 1800 K, yielding a mixture of spinel and nickel-iron wustite phases [C-6], The other two ferrites, M = Co and Zn, also reach 0.2 atm at much lower temperatures than Fe_3O_4, but this occurs at roughly the same temperature as the onset of the decomposition of a molten phase (also ~ 1800 K). The nickel ferrite, on the other hand, has the highest decomposition-melting

temperature of the four ferrite systems (~1860 K under these conditions; ~1875 K in the absence of ZrO_2).

Corresponding to its higher equilibrium $p(O_2)$, nickel ferrite also reduces to the greatest extent compared with the other three ferrites. This is illustrated in figure C-4, in which the percent decomposition (mass basis) at equilibrium for all four spinels is plotted versus temperature.

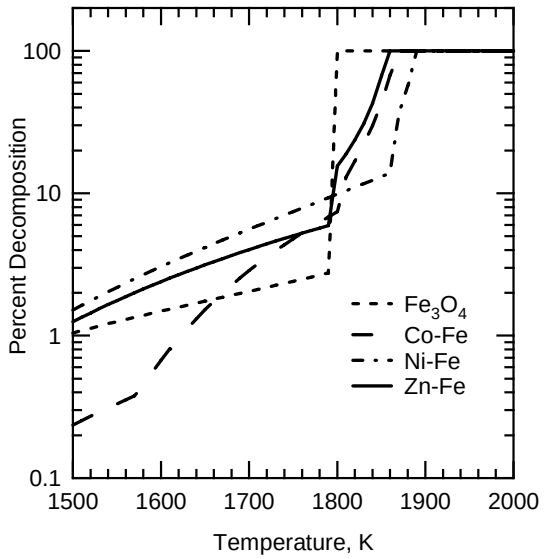

Figure C- 4. Percent decomposition by thermal reduction (mass basis; total mass of the metal oxide portion of the system is 0.2 g) of the input spinel phase corresponding to the calculations exhibited in figure C-3 as a function of temperature.

The distinct jumps in the amount of spinel decomposition correspond in each case to the point at which the liquid slag phase forms. As can be seen in the figure, the nickel ferrite exhibits the highest percent decomposition at all temperatures below its melting point. At 1773 K, just below the melting point of the Fe, Co, and Zn spinel solid solutions, the percent decomposition of the nickel spinel exceeds the Co and Zn solutions by a factor of ~ 1.5, while the difference is a factor of 3.2 in the case of Fe_3O_4 (8.3% vs. 2.6%).

The results in figure C-4 also show that all of the spinels are stable to some extent below their melting points. Complete decomposition does not occur until a temperature at which a molten slag phase forms. This indicates that to fully reduce any of these materials without melting requires the system to be kept out of equilibrium, so that reaction 1 is always spontaneous ($\Delta G° < 0$) in the forward direction. From a practical standpoint, this means that the gas above the ferrite material must either be diluted or the total pressure reduced so that $p(O_2)$ is always less than its equilibrium value. Thus, the extent of reduction shown in figure C-4 is an indication of the thermodynamic driving force for the reaction, not necessarily a

measure of the efficiency of reaction 1. The observed extent of TR will depend on kinetics and the extent to which the system can be kept out of equilibrium.

Water Oxidation

Efficient hydrogen production via reaction (C-2) places several requirements on the system. Of course, the reaction must be spontaneous at the temperature of the water oxidation (WO) step for H_2 to be produced. Additionally, however, it desirable that WO conditions exist such that the spinel phase is the most stable one, so that all of the reduced material formed in reaction 1 can be readily reconverted to spinel. Like the TR step, the WO step should occur below the melting point so that no loss of permeability occurs. These conditions can be met by all of the materials examined here. For the purposes of discussion, we will focus on the nickel system, since its properties appear to be the most favorable for hydrogen production.

As mentioned in the previous section, the nickel ferrite forms a solid solution of oxides (nickel, ferric, and ferrous oxides) in the thermal reduction step. Upon exposure to an excess of steam at elevated temperature, the oxides of the monoxide solid solution (composed of FeO, NiO, and Fe_2O_3) are largely oxidized to spinel. For illustration we consider the mixture of phases resulting from thermal reduction of 1.0 g of pure $NiFe_2O_4$ at 1875 K (again at a total system volume of 20 cm^3); we will refer to this mixture as NiFeO_TR1875. At 1875 K, which is below the predicted melting point of 1970 K, ~ 10% of the mass of the $NiFe_2O_4$ is reduced at equilibrium and must be reoxidized during the WO step to achieve the maximum H_2 production. Reacting NiFeO_TR1875 with a large excess (1000 g) of steam at 1 atm simulates WO. The various components in the mixture and the amounts of H_2 and O_2 produced by the WO step are plotted as a function of temperature in figure C-5.

It is evident from the small amounts of the monoxide solution components (indicated by MeO in figure C-5) that they are not stable under these conditions and revert almost completely to spinel. These predictions are consistent with measurements reported by Aoki et al. [C-6], whose results indicate that the WO step is fast and yields 90% of the theoretically possible amount of H_2. A slight decrease in the stability of the spinel with temperature is predicted, however, as evidenced by the increasing amounts of monoxide solution components with temperature, although greater than 94 % of the mass in this temperature range consists of spinel. Nevertheless, the result indicates that it is preferable to operate the WO step at as low a temperature as possible, heating the system only enough to achieve reasonable reaction rates.

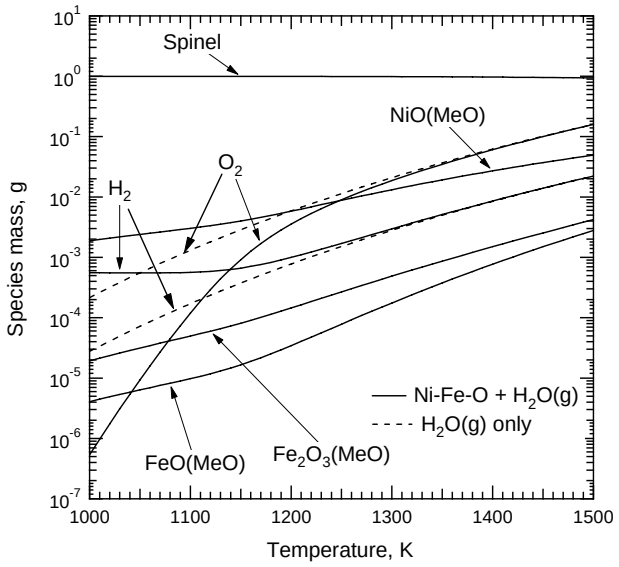

Figure C-5. Composition of the solid and gas phase resulting from water oxidation in excess steam as a function of temperature (P_{tot} = 1 atm), using the mixture of nickel and iron oxides formed by thermal reduction of 1.0 g of $NiFe_2O_4$ at 1875 K (designated NiFeO_TR1875).

The results in figure C-5 clearly show that H_2 is produced as a result of the reoxidation of NiFeO_TR1875 and is not simply due to dissociation of small amounts of H_2O. At temperatures up to about 1150 K, the amount of H_2 formed in the presence of NiFeO_TR1875 (solid line for H_2) is significantly higher than the amount formed when only steam is included in the calculation (dashed line for H_2). Note also that very little O_2 is present at these temperatures, indicating that oxygen from H_2O is consumed by reoxidizing the metal oxides. Above 1150 K, however, both H_2 and O_2 begin to increase. Furthermore, the amounts of these gases approach the curves produced with only steam (dashed lines), showing that additional H_2 production at these temperatures is due to dissociation of H_2O. Whether this prediction would be realized in an actual production system is unclear, since kinetic factors could well limit its extent. The prediction suggests, however, that there is an optimal temperature that maximizes H_2 production while minimizing or eliminating O_2. The presence of significant amounts of O_2 in the H_2 stream presents not only a potential safety hazard, but also a separations problem, since the O_2 would have to be removed before the H_2 could be used as a fuel.

Conclusions

The equilibrium calculations presented here provide numerous insights into the production of hydrogen via thermal redox process. Although complete equilibrium may not be achieved in an actual process, the high temperatures used, particularly in the TR step, make it likely that at a minimum, the trends predicted here will be reproduced in a physical system and thus be useful in guiding process development.

Four key conclusions are reached as a result of this study. First, the nickel ferrite system, nominally $NiFe_2O_4$, displays the best combination of properties relative to the other three chemical systems examined. In particular, the nickel ferrite melts at the highest temperature and has the highest equilibrium O_2 partial pressure of any of the systems in the solid states. These properties minimize material problems by avoiding the formation of liquid-phase reduction products while maximizing the stability of the reduced oxides. Second, the equilibrium composition of the prepared material can depend strongly on the calcination temperature. Low temperatures tend to favor mixtures of spinel and Fe_2O_3. In the presence of Fe_2O_3 the composition of the spinel (i.e., the M/Fe atomic ratio) is constant until the MO/FeO ratio reaches the point at which all of the Fe_2O_3 is consumed. The amount of MO required to reach this point also depends on temperature. Third, operating the TR step at the highest practical temperature is advantageous, since this leads to higher $p(O_2)$, shifts the equilibrium toward FeO, and increases the rate of the reduction reaction. Finally, the WO step is thermodynamically most efficient at low temperatures (1000 – 1150 K), converting essentially all of the available FeO and MO to H_2 and reforming the spinel. Higher temperatures may lead to some formation of O_2 due to dissociation of H_2O.

References

C-1. Steinfeld, A., 2005, "Solar thermochemical production of hydrogen--a review," Solar En. 78, 603.

C-2. Kodama, T., 2003, "High-temperature solar chemistry for converting solar heat to chemical fuels," Prog. En. Comb. Sci. 29, 567.

C-3. Ehrensberger, K., Frei, A., Kuhn, P., Oswald, H. R., and Hug, P., 1995, "Comparative experimental investigations of the water-splitting reaction with iron oxide $Fe_{1-y}O$ and iron manganese oxides $(Fe_{1-x}Mn_x)_{1-y}O$," Sol. St. Ionics 78, 151.

C-4. Kodama, T., Kondoh, Y., Yamamoto, R., Andou, H., and Satou, N., 2005, "Thermochemical hydrogen production by a redox system of ZrO_2-supported Co(II)-ferrite," Solar En. 78, 623.

C-5. Ishihara, H., Kaneko, H., Yokoyama, T., Fuse, A., Hasegawa, N., and Tamaura, Y., 2005, "Hydrogen production through two-step water splitting using YSZ (Ni,Fe) system for solar hydrogen production," ISEC2005, ASME, Orlando, FL.

C-6. Aoki, H., Kaneko, H., Hasegawa, N., Ishihara, H., Takahashi, Y., Suzuki, A., and Tamaura, Y., 2004, "Two-step water splitting with Ni-Ferrite system for Solar H_2 production using concentrated solar radiation," ISEC 2004, Portland, OR.

C-7. Tamaura, Y., Kojima, N., Hasegawa, N., Inoue, M., Uehara, R., Gokon, N., and Kaneko, H., 2001, "Stoichiometric studies of H_2 generation reaction for $H_2O/Zn/Fe_3O_4$," Int. J. Hydrogen En. 26, 917.

C-8. Tamaura, Y., and Kaneko, H., 2005, "Oxygen-releasing step of $ZnFe_2O_4/(ZnO+Fe_3O_4)$-system in air using concentration solar energy for solar hydrogen production," Solar En. 78, 616.

C-9. Kodama, T., Nakamuro, Y., Mizuno, T., and Yamamoto, R., 2004, "A two-step thermochemical water splitting by iron-oxide on stabilized zirconia," ISEC2004, ASME, Portland, OR.

C-10. Lundberg, M., 1993, "Model calculations on some feasible two-step water splitting processes," Int. J. Hydrogen En. 18, 369.

C-11. Bale, C. W., Chartrand, P., Degterov, S. A., Eriksson, G., Hack, K., Mahfoud, R. B., Melançon, J., Pelton, A. D., and Petersen, S., 2002, "FactSage Thermochemical Software and Databases," Calphad 26, 189.

C-12. Jung, I.-H., Decterov, S. A., Pelton, A. D., Kim, H.-M., and Kang, Y.-B., 2004, "Thermodynamic evaluation and modeling of the Fe-Co-O system," Acta Mat. 52, 507.

C-13. Degterov, S. A., Jak, E., Hayes, P. C., and Pelton, A. D., 2001, "Experimental study of phase equilibria and thermodynamic optimization of the Fe-Zn-O system," Met. Mat. Trans. B 32B, 643.

C-14. *Phase Diagrams for Ceramists*; Vols. 1-12, The American Ceramic Society: Westerville, OH, 1964-1996; Vol. 1-12.

C-15. Kiminami, R. H. G. A., 1988, Ceramica (Sao Paulo) 34, 121.

C-16. Ehrensberger, K., Kuhn, P., Shklover, V., and Oswald, H. R., 1996, "Temporary phase segregation processes during the oxidation of $(Fe_{0.7}Mn_{0.3})_{0.99}O$ in N_2-H_2O atmosphere," Sol. St. Ionics 90, 75.

APPENDIX D

FERRITE MATERIAL STUDIES

Appendix D - Ferrite Materials Studies

The CR5 design, although quite attractive for achieving high efficiency (calculations suggest 50% thermal efficiency is possible (see Appendix B), and continuous operation, is very demanding of the reactive oxide working material. From a chemistry point of view it is essential for the Gibbs free energy of reaction (ΔG) to be negative (i.e. the reaction to be thermodynamically favorable) for both the TR and WO steps at reasonable temperatures and for the high temperature TR step to couple well with the energy source. For Concentrating Solar Power (CSP), this implies a temperature for TR >1000 °C. It is possible of course to compensate for unfavorable thermodynamics by providing additional work to the system, although the overall system efficiency will suffer. For example, the reactions can be driven forward by keeping the system from reaching equilibrium with an inert sweep gas (this will require a separation to be performed) or similarly by operating at reduced pressure. A closely related requirement is that the solid working material must not melt or volatilize under either reaction condition. Furthermore, the chemistry must be repeatable over thousands, if not millions, of cycles. This implies that there must not be any thermodynamically or kinetically stable phases that can potentially trap the material in an inactive form. In addition to these basic chemical requirements it is desirable for the overall reaction kinetics to be as rapid as possible. That is, the surface reaction and transport of ions in and out of the bulk oxide to the reacting surface should be as rapid as possible.

From an engineering design standpoint, the working oxide must be amenable to fabrication into physical forms that can be integrated into the engine design concept. High volumetric and mass utilization of the working material is important to achieving high efficiency, even with the recuperation aspect of the CR5 design. Thus, the physical form of the metal oxide should have a high surface to volume ratio. The physical form should also be relatively open to allow gaseous transport and light penetration for direct solar heating. The parts must not physically or chemically degrade over thousands or millions of cycles and thus should be resistant to thermal shocking, have relatively small volumetric changes with changes in temperature or phase, and should be compatible with the other materials of construction.

Baseline Material Selection

The test apparatus and our initial results of the water splitting evaluations for the as-prepared materials are shown in figure 3 and Table 1, respectively, in the main report. The temperatures for the two reaction steps are also in Table 1. Based on older literature reports of relatively low cycle temperatures for water splitting over nickel/manganese-substituted ferrites, our first studies were conducted at 1100 and 800 °C [D-1, D-2]. Consistent with more current literature, cycle temperatures were shifted upward for the cobalt- and nickel-substituted samples [D-3, D-4]. Note that in all cases the

reduction temperatures are high enough that any minor impurities (e.g. Fe_2O_3) in the as-prepared material should no longer be present.

The as-prepared $Mn_{O.36}Fe_{2.64}O_4$ generated a large amount of oxygen during thermal reduction (ca. 15 cm^3/g), but almost no hydrogen during subsequent exposure to water vapor. This behavior is consistent with the presence of a distinct manganese oxide phase in the as-prepared material, although such a phase was not apparent in the XRD patterns. Nonetheless, the formation of this hypothetical phase might be avoided by altering the preparation procedure. Furthermore, reevaluating this material at higher temperatures might improve the results. However, given that the literature indicates that manganese-substituted ferrites are inferior to cobalt-substituted materials [D-4], further efforts with this material were considered to be inconsistent with our goals.

The results for the $Ni_{0.5}Mn_{0.5}Fe_2O_4$ were also disappointing. In contrast to very promising results in the literature [D-1], only a amount of oxygen was produced in our lab by this material (0.75 cm^3/g), and no hydrogen was evolved. A related formulation, $Ni_{0.39}Mn_{0.35}Fe_{2.26}O_4$, containing sub-stoichiometric amounts of Mn and Ni (i.e. some of the Fe would be expected to be Fe(II)) gave better results. Large quantities of hydrogen were generated by the as-prepared material in the first water splitting cycle, with less produced in each successive cycle. This prompted additional work wherein the $Ni_{0.39}Mn_{0.35}Fe_{2.26}O_4$ was physically mixed in a 1:3 weight ratio with yttria stabilized zirconia (YSZ). The YSZ improved, but did not entirely eliminate, loss of activity over several cycles (a 28 % loss in H_2 yield across three cycles for the stabilized material compared to a > 90 % loss for unstabilized materials). Also troubling was the fact that we observed very little oxygen evolution during the reduction steps, suggesting the possibility of an unsustainable stoichiometric reaction. Poor sample to sample reproducibility was also a concern.

Compared to the best $Ni_{0.39}Mn_{0.35}Fe_{2.26}O_4$ results, the $Co_{0.67}Fe_{2.33}O_4$ material produced relatively little hydrogen or oxygen. However, both products were consistently detected over several consecutive cycles. The addition of YSZ slightly improved the hydrogen yield, and stabilized the results through numerous cycles. Both product gasses were also realized over $Ni_{0.67}Fe_{2.33}O_4$, and an initial improvement in hydrogen yield was realized by the addition of YSZ. However, the YSZ did not appear to stabilize the $Ni_{0.67}Fe_{2.33}O_4$, to the same degree as for $Co_{0.67}Fe_{2.33}O_4$ (in one test with $Ni_{0.67}Fe_{2.33}O_4$, 75 % loss in hydrogen was observed from the first to second cycle and an additional 30 % in the next cycle). Based on these results $Co_{0.67}Fe_{2.33}O_4$ blended with YSZ in a 1:3 weight ratio was selected as the baseline material for further process development.

Oxide Synthesis and Monolith Construction

Synthesis of $Co_{0.67}Fe_{2.33}O_4$ was achieved through co-precipitation of the metals from nitrate solutions with ammonium hydroxide. After aging, the solids were filtered, washed with deionized water, dried in a vacuum oven overnight at 80 °C, and then typically calcined for 2 hrs at 1100 °C in air. The calcined

ferrites were typically milled to reduce particle size to about an 11 μm average prior to testing. YSZ was used as-received from Tosoh (3 mol% Y_2O_3, 0.63 μm average particle size, unless otherwise specified). Al_2O_3 (Sasol Puralox) and TiO_2 (Degussa P-25) were used as received. HfO_2 and Y-doped HfO_2 (10 mol% Y_2O_3) were synthesized by NH_4OH precipitation from solutions of $HfOCl_2$ and $HfOCl_2$ with $Y(NO_3)_3$ respectively, followed by filtration, washing, drying, and calcination at 1100 °C.

Previous attempts at "reactorizing" ferrite powers have focused on the difficult task of supporting the ferrite on an inert monolithic substrate, e.g. SiC [D-5]. Our approach is to directly fabricate the powders into monolithic structures. This circumvents the need to consider the chemical compatibilities of the ferrite and substrate. This is quite important as prior experience has shown us that even very stable oxides such as hexaaluminates can interact with ceramic substrates at high temperatures in ways that are difficult to characterize, but nonetheless deleterious to performance [D-6]. Direct fabrication of ferrite into monolith also avoids problems such as thermal mismatch between substrate and powder coating, and allows for higher volumetric loading of the reactive material.

Physical mixtures of the ferrite powder with the support were fabricated directly into monolithic structures for testing using two different methods. The robocasting technique, developed at Sandia National Laboratories [D-7], was used to fabricate monoliths consisting of a series of rods arranged in a face-centered cubic-like geometry (figure D-1A) that offers no line-of-sight pathways, yet provides three-dimensional interconnectivity of the void spaces [D-8]. Two sub-types of monoliths were cast with this technique, those designed to have dense, non-porous rods after firing at 1425 °C (figure D-1C), and those in which spherical polymethylmethacrylate (PMMA) pore former was added during the manufacture to produce a part that was nominally 75 % void space (figure D-1D). This addition required adjustment of feature sizes (rod diameters) to accommodate the larger particles. The second type of monolith was fabricated using the same slurry as the robocasting technique. In this case, however, the slurry with added pore former (75% targeted porosity) was simply poured into a cylindrical mold, allowed to dry at room temperature and then removed from the mold and fired at a temperature of at least 1400 °C. The flat faces of the resulting disk were then ground on a bench grinder to expose the porosity (figure D-1B). Typical specifications for these monoliths are given in Table D-1. Monoliths containing other materials (Al_2O_3, TiO_2, HfO_2 and Y-HfO_2) were fabricated with similar dimensions to those in Table 1 using the second technique with the amounts of ferrite and "support" adjusted to maintain a constant volume ratio (1:3 $Co_{0.67}Fe_{2.33}O_4$/YSZ by weight is equivalent to about 1:2.6 by volume).

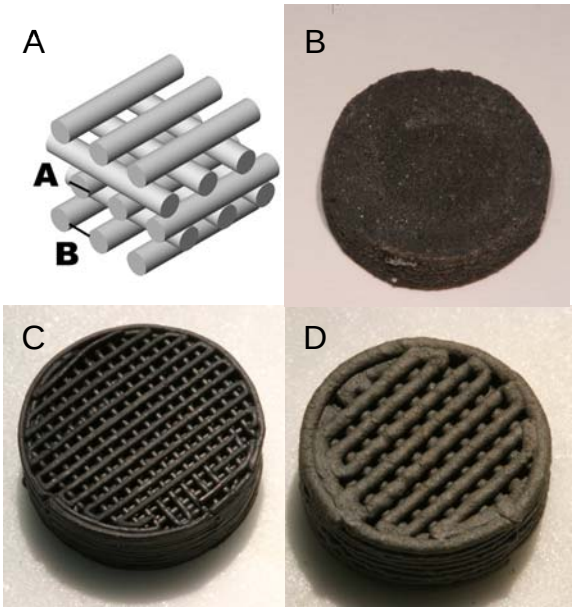

Figure D-1. Monolithic structures of 1:3 $Co_{0.67}Fe_{2.33}O_4$/YSZ. A) schematic of robocast lattice structure. B) Cast monolith with ground faces. C) Robocast lattice with dense rods. D) Robocast lattice with porous rods.

Table D-1. Typical specifications for $Co_{0.67}Fe_{2.33}O_4$/YSZ (1:3 by weight) monoliths.

	Cast Monolith	Robocast Dense Monolith	Robocast Porous Monolith
Thickness (mm)	4.1	5.1	5.4
Diameter (mm)	15	15.4	15.3
Rod Size (mm)	N/A	0.45	0.91
Weight (g)	1.80	2.80	1.56
PMMA Size (mm)	0.035 average	N/A	0.035 average

Water Splitting Reaction

The water splitting reaction was carried out in a typical laboratory-scale flow reactor consisting of a 2.53 cm O.D. by 66 cm long mullite tube situated in a high temperature furnace. The ferrite composite disks are supported in the tube by plugs of refractory wool so that gas flow must pass through the thickness of the disk via the porous networks provided by the lattice structure or pore former. Argon and helium (ca. 60 sccm) are used to sweep the reactor during the WO and TR phases of water splitting, respectively. The different sweep gasses facilitate chemical analysis of the reactor effluent by gas chromatography using a thermal conductivity detector. The argon flow is split so that it can function either as an inert purge or be humidified by a saturator operated at 80-90 °C prior to entering the reaction zone. Gas samples are collected and analyzed at 2 min intervals during WO and TR cycles. Background oxygen levels in the system are typically measured to be between 20-100 ppm.

The "standard operating cycle" is outlined in Table D-2. Each reaction is monitored and allowed to proceed until gas evolution returns to near baseline with this method and thus it provides a measure of the maximum yield or (material utilization) that can be achieved with the monolith under the stated conditions. A limitation of the standard operating protocol is that samples can be cycled no more than one or two times each working day. Also, the long duration of each reaction step, long purge times, and slow ramp rates arising from the large thermal mass of the system are inconsistent with the CR5 design which requires an operating speed of about 1 rpm to maintain temperature differences across the two reaction chambers. Thus, additional methods were adopted to provide some insight into the time dependence of the yields and to shorten the time required to cycle a given sample a significant number of times. Typically, the shorter cycles involved reducing the sample in Ar rather than He for a defined time period, and then exposing the sample to steam at the WO temperature for a defined time period or until H_2 evolution was complete (Table D-2). In these cases, O_2 yields could not be determined. Typically, the standard procedure was performed at the beginning of a given test to establish a baseline, and then again on occasion throughout the run to provide an indication of any changes that have occurred as a result of cycling the sample. The sample was allowed to cool under flowing inert gas following the final WO step of a work day.

Table D-2. Operating cycles for water splitting reactor.

Step	Standard Procedure	Alternate Procedure
1	Purge with He	Purge with Ar
2 -TR	Ramp to1400 °C	Ramp to1400 °C
3-TR	Hold until O_2 evolution is complete (1.5-3 hrs)	Hold for specified time
4	Purge with Ar	N/A
5-WO	Initiate steam flow	Initiate steam flow
6-WO	Ramp 1400-1100 °C	Ramp 1400-1100 °C
7-WO	Hold until H_2 evolution is complete (1.5-3 hrs)	Hold until H_2 evolution is complete (30 min)
8	Repeat or cool and idle overnight	Repeat or idle

Activity over Numerous Cycles

Kodama and coworkers established that mixing ferrite powders with ZrO_2 or YSZ powders, typically in about a 1:3 weight ratio, results in a material that can repeatedly produce H_2 over numerous cycles without extensively grinding the material between each step [D-9]. We sought to expand on this finding by establishing that solid, monolithic parts fabricated from similar composites will also produce H_2 over repeated cycles. Figure D-2 summarizes the results for a cast pellet of 1:3 $Co_{0.67}Fe_{2.33}O_4$/YSZ with the specifications given in Table D-1. Figure D-2 clearly shows that the material is active for at least 14 cycles, and that H_2 can be produced even with very short reduction times. This is a result of the fact that the rate of thermal reduction is greatest in the initial stages, as one would expect. Additionally the data shows that there is no loss in H_2 production potential with cycling for at least 8 cycles (the last standard

cycle). In fact the H_2 yields in the standard cycle show some improvement with cycling. As will be seen below, this is a consistent, but not well understood observation. For comparison purposes we also performed an experiment with a similar 1.46 g disk constructed wholly of $Co_{0.67}Fe_{2.33}O_4$. In this case, 30 min reduction cycles resulted in the production of only 0.05 cm^3 H_2/g ferrite in the first cycle and no detectable H_2 in the second cycle. The positive effect of the added zirconia support clearly carries over to monolithic parts.

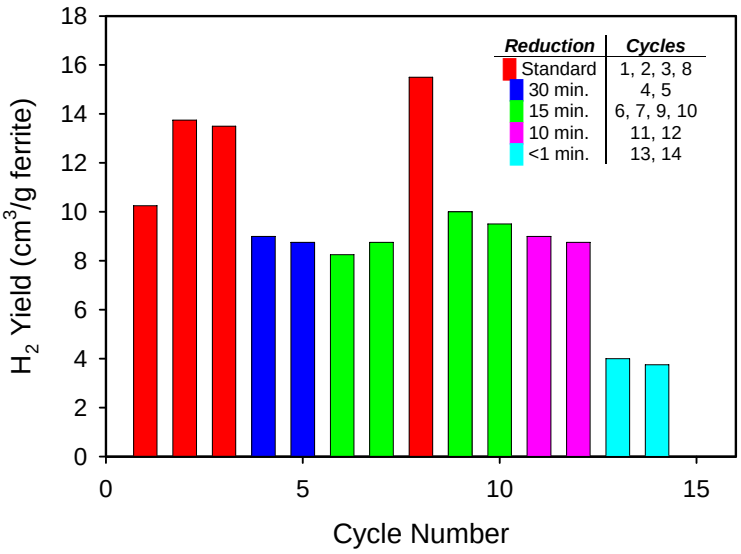

Figure D-2. Hydrogen yields for each water oxidation carried out with a cast $Co_{0.67}Fe_{2.33}O_4$/YSZ monolith.

Compatibility with Other Supports and Materials

Although constructing monoliths directly from the active ferrite/zirconia composite avoids many compatibility and reactivity issues, problems may still arise for example in places where the monoliths are joined to other reactor parts. Additionally, it is of interest to establish whether the support effect is unique to zirconia, or applies to other materials as well. Tests were carried out with disks cast from $Co_{0.67}Fe_{2.33}O_4$ mixed with either Al_2O_3 or TiO_2 in the standard 1:2.6 volume ratio. As shown in Table D-3, O_2 was produced over both materials in each of the 4 TR cycles attempted. However, virtually no H_2 was produced during the corresponding WO steps. We posit that the O_2 is produced as the result of a solid state reaction between the ferrite and support with spinels (e.g. $FeAl_2O_4$ and Fe_2TiO_4) as likely products. We were unable to confirm these reactions by powder X-ray diffraction analysis of the post-reaction monoliths (samples were characterized after crushing and after grinding to a fine powder.) However, in other tests we have witnessed catastrophic reactive failure of $Co_{0.67}Fe_{2.33}O_4$/YSZ monoliths that were calcined in contact with alumina fiber board or boats at temperatures in excess of ca. 1500 °C.

Table D-3. Results of standard water splitting cycles over cast $Co_{0.67}Fe_{2.33}O_4/Al_2O_3$ and $Co_{0.67}Fe_{2.33}O_4$ /TiO_2 monoliths.

Cycle Number	$Co_{0.67}Fe_{2.33}O_4/Al_2O_3$		$Co_{0.67}Fe_{2.33}O_4/TiO_2$	
	O_2 Produced (cm^3/g ferrite)	H_2 produced (cm^3/g ferrite)	O_2 Produced (cm^3/g ferrite)	H_2 produced (cm^3/g ferrite)
1	3.8	0.00	14.9	0.15
2	2.6	0.48	12.3	0.32
3	5.6	0.48	6.5	0.05
4	6.2	0.22	4.9	0.00

In an additional set of experiments monoliths were cast from mixtures of $Co_{0.67}Fe_{2.33}O_4$ with either HfO_2 or Y-doped HfO_2 in the standard volume ratio. The chemical properties of HfO_2 are similar to those of ZrO_2; Y-doping introduces vacancies into both ZrO_2 and HfO_2 thereby enhancing oxygen conductivity within the solid. However, unlike ZrO_2, HfO_2 is cubic with or without added Y_2O_3. The results for these monoliths are summarized in figure D-3. Both materials produced H_2 over the 15 cycles tested, with the yields in the final standard cycles approximating those in the early cycles. The results do suggest differences in the materials however. The yields are greater and more consistent for the Y-containing sample. Also, yields over the Y-free sample appear to be somewhat independent of reduction time. Taken together this could be an indication that the reaction for the Y-free sample is limited to the outer surfaces of the material and suggests exploring the relationship between oxygen conductivity and ferrite utilization as a potentially fruitful exercise.

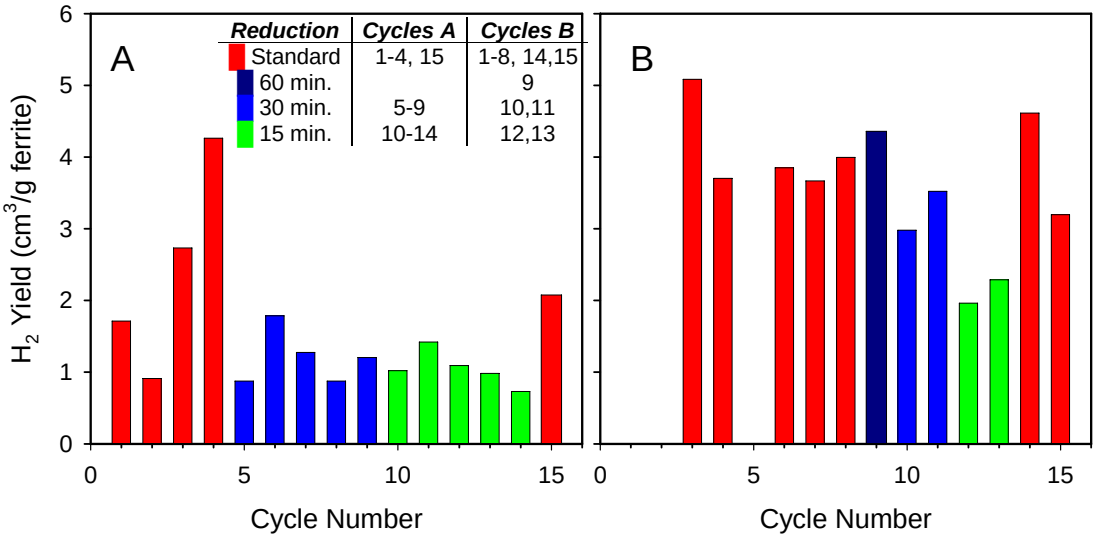

Figure D-3. Hydrogen yields for each water oxidation step carried out with cast ferrite/hafnia monoliths A) $Co_{0.67}Fe_{2.33}O_4/HfO_2$ B) $Co_{0.67}Fe_{2.33}O_4$/Y-doped HfO_2

Integration with CR5 Design Concept

The robocasting method provides a route to directly produce monolithic structures with volumetric surface areas comparable to those of commercial extruded monoliths, but with the added benefits of channel to channel connectivity, no line of sight pathways, piece to piece consistency, and no constrictions to flow as are present in foam-like monoliths or our cast disks [D-8]. A photograph of a Robocast reactant ring is shown in figure 5 in the main report. Small disks constructed with the lattice geometry that is integral to the current ring design were tested in our laboratory reactor to begin to establish the suitability of the robocasting technique and the lattice design for the CR5 application.

The results for the dense and porous monoliths described in Table D-1 are summarized in figure D-4 and figure 4 in the main report, respectively. Cycles 3-8 for the porous sample (figure 4 in the main report) were conducted in a unique fashion and will be discussed below. On the whole, the results are very encouraging. The dense sample was cycled 36 times and the porous sample was cycled 31 times, and in both cases the H_2 yield in the final standard cycle exceeded that of the earlier cycles. Additionally both samples remained mechanically sound throughout the length of the test. Under the standard conditions, the H_2 yields were greater over the dense monolith than over the porous monolith. The yields were more similar when the TR period was shortened. For shorter reduction times the reaction should be more limited to surface regions and thus this outcome indicates that the pore former did not improve ferrite utilization by providing greater surface area and access to the core of the composite rods as was hoped. This may be explained by the fact that on close inspection of the porous rods comprising the monolith the pore structure was found to have relatively little connectivity to the outer surfaces, probably because wall effects excluded the pore former from these regions during the extrusion process.

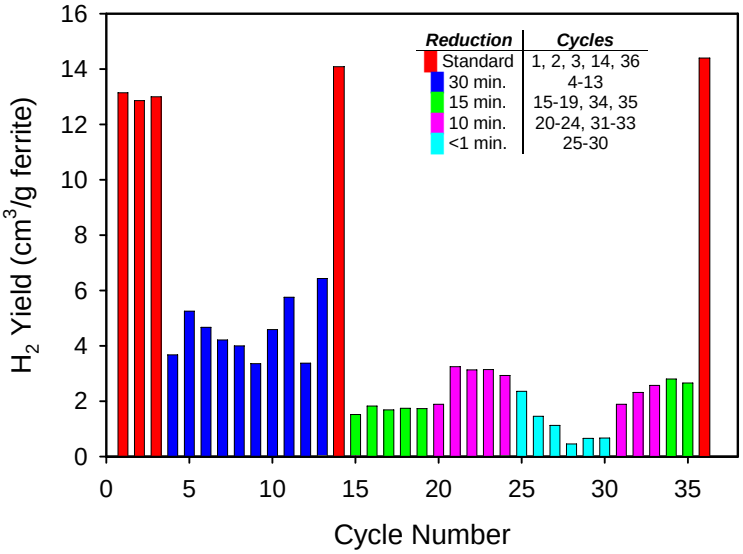

Figure D-4. Hydrogen yields for each water oxidation step carried out over a dense Co0.67Fe2.33O4/YSZ monolith.

Physical changes were evident in the porous sample after testing. The monolith shrunk during testing with of decrease of 18% in the diameter. Migration and coalescence of the small ferrite particles evidently occurred in parallel with the collapse of the porosity. The sample was uniformly black in color at the onset of the test, but it had taken on a "salt and pepper" appearance by the end the evaluation with distinct black particles visible against a white or grey background. It is interesting that the apparent increase in ferrite particle size did not result in a decrease in H_2 yield.

Ferrite Utilization Efficiency

In any test performed to date with a dense robocast monolith, the highest utilization efficiency achieved during a standard cycle was 22%. That is, the gas yield relative to the theoretical maximum gas yield (95 cm^3 H_2/g $Co_{0.67}Fe_{2.33}O_4$ at STP) was only 22%. It is straightforward to calculate a "penetration depth" of the reaction into the monolith rods from this number if one assumes that there is no geometric surface area lost where the rods overlap one another. If one assumes an extent of reaction of 100%, i.e. that any portion of the ferrite that reacts fully reduces from $Co_{0.67}Fe_{2.33}O_4$ to CoO and FeO and back, then the reaction must penetrate 26 μm into the 450μm rod to achieve 22% utilization. If more reasonable reaction extents of 50% or 25% are assumed, then the calculated penetration depths increase to 56 μm and 150 μm respectively. For this monolith the average ferrite particle size prior to fabrication was 11 μm with 12 μm standard deviation.

The simple calculation shows that, even in the worst case, the sampling depth was greater than the average particle size, and suggests the intriguing possibility that interior particles (i.e. those without direct connectivity to the surface) in some way communicate with the surface and are available to react. A possible mechanism for this might involve transport of oxygen through vacancies in the YSZ phase. Alternate explanations include the possibility of gas transport through networks of micro-porosity or the formation of limited ferrite networks that connect to the surface (the ferrite loading is below the theoretical percolation limit). Additional experiments with variable rod sizes and particle sizes are planned to provide greater insight into this question.

The impact of ferrite loading on utilization was addressed by robocasting a series of dense $Co_{0.67}Fe_{2.33}O_4$/YSZ monoliths with ferrite:zirconia weight ratios of 1:10, 1:5, 1:4, 1:3, 1:2 , and 1:1.75. A 1:3 sample with 8% Y_2O_3 stabilized zirconia (as opposed to the standard 3%) was also fabricated. The $Co_{0.67}Fe_{2.33}O_4$ in each sample was all taken from the same large batch of material. The monoliths were each subjected to a mix of up to 11 standard cycles and alternate cycles. No patterns emerged in ferrite utilization efficiency; differences between the samples were generally within the range of cycle to cycle variability typically seen, with one exception. The sample with the highest ferrite loading (1:1.75 by weight) appeared to losing activity with cycling; the final standard cycle over this sample, the eleventh

cycle overall, produced only half the H_2 of the first cycle. It may be significant that this material should be bi-continuous with the ferrite forming a percolating network rather than existing as isolated particles in a YSZ matrix. One would expect the positive support effect to diminish at high ferrite loadings, particularly once the ferrite particles can form a continuous phase.

Reaction Rate Considerations

Figure D-5 shows O_2 and H_2 evolution as a function of time during the final standard cycle for the dense $Co_{0.67}Fe_{2.33}O_4$/YSZ monolith discussed above (cycle 36, figure D-4). Ideally, one would expect these curves to exhibit an initial high rate of reaction (gas evolution) associated with the surface and near surface and possibly a plateau at that rate if kinetics or mass transfer were slow relative to the number of these sites, and then a slow decline in reaction rate as bulk reaction and transport become necessary. In our case, the 10-15 minute increase from no reaction to the maximum can be traced to the relatively high thermal mass of the furnace system coupled with gas dispersion resulting from relatively low flow rates in the large diameter reaction tube. Gas evolution curves in the solar furnace system resemble the ideal. It is clear from figure D-5 that the reactions as practiced here are relatively slow, and that the initial stages of TR are more rapid than the initial stages of WO. The reasons for this are currently unknown, but surface reaction kinetics, thermodynamic driving forces, and mass transport to and away from the surface could all play a role. We are reasonably certain that transport within the bulk is not the rate limiting factor however as thermogravimetric analysis of the oxidation of thermally reduced samples with O_2 in air at 1100 °C shows the reaction to be complete within several minutes.

The differences in reaction rate are not a particular concern for the CR5 design as they will eventual come to a balance under steady state operation. This point can be understood by examining figure D-6, wherein the data from figure D-5 is replotted so that rates are shown as a function of "total oxygen deficiency" in the monolith sample. The oxygen deficiency is defined as the integrated amount of O_2 evolved up to that point in time in the case of TR, or for WO the final O_2 deficiency at the end of the TR step minus ½ the amount of H_2 evolved and minus the total amount of O_2 the sample has been exposed to a result of background O_2 up to that point in time (plotted as Reoxidation, O_2 basis). Thus the TR step proceeds from left to right in figure D-6, while WO (the back reaction) proceeds from right to left. A hypothetical unreacted packet of ferrite monolith circling through the CR5 would first be reduced, represented in figure D-6 as movement to the right on the O_2 evolution curve. Then, for a similar time period, it would be oxidized, represented by a drop to the reoxidation curve and a smaller movement back to the left (the rate is small as is the impact on oxygen deficiency). The packet would then again be thermally reduced and driven further along the WO curve to the right. The sequence would repeat until the sample is driven far enough into reduction that the rates of WO and TR converge and the process operates in the area where the TR and reoxidation curves cross one another.

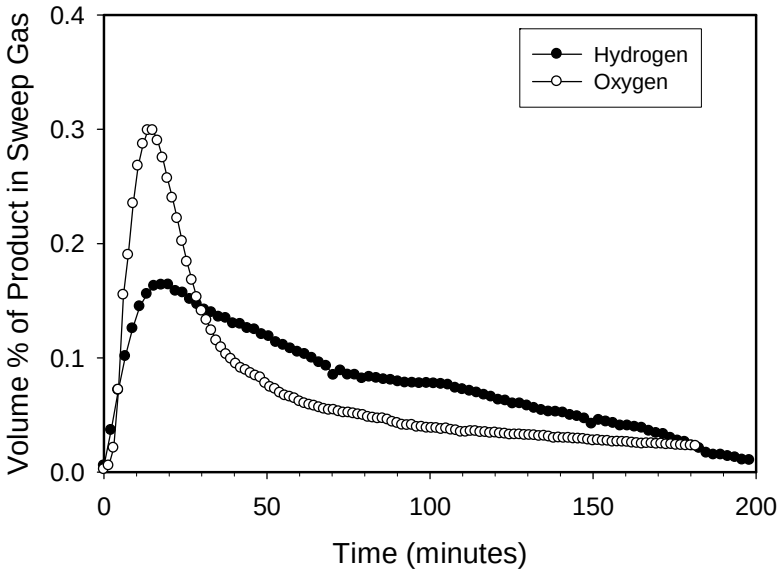

Figure D-5. Oxygen and hydrogen evolution from robocast $Co_{0.67}Fe_{2.33}O_4$/YSZ monolith with dense rods during cycle 36 (refer to Figure D-4).

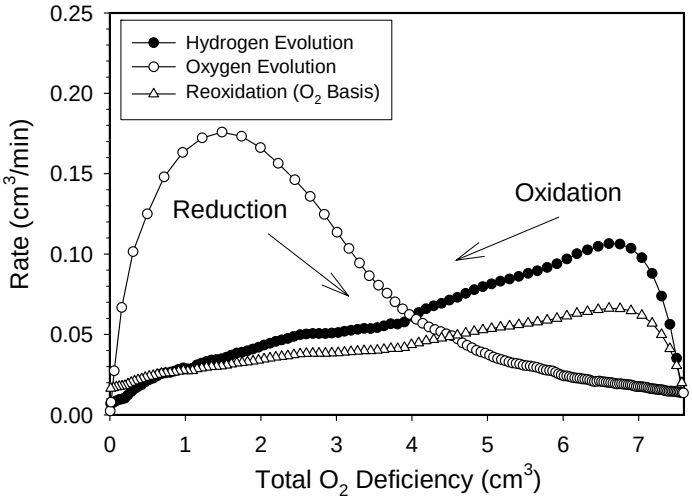

Figure D-6. Rates of O2 evolution, H2 evolution, and equivalent O2 uptake during WO as a function of total oxygen deficiency in the monolith sample. Data adapted from figure D-5.

In truth, the use of figure D-6 for the above illustration is an oversimplification; the reason being that it is not simply the oxygen deficiency of the sample that determines the reaction rate, but the history of the sample as well. It is clear in the data from shorter cycles for example that if TR is interrupted after the evolution of only 4 cm^3 of O_2, then the initial H_2 evolution rate is significantly higher than that shown in figure D-6 for an oxygen deficiency of 4 cm^3. If one assumes a simple shrinking core type model for the progress of both the TR and WO reactions in a rod geometry, it is clear that this should be expected. For this model, TR of a fully oxidized sample would result in an outer annular layer of reduced material.

Subsequent WO would also proceed from the outside, resulting in cylinder of reduced material sandwiched between an inner core and outer eggshell of oxidized material. A similar volume of reduced material could be produced in a second sample as shallow surface layer by performing a shorter TR step. It is clear that the apparent reactivity of the surface layer and the inner ring would be different even though the total oxygen deficiencies of the two samples were identical.

In any case, what is important for CR5 operation is not the maximum rate of each reaction, but rather maximizing the kinetics of the reaction at the point where the two rates converge. This in fact may be a more important factor than how far one can drive a sample into and out of a reduced state, i.e. the maximum materials utilization. In other words it can be better to utilize a smaller percentage of material at a higher rate than a higher percentage at a smaller overall rate. This point may be further understood by reexamining the data in figures D-4 and figure 4 in the main document in the context of figure D-5. It is clear that when the TR time period is reduced, the H_2 yields do not suffer a proportional decrease. Thus a greater number of shorter cycles can result in larger overall yield than a single cycle carried out over the same time period.

Temperature is of course an important consideration for maximizing reaction rates. The limits of our laboratory furnace have effectively prevented us from addressing this issue for the TR step. Cycles 3-8 in figure D-4 address the effect of temperature on the WO reaction. For these cycles, the TR step was performed as in the standard cycle. The WO step for cycle 4-8 however was performed by decreasing the temperature to that shown and then initiating steam flow. For cycle 3, steam flow was initiated at 1400 °C and the sample was allowed to cool to 900 °C. The results clearly show that the highest yields of H_2 were obtained at 1100 and 1200 °C. The poor yield at 1300 °C is evidently the result of unfavorable thermodynamics. The poor yield at 900 and 1000 °C is evidently the result of poor kinetics as the thermodynamics should be most favorable at the lowest temperatures.

The unfavorable thermodynamics for WO at 1300 °C raises the possibility of using steam as an "inert" sweep gas that can easily be separated from O_2 produced during TR. Even if this were not done, it could alleviate concerns regarding crossover of steam from the WO side of the CR5 to the TR side. To evaluate this possibility, several cycles were performed with a porous robocast monolith utilizing the saturated Ar flow in place of the He sweep during the 1400 °C TR step. The resulting H_2 yields during the WO steps were virtually indistinguishable from those with the He sweep in earlier and subsequent cycles. Nonetheless, longer term evaluation of the effect of steam is required due to its tendency to degrade materials and enhance metal volatility D-10

Summary

Two-step oxide-based thermochemical processes offer an exciting alternative to water electrolysis for H_2 production. However, in order for these processes to be truly competitive with electrolysis, energy

management is essential. This fact makes efficient thermal recuperation between the high and low temperature reactions a virtual necessity. The CR5 is a new reactor concept that was designed to accomplish ferrite-based water splitting with thermal recuperation and simplicity of operation as guiding principles. As part of our efforts to develop a CR5 prototype, we have demonstrated that ferrite/zirconia mixtures may be directly fabricated into monolithic structures that are mechanically robust and that maintain productivity over at least tens of cycles with no apparent degradation in performance. Work is ongoing to maximize the utilization of the ferrite and the reaction rates of the monoliths. Our baseline choice of material for the prototype is a mixture of $Co_{0.67}Fe_{2.33}O_4$ and YSZ in a 1:3 weight ratio. Future work will consider Ni-substituted materials ($NiFe_2O_4$) that are indicated as the optimum material by thermodynamics. Many questions remain unanswered regarding the basic processes taking place during both the TR and WO steps. Additionally, the role of "inert" supports such as YSZ in stabilizing ferrites over multiple water splitting cycles is not well understood as both physical (particle isolation) and chemical (Fe dissolution, oxygen transport) mechanisms may contribute.

References:

D-1. Tamaura, Y.; Steinfeld, A.; Kuhn, P.; Ehrensberger, K. "Production of Solar Hydrogen by a Novel, 2-Step, Water-Splitting Thermochemical Cycle" Energy 20 (1995) 325-330.

D-2. Tamaura, Y.; Kojima, M.; Sano, T.; Ueda, Y.; Hasegawa, N.; Tsuji, M. "Thermodynamic Evaluation of Water Splitting by a Cation-Excessive (Ni,Mn) Ferrite" Int. J. Hydrogen Energy 23 (1998) 1185.

D-3. Aoki, H.; Kaneko, H.; Hasegawa, N.; Ishihara, H.; Takahashi, Y.; Suzuki, A.; Tamaura, Y. "Two-step water splitting with Ni-Ferrite system for Solar H_2 Production using Concentrated Solar Radiation," Proceedings of 2004 International Solar Energy Conference, Portland, OR.

D-4. Kodama, T.; Kondoh, Y.; Yamamoto, R.; Andou, H.; Satou, N. "Thermochemical Hydrogen Production by Redox System of ZrO2-Supported Co(II)-Ferrite," Solar Energy 78 (2005) pp. 623-631.

D-5. M. Roeb, C. Sattler, R. Kluser, L. Monnerie, A.G. Konstandopoulos, C. Agrafiotis, V.T. Zaspalis, L. Nalbandian, A. Steele, and P. Stobbe in Proceedings of the 2005 International Solar Energy Conference (ISEC), Orlando, FL, 2005 (ASME, 2006) p. 671.

D-6. J.N. Stuecker, J.E. Miller, R.E. Ferrizz, J.E. Mudd, and J. Cesarano III, Ind. Eng. Chem. Res. 43 (2004) 51.

D-7. J.N. Stuecker, J. Cesarano III, and D.A. Hirschfeld, Journal of Materials Processing Technology 142 (2003) 318; J. Cesarano III and P.D. Calvert U.S. Patent 6,027,326 (2000); J. Cesarano III, R. Segalman, and P. Calvert, Ceramic Industry 148 (1998) 94.

D-8. R.M. Ferrizz, J.N. Stuecker, J. Cesarano III, and J.E. Miller, Ind. Eng. Chem. Res. 44 (2005) 302.

D-9. T. Kodama, Y. Kondoh, A. Kiyama, and K. Shimizu "Hydrogen Production by Solar Thermochemical Water-Splitting/Methane-Reforming Process" in Proceedings of the ASME International Solar Energy Conference (ISEC), Hawaii, 2003, M.D. Thornbloom and S.A. Jones, editors (ASME, 2003) p. 121.

D-10. J.G. McCarty, M. Gusman, D.M. Lowe, D.L. Hildenbrand, and K.N. Lau, Catalysis Today 47 (1999) 5.

APPENDIX E

CR5 MODELING AND SCOPING STUDIES

Appendix E - CR5 Modeling and Scoping Studies

In this appendix, numerical modeling to investigate the concept of a solar-driven reactor for splitting water is presented in detail for the "counter-rotating-ring receiver/reactor/recuperator" (CR5) solar thermochemical heat engine that is presently under development. The details of numerical simulations predicting the thermal/fluid behavior of the innovative solar-driven thermo-chemical reactor are described. These scoping calculations have been used to provide insight into the thermal behavior of the counter-rotating reactor rings and to assess the degree of flow control required for the CR5 concept.

Research regarding the conversion of solar energy into chemical energy has been around for at least 50 years [E-1] with much of the recent research concentrating on a two-step or multi-step water splitting process [E-2 to E-7]. The basic idea of a water splitting process involves the reduction of a metal oxide followed by an oxidation reaction with water in which hydrogen is produced. The efficiency of the reduction reaction increases with temperature, hence focused solar energy from a solar concentrator can increase the amount of hydrogen produced. A challenge for solar thermochemical heat engines is the efficient utilization of the heat captured on the high temperature side of the reactor. Sandia National Laboratories has developed a concept for a unique solar thermochemical heat engine that regenerates the waste heat in two recuperator sections which is named the CR5 - counter-rotating-ring receiver/reactor/recuperator. The purpose of the studies reported here was evaluate the thermal-related performance of various aspects of the CR5 to better understand the overall CR5 cycle efficiency.

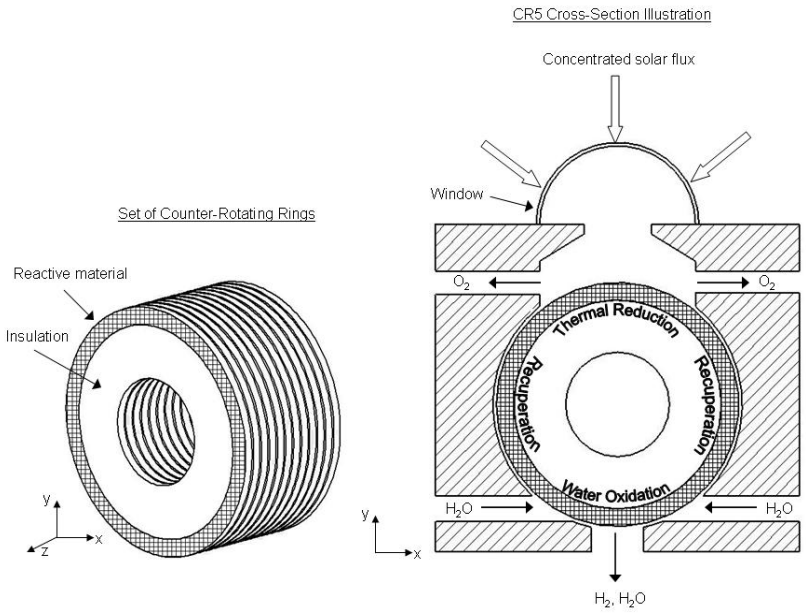

Figure E-1. Schematic of the CR5.

A schematic of the CR5 is shown in figure E-1. A set of counter-rotating rings absorb the solar flux on the hot side of the reactor with radiation and conduction being the predominant heat transfer mechanisms. As each ring rotates out of the hot side, radiative heat transfer with the recuperator sections provides regeneration of thermal energy to the adjacent, colder rings that have just rotated out of the exothermic, hydrogen producing cold side. Each ring is composed of a gear ring (not shown in figure E-1), insulation, and the reactive material. A cross-sectional view of the ring is shown in figure E-2.

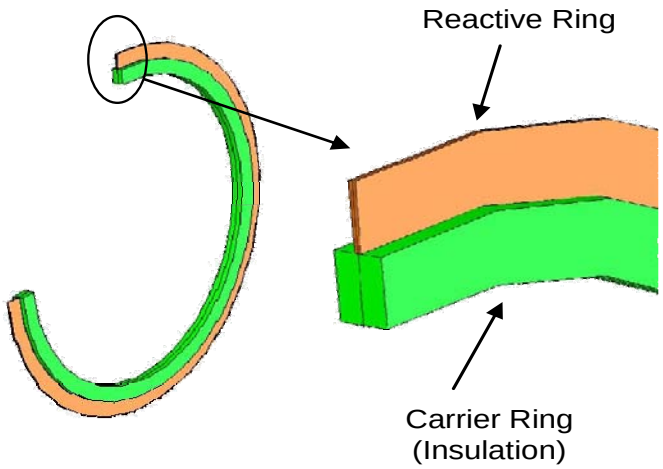

Figure E-2. Cut-away of single ring showing cross-section.

Numerical modeling was used in scoping calculations to evaluate the feasibility of this concept. A numerical investigation of the CR5 concept was conducted with the following objectives:

- Evaluate sensible heat transfer in the recuperator section
- Provide an assessment of the simplified recuperator model being used in the system simulations
- Evaluate flow fields within the CR5 to better understand potential mixing effects
- Provide insight into the design parameters affecting system performance

Two numerical models have been developed to address different aspects of the relevant physics. In the first model, referred to here as the "Radiative Model," the radiative exchange between the counter-rotating rings is computed to evaluate the heat exchanger "effectiveness" of the recuperation sections and to provide thermal boundary conditions for the "Fluid Flow Model." Each of these modeling approaches is discussed in more detail below.

The "Radiative" Numerical Model

A finite element model of the CR5 concept that focused on the recuperator performance was developed to predict the radiative exchange between the counter-rotating rings and to assess the effectiveness of the rotating-ring concept as a counter-flow heat exchanger. In this model, a "typical" pair of counter-rotating rings assumed to be near the center of the reactor is considered. The geometric

definition of this numerical model utilizes planes of symmetry at the axial center of each ring and treats these planes as insulated. A cross-section of the numerical model consisting of two half-rings is shown in figure E-3.

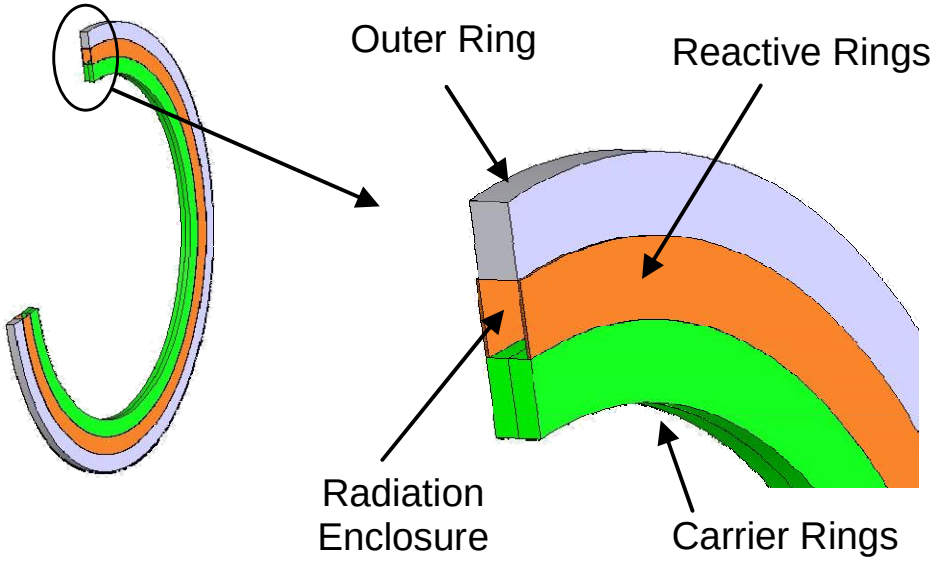

Figure E-3. Cut-away of Radiative Numerical Model showing two half-rings and the radiation enclosure cross-section

The CR5 is divided into four regions circumferentially that correspond to the four sections having different thermal conditions. Figure E-4 shows the four sections of the CR5 which are characterized by:

- the thermal reduction (TR) zone or the "hot zone" where solar energy is absorbed by the rings,
- the two recuperation zones or "insulated zones" where energy is transferred between the two rotating rings, and
- the water oxidation (WO) zone or the "cold zone" where the hydrogen is liberated.

Because this model focuses on the radiative transfer between the counter-rotating rings, fluid flow, convective transfer, and chemical reactions have been neglected. The model simulates the absorption of incident solar energy, heat conduction in the reactive rings and the carrier rings (insulation ring), material advection due to the rotational motion of these rings, radiative exchange between the rings and with sides of the reactor housing, and radiative/convective cooling in the cold region. Neglecting the chemical reactions in the hot and cold zones in this model will affect the local temperatures in these zones.

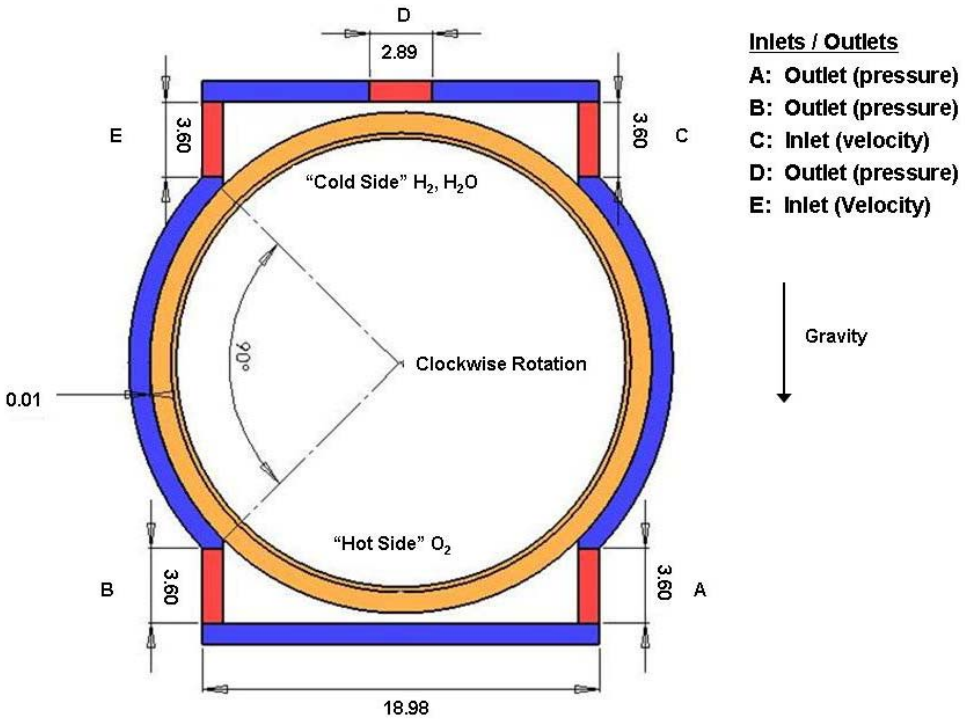

Figure E-4. Simplified schematic of the CR5 and reactive ring geometry

The heat conduction within the rotating reactive and carrier rings can be formulated in two ways:

- a Lagrangian formulation where the mesh is fixed to the rings and moves with them or
- an Eulerian formulation where the finite element mesh is fixed in space and the ring materials move through the mesh.

For this analysis, the heat conduction in the rings is formulated using an Eulerian formulation and is given by

$$\rho u_j C \frac{\partial T}{\partial x_j} - \frac{\partial}{\partial x_i}\left(k_{ij} \frac{\partial T}{\partial x_j} \right) = 0 \ . \qquad \text{(E-1)}$$

The thermophysical properties are assumed constant. The velocity in the advection term is the velocity of the rings relative to the mesh and is specified through the angular velocity of the rings. For these scoping calculations, the nominal rotational speed of the rings ranged from 1/8 to 3/4 rpm. The radiative transfer between the reacting and carrier rings and the housing is computed using the net-radiation method [E-8,E-9].

Assuming that the surfaces participating in thermal radiation are diffuse and gray and assuming that the radiative surfaces are locally isothermal and have uniform net heat flux, the radiative exchange

between the N_{surf} surfaces defining the enclosure is formulated using the net-radiation method and is given by

$$\sum_{j=1}^{N_{surf}} \left[\frac{\delta_{kj}}{\varepsilon_j} - F_{k-j} \left(\frac{1-\varepsilon_j}{\varepsilon_j} \right) \right] \frac{Q_j}{A_j} = \sum_{j=1}^{N_{surf}} \left(\delta_{kj} - F_{k-j} \right) \sigma T_j^4 \ . \qquad \text{(E-2)}$$

The radiation "enclosure" is defined as an annular region bounded by the outer radius of the carrier rings, the faces of the reactive rings, and the inner radius of the outer ring. The cross-section of this annular enclosure is shown in figure E-3. The outer ring represents the insulation boards in the recuperators and artificial surfaces representing the hot and cold zones. In this model, the outer ring is sub-divided into four regions that correspond to the four different "zones" in the CR5. The approximations for boundary conditions in each of these regions are discussed next.

In the two recuperator zones, the surfaces that complete the radiation enclosure are the surfaces of the insulating board. The boundary condition on the outer radius of the insulating board is zero heat flux. The inner radius of the insulating board has a radiative heat flux due to enclosure radiation. In the hot and cold zones, the inner surfaces of the outer ring are used to specify the effective heat source and sink temperatures. For the "hot zone," the incident solar heat flux is approximated by modeling this artificial surface as a uniform temperature surface at 1923K. This is recognized as a simplification because the incident radiation from a concentrator would not be diffuse, but would vary with direction within the cone angle of the concentrator. However, this simplification was used in this scoping study to assess the effectiveness of the recuperator. For the "cold zone," the energy transfer from the reacting rings is approximated by both radiation and convection to a fixed temperature of 298K.

Computation of the view factors for enclosure radiation can be a significant effort. If a Lagrangian formulation for the heat conduction had been employed, then the view factors between element surfaces would have had to have been recomputed at every time step due to the mesh movement. Because the finite element model used here is based on an Eulerian formulation, the mesh is fixed and the view factors within the enclosure are calculated only once; a significant savings over a Lagrangian approach.

In this initial analysis, the carrier ring is assumed to be made of insulating board, the reactive ring is assumed to be zirconia/iron oxide mix, the insulating sides are assumed to be fibrous insulating board, and the "cold" and "hot" surfaces are imaginary surfaces to approximate the incident heat flux and water oxidation zones. The material properties for this model are given in Table E-1.

Table E-1 Thermophysical properties using in the CR5 thermal models

	k (W/mK)	(kg/m^3)	C (J/kg K)	emissivity
Reactive ring	1.1	3000	690	0.8
Carrier ring	0.15	2400	1047	0.6
"hot or cold zone"	-	-	-	1.0
"insulating sides"	0.15	2400	1047	0.6

The temperature distribution within the reactor was computed for these material properties and boundary conditions. The computed temperatures were used to estimate the recuperator effectiveness. The effectiveness values computed were subsequently used in the thermochemical system model described in Appendix B. For these calculations, the recuperator was treated as a counter-flow heat exchanger with a solid-phase working "fluid." The effectiveness was formulated in terms of the temperatures of the reactive ring entering and exiting the recuperator zones [E-10]. Typical recuperator effectiveness values ranged from 0.77 at 3/4 rpm to 0.86 at 1/2 rpm.

Figure E-5 shows the temperature distribution along the outer radius of the reactive ring for a rotational speed of 3/4 rpm. For the radiation simulations, the angle corresponding to 0 degrees is defined to be the 6 o'clock orientation for ring shown in figure E-4 and the 12 o'clock position corresponds to 180 degrees. It can be seen that the average ring temperature on the "hot" side is approximately 1600°C and the profile in the recuperator section (45° - 135°, 225° - 315°) can be approximated as linear. The temperature of the "cold" side (135° - 225°) is approximately constant at 500°C.

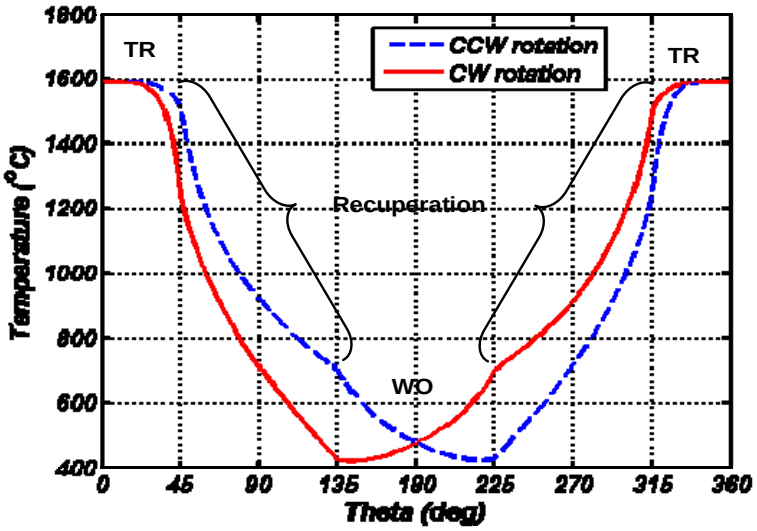

Figure E-5. Average temperature of a reactive ring pair as a function of angle

Figure E-6 shows a typical temperature distribution in the counter-clockwise rotating ring. The effect of the ring motion is evident in the counter-clockwise shift of the temperature distribution. These computed temperatures were subsequently used as boundary conditions with the more detailed "Fluid Flow" model to simulate the fluid flow field and evaluate potential mixing characteristics of the CR5.

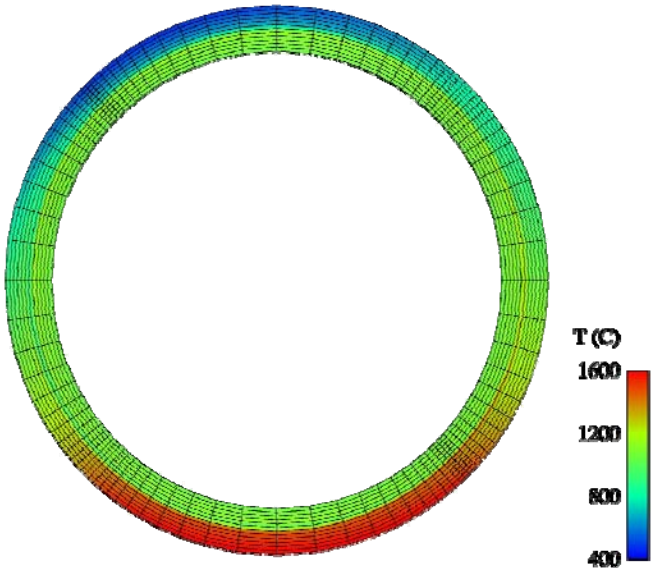

Figure E-6. Predicted CR5 carrier and reactive ring temperatures, in Celsius, at a rotational speed of 3/4 rpm

The "Fluid Flow" Numerical Model

Based on the temperature distribution obtained in the radiative model, various simulations were performed utilizing the Fluent CFD solver and specially written subroutines referred to as user-defined

functions (UDFs). It should be noted that the size of the CR5 changed during its development, but the basic geometry consists of counter rotating rings enclosed in a housing. The models presented here utilize symmetry and thus represent half of a two counter-rotating rings and housing. The grid of the reactor ring used in the fluid flow analysis was similar to the grid illustrated in figure E-6. The initial grid for the fluid portion of the model was adapted based on temperature and velocity gradients.

Various simulations were performed to determine the degree to which buoyant natural convection flows would cause undesired crossover (hydrogen in the cold side moving to the hot side where the oxidation reaction occurs). To investigate a worst case crossover scenario, the model of the CR5 was oriented with the hot side vertically below the cold side such that the body force due to gravity was maximized (note the gravity vector direction in figure E-4). The operating, pressure defined at the center of the rings, was 20.265 kPa. The outlet ports pressure was set to 0 gage. The portions of the ring on the "cold" side (90° section sandwiched between the recuperators labeled "water oxidation" in figure E-1) were specified to be 1000K and those of the "hot" side (90° section sandwiched between the recuperators labeled "thermal reduction" in figure E-1 and exposed to the concentrated solar flux) were 1800K. The low temperature value was increased over the results presented in figure E-5, because it was felt that the cusp on the "cold" side was a result of boundary conditions used in the radiative model that would not be prevalent in the full CR5 reactor design.

A UDF was written that provided a linear temperature distribution of the ring in the recuperator sections between the hot and cold side temperatures. Only the reactive material portion of the rings had a prescribed temperature distribution. Radiation heat transfer was modeled using the discrete ordinates (DO) model with discretization and pixilation values set to 3. Considering the fluids to be non-participating, the DO model can be written in terms of the radiative intensity that is a function of position, $\vec{r}$, and direction $\vec{s}$.

$$\nabla \cdot \left(I(\vec{r},\vec{s})\vec{s} \right) = 0 \tag{E-3}$$

and the heat transfer is calculated at the wall (for all positive values of $\vec{s} \cdot \vec{n}$, where $\vec{n}$ is the element normal) by:

$$q_{in} = \int I \vec{s} \cdot \vec{n} \, d\omega \tag{E-4}$$

where the solid angle is discretized into a total of 72 sub-angles and any overhanging elements were also discretized by 72 sub-angles. The heat transfer out of a wall is given by

$$q_{out} = (1 - \varepsilon_w) q_{in} + \varepsilon_w \sigma T_w^4 \tag{E-5}$$

Laminar natural convection heat transfer for each species was modeled using the incompressible, ideal gas assumption for the buoyancy term in the Navier-Stokes equation:

$$\frac{\partial(\rho\vec{V})}{\partial t}+\vec{V}\cdot\nabla(\rho\vec{V})=-\nabla P+\mu\nabla^2\vec{V}+(\rho-\rho_o)\vec{g} \qquad \text{(E-6)}$$

where ρ_o is the (constant) operating density (0.03134 kg/m^3) and the density, ρ, in the body force term is determined from the ideal gas equation of state using the local temperature and pressure; otherwise the density is constant.

A simple model of just two rings counter-rotating at 1 rpm was considered to estimate the degree to which the bulk of the fluid in the gap between the rings moved with the rotation, and it was determined that it was insignificant; therefore, for the cases presented below, the rotation of the rings was set to zero.

UDFs were written to generate oxygen and hydrogen at a rate of 0.017 g/s and 0.002 g/s, respectively, with zero bulk momentum in the gap (6.4 mm) between the reactor rings on the "hot" and "cold" sides, respectively. The generation of hydrogen and oxygen represent the chemical production of each gas. The temperature of the generated oxygen and hydrogen was 1800K and 1000K, respectively, such that no enthalpy deficit was introduced. Steam, at a temperature of 1000K, was supplied at the two inlets (labeled C and E in figure E-4) at a rate of 0.033 g/s. Figures E-8 to E-10 show steady-state contours of mole fraction of specified species at the mid-plane (in the middle of the modeled geometry).

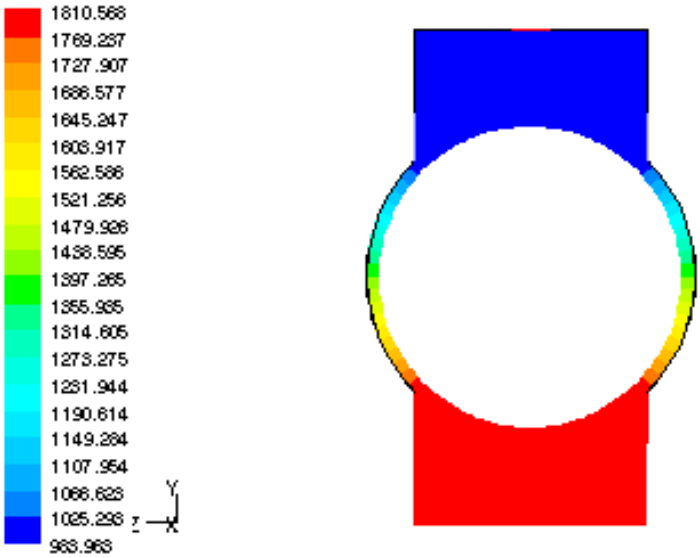

Figure E-7. Mid-plane temperature distribution

Figure E-7 shows the predicted temperature distribution at the mid-plane. The specified linear temperature distribution in the recuperator is evident. The temperature of the walls above the hot side and below the cold side was specified to be 1000K and 1800K, respectively. Gravity is in the negative y

direction with regards to the coordinate shown in figure E-7. In this orientation, buoyancy forces are maximized with regards to the unwanted cross-over of hydrogen and oxygen.

The mole fraction of oxygen is depicted in figure E-8 where it can be seen that the generated oxygen is confined to the side at which is generated with no cross-over. A very small amount exists in the lower sections of the recuperator.

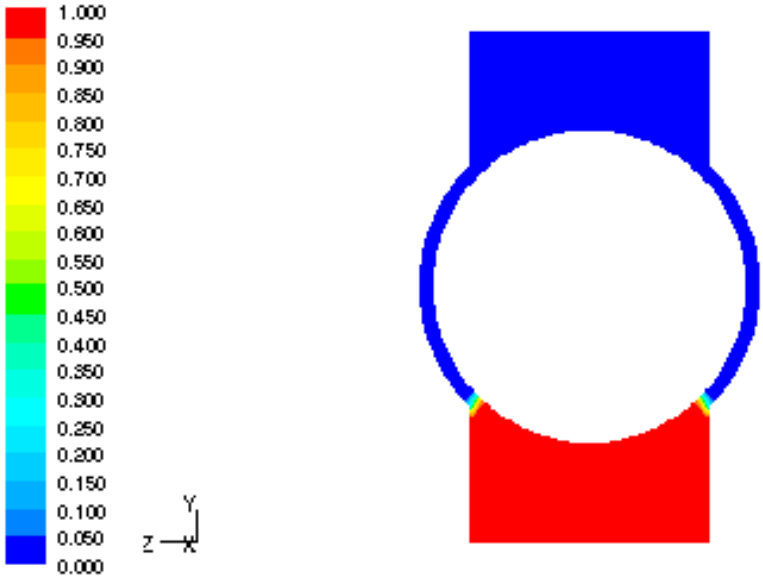

Figure E-8. Oxygen mole fraction prediction on the mid-plane

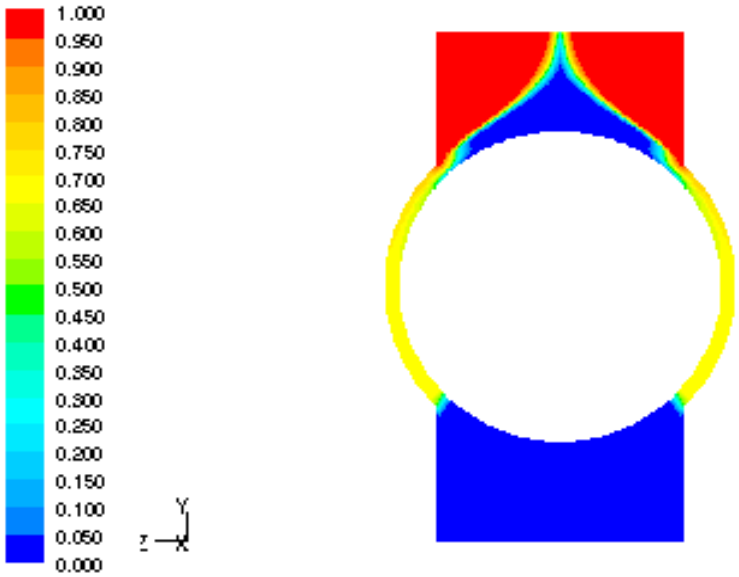

Figure E-9 Mid-plane steam sweep gas mole faction prediction

Figures E-9 and E-10 depict the mole fraction of the steam sweep gas and the hydrogen, respectively. For this model, the steam effectively engulfs the hydrogen reducing cross-over. The mole fraction of the steam in the recuperator sections is 70% or greater, the remainder being hydrogen.

Conclusions

A numerical investigation has been performed to understand various physical processes that contribute to the thermal performance of the CR5 solar thermochemical heat engine. It has been shown that regenerating the thermal energy in the recuperator section is feasible, with effectiveness values of 0.77 and 0.86 for rotational speeds of ¾ and ½ rpm, respectively.

The temperature profile in the reactant ring was used to evaluate the extent of cross-over of hydrogen and oxygen that were “produced” on the “cold” and “hot” side of the reactor, respectively, simulating the production of gas in the reactant. Using steam as a sweep gas at a flow rate of 0.33 kg/s, and no other flow control, the crossover of hydrogen was typically less than 20%. In order to reduce hydrogen crossover further, pressure control at outlet D (see figure E-4) should be considered.

Future work should include modeling the counter-rotation of the reactive rings to evaluate the extent of cross-over in a coupled heat, mass, and momentum simulation so as to better define the extent of flow control required. It is also envisioned to include limited chemical kinetics of the respective redox chemical reactions.

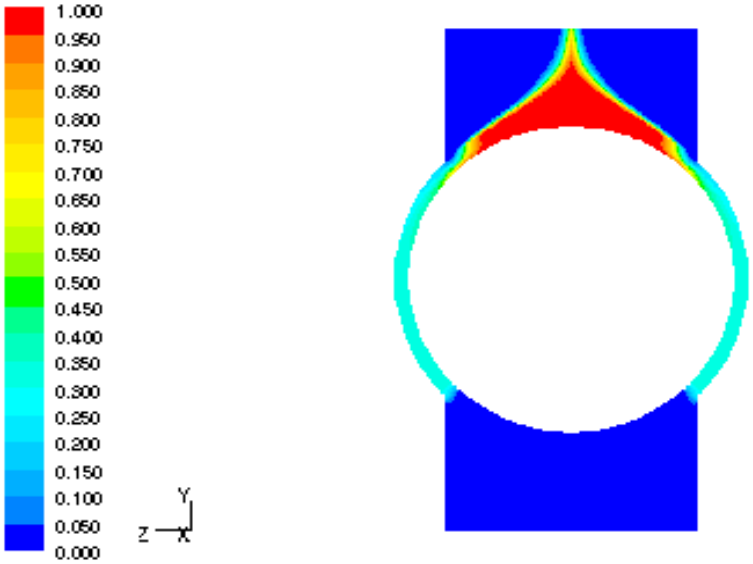

Figure E-10. Hydrogen mole fraction prediction on the mid-plane

References

E-1. Steinfeld, A., Sanders, S., and R. Palumbo, "Design Aspects of Solar Thermochemical Engineering –A Case Study: Two-Step Water-Splitting Cycle Using the Fe3O4/FeO Redox System," *Solar Energy* Vol. 65, No. 1, pp43-53, 1999.

E-2. Richard B. Diver, James E. Miller, Mark D. Allendorf, Nathan P. Siegel, and Roy E. Hogan, "Solar Thermochemical Water-Splitting Ferrite-Cycle Heat Engines," Proceedings of the ASME Solar Energy Conference 2006, Denver, CO.

E-3. Nakamura, T., 1977, "Hydrogen Production from Water Utilizing Solar Heat at High Temperatures," *Solar Energy*, Vol. 19 pp. 467-475.

E-4. Lundberg, M., 1993, "Model Calculations on Some Feasible Two-Step Water Splitting Processes," *Int. J. Hydrogen Energy*, Vol. 18, No. 5 pp. 369-376

E-5. Ishihara, H., Kaneko, H., Yokoyama, T., Fuse, A., Tamaura, Y., 2005, "Hydrogen Production Through Two-Step Water Splitting Using YSZ (Ni, Fe) System for Solar Hydrogen Production," Proceedings of ISEC 2005 International Solar Energy Conference, Orlando, FL.

E-6. Kaneko, H., Kodama, T., Gokon, N., Tamaura, Y., Lovegrove, K., and A. Luzzi, "Decomposition of Zn-ferrite for O2 generation by concentrated solar energy," *Solar Energy* Vol 76, pp. 317-322, 2004.

E-7. Roeb, M., Sattler, C., Kluser, R., Monnerie, L., Konstandopoulos, A.G., Agrafiotis, C., Zaspalis, V.T., Nalbandian, L., Steele, A., Stobbe, 2005, "Solar Hydrogen Production by a Two-Step Cycle Based on Mixed Iron Oxides," ASME Proceedings ISEC 2005 International Solar Energy Conference, Orlando, FL.

E-8. Gartling, D.K., Hogan, R. E. and Glass, M.G., "COYOTE – A Finite Element Computer Program for Nonlinear Heat Conduction Problems, Part I – Theory Manual," SAND94-1173, Sandia National Laboratories, Albuquerque, NM (1994).

E-9. Gartling, D.K., Hogan, R. E. and Glass, M.G., "COYOTE – A Finite Element Computer Program for Nonlinear Heat Conduction Problems, Part II – User's Manual," SAND94-1179, Sandia National Laboratories, Albuquerque, NM (1994).

E-10. Holman, J.P., *Heat Transfer*, 9th edition, McGraw-Hill, New York, NY, (2002).

Nomenclature

A	Area of radiating surface [m^2]
C	Specific heat [J/kg K]
CR5	counter-rotating-ring receiver/reactor/recuperator solar thermochemical heat engine
Fij	Radiation view factor
I	Radiative intensity [W/m^2]
k_{ij}	Thermal conductivity tensor[W/mK]
q	Heat transfer rate [W]
Q	Energy of radiating surface [W]
t	Time [s]
T	Temperature [K]
u	Velocity [m/s]
x	Spatial coordinates [m]

δ_{kj} Kroneker delta

ε Emissivity or emittance

Density [kg/m^3]

σ Stefan-Boltzmann constant

ω Solid angle

APPENDIX F

CR5 PROTOTYPE DESIGN

Appendix F - CR5 Prototype Design

Figure F-1 shows a schematic drawing of the CR5 prototype design. Our overall objective is to demonstrate the practicality of the CR5 concept and to determine how test results from small-scale testing can be extrapolated to real devices. Our approach is to develop a functional prototype that demonstrates the key feature of the CR5 concept. The design is conservative compared to what might eventually be developed. The ring diameter in the prototype is smaller, the ring is thicker, and the mass loading of ferrite is less than we foresee in a high-performance device. The cobalt ferrite reactant in the first CR5 prototype was selected because in our experience it is very forgiving relative to how it is processed. It is not the best performing reactant material we have tested. We anticipate a successful demonstration might produce as much as 100 standard liters per hour of hydrogen from water and be capable of absorbing up to 9 kW of concentrated solar flux.

The prototype reactant rings have an outside diameter of 0.302 m (11.875 inch). . The reactant fins have a height of 2.44 cm (0.96 inch) and a width of 1.27 cm (1/2 inch). Fourteen (14) rings are used. A photograph of Robocast reactant ring segments showing the attachment to the alumina carrier ring is shown in figure F-2. The design of these monolithic reactant fin structures is based on engineering judgment of the design tradeoffs and by the capabilities of the Robocasting technique. Design considerations include penetration of solar flux into the reactant structure, gas permeability to and from the reactant structure, flow resistance through the recuperator sections, and thermal shock resistance. Twelve (12) Robocast reactant ring segments are attached to the perimeter of each 0.254-m (10-inch) diameter, 1.27–cm (1/2-inch) thick, alumina Zircar Buster 35 refractory ceramic fiber board “carrier ring”. A tab on the reactant fin segments is inserted into slots machined into the edge of the carrier rings and pinned in place. Zirconia-based Ceramabond 835 cement secures the reactant fin segments and alumina pins to the carrier rings. The total weight of the Robocast reactant in the prototype is approximately 9.2 kg, with approximately 8 kg available for participating in redox reactions. (The remaining 1.2. kg is in the base and attachment tab.) With 25 wt. % ferrite/YSZ in the prototype reactant fins, there is about 2 kg of available ferrite.

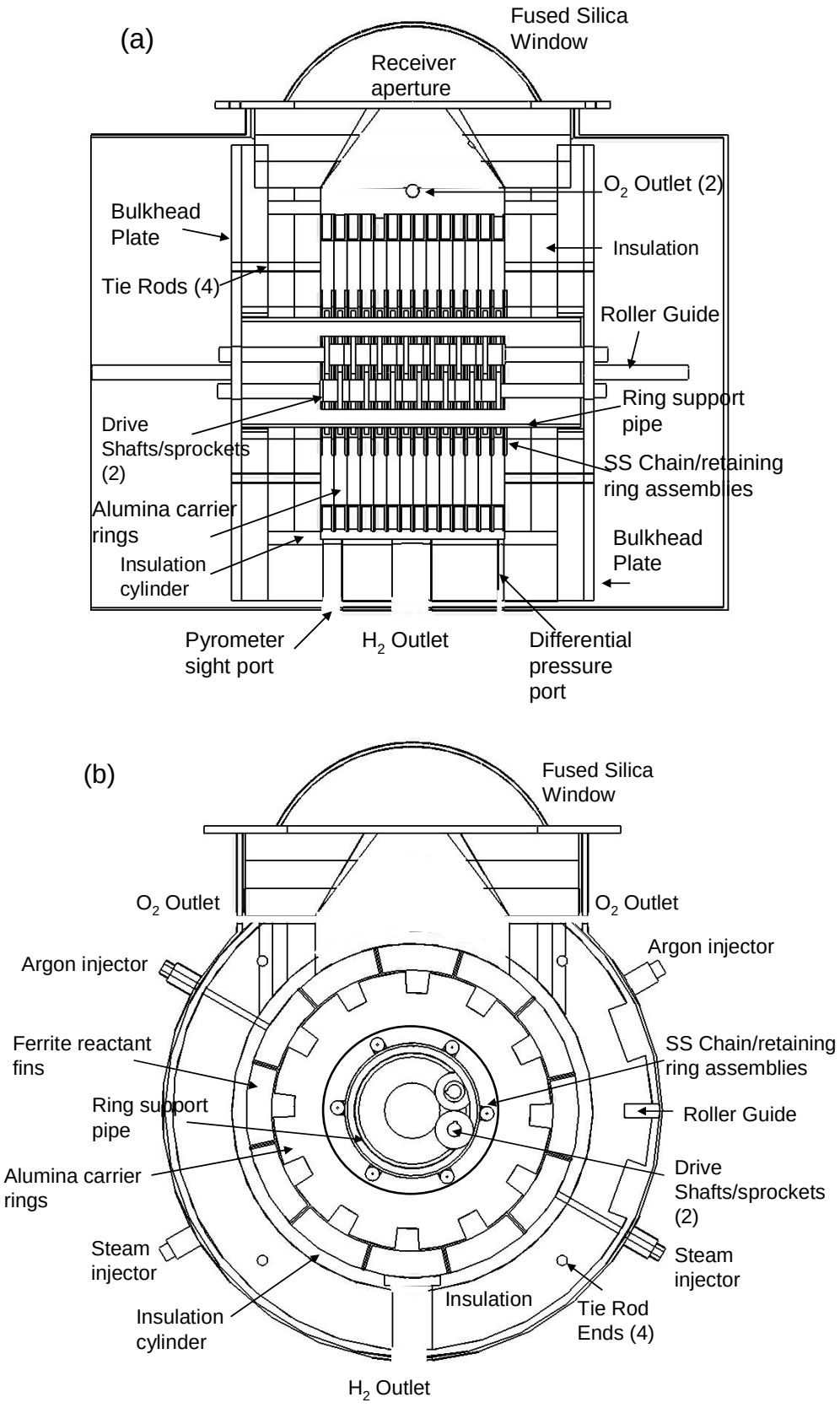

Figure F-1. Schematic (a) side view and (b) end view of the CR5 prototype design.

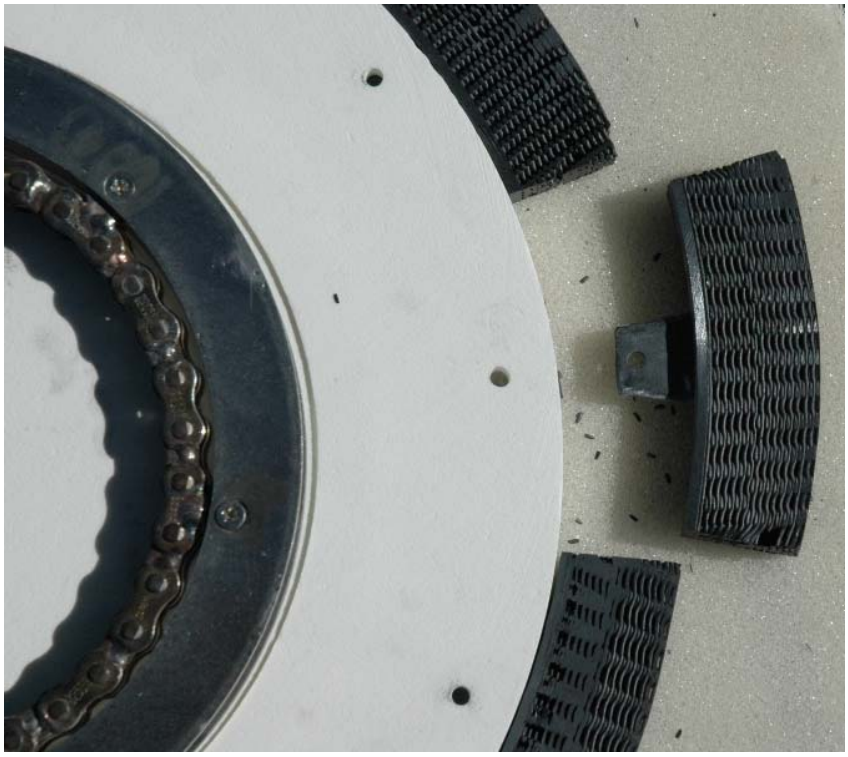

Figure F-2. Photograph of a reactant ring showing the attachment of the reactant fins to carrier ring.

Rotation is driven by two sets of sprockets. For the internal gearing we are using standard ANSI No. 35 stainless-steel chain and sprockets. The individual chain links are welded together to create rigid ring gears which are supported by and ride over a 4.15-in. O.D.-pipe. A slot in the bottom of the pipe allows the sprockets to engage the inside of the ring gears. Six 1.27-cm (1/2-inch) diameter rods segments welded to the outside of each chain ring provide attachment points for two 1.5-mm (0.058-inch) thick sheet metal "retaining rings" that capture the ceramic reactant ring assemblies. All internal gearings and retaining ring hardware are constructed of 300 series stainless steel. A direct current (DC) gear motor drives one of the 1.27-cm (1/2-inch) diameter sprocket shafts. The other shaft is counter driven by directly coupled pinion gears on the two drive shafts. A variable voltage DC power supply is used to control ring speed. The two drive shafts are supported by Rulon bushings inserted into two aluminum bulkhead plates on each end of the reactor. An insulation housing assembly constructed from a 0.305-m (12-inch) I.D. x 0.330-m (13-inch) O.D. Zircar Buster 25 ceramic cylinder and insulating boards are independently attached to the inside of the bulkhead plates. The bulkhead plates also support the drive bearings and ring support pipe. The assembly is tied together with 4 stainless steel tie rods. Rollers attached to the bottom edge of the bulkhead plates facilitate inserting and removing the ring/insulation assembly into the 0.457-m (18-inch) O.D. x 4.8-mm (3/16-inch) thick wall stainless-steel vacuum vessel. A roller guide bar welled to the bottom of the vacuum vessel slides through slots in the bottom of the

bulkhead plates to accurately position the assembly. The vacuum vessel, manufactured by Laco Technologies, has a 0.324-m (12.75-inch) O.D. x 4.7-mm (3/16-inch) thick wall cylinder welded to one side. A 6-mm thick (1/4-inch) stainless steel aperture plate with a 0.232-m (9.125-inch) diameter hole provides an opening for sunlight to be introduced through a 0.248-m (9.75-inch) diameter fused-silica dome window into the TR reactor section. Teflon tape on the ground edge at the base of the dome seals it to the polished stainless steel aperture plate. Standard Viton L-gaskets seal the two ports to the vacuum vessel. A photographs of the prototype CR5 is shown if figure F-3.

Injection ports introduce steam within the recuperator directly over the reactant rings near the exit of the water oxidation (WO) reactor section (120 degrees before top dead center). Top dead center (TDC) corresponds to the center of the solar heated thermal reduction (TR) reactor. Ports near the exit of the TR reactor section (60 degrees after TDC) are capable of injecting argon or steam to promote the TR reaction and block cross flow between the two reactor sections. The 14 injection points in each set of injectors (28 total) are directly over the rings as they exit the respective reactor sections to facilitate counter-current sweeping of the reactant fins. This is intended to promote "polishing off" the reactions as the fins leave the reactors. A hydrogen/steam collection manifold machined into the 0.305-m (12-inch) I.D. ceramic cylinder collects and channels product hydrogen to a 2.54 cm (1-inch) exhaust port in the center of the WO reactor section Two 1.27-cm (1/2-inch) diameter ports in the walls of the cavity receiver (TR reactor) collect product oxygen.

Calculations and numerical simulations were used to address key thermal and fluid dynamic aspects of the CR5. Of concern are (1) cross-flow through the recuperator between the WO and TR reactors, (2) overheating of the internal gearing, (3) flux distribution in the TR reactor, and (4) injector manifold design. We used the FLUENT computational fluid dynamics (CFD) code to simulate the flow field within the device. Injector manifold design involves ensuring evenly distributed flow between injectors and is standard engineering practice. For the injectors 6 mm (1/4-inch) Haynes 230 tubing was used. Injector nozzles were created by plugging and welding the ends of the tubes closed and then drilling small holes into the ends. For the steam (WO) injector nozzles the nozzle diameter is 1.2 mm (0.047 inch). The argon nozzle diameters are 0.8 mm (0.032 inch). Our analyses indicate the internal gearing should operate at less than 500^{o}C, but that cross flow through the recuperator is a potential issue. To address the cross flow issue, we will actively control the pressure in the TR reactor to maintain as low a pressure differential between the two reactors as possible. To accomplish this we have selected a MKS model 651 pressure controller with a Validyne model DP103 differential pressure transmitter. With this system we expect to be able to maintain a pressure differential between reactors approaching 1 Pascal. To help restrict cross flow, we will also attempt to maintain gaps between reactant fins of less than 1 mm (0.040 inch) and between the tips of the reactant fins and ceramic cylinder of less than 3 mm (1/8 inch) at

operating temperatures. In addition, the introduction of sweep gas within the recuperator sections should help establish a pressure gradient barrier to cross flow. A small amount of inert gas or steam will also be injected into the interior of the gear drives to reduce the possibility of hydrogen or oxygen accumulating inside the device. A schematic of the overall experimental system design is shown in figure F-4.

Figure F-3. Photograph of the CR5 test assembly. On the top part of the skid the CR5 vacuum vessel, injector s, and aperature insulation assembley can be seen. On the lower half are the tube in tube condensers, water traps, control valves, vacuum pumps, and steam generator.

Two Alcatel diaphragm vacuum pumps, Model AMD 1, one each on the hydrogen and oxygen exit are used. The valve upstream of the hydrogen pump will sets system pressure. Design system pressures range from 0.05 to 0.5 atm. The solar furnace attenuator and ring speed will be used to control TR reactor temperature. We anticipate using steam injection temperature and flow to establish WO temperature. If necessary to further reduce WO temperature, a cooling coil will be inserted adjacent to the center of the WO section. A sight glass and port near the center of the WO reactor (180^{o} after TDC) allows the WO temperature to be measured with a pyrometer. As with the small-scale solar testing, a pyrometer will measure TR temperature and a flash boiler fed with a metering pump will be used to generate steam. Because of solar contamination issues with the stand Mikron pyrometer, a special pyrometer limited to sensing in radiation is a water band near 1.4 micron was purchased for TR reactor temperature measurement.

To support this test the NSTTF solar furnace was recently upgraded with new heliostat and concentrator mirrors. After evaluating a number of aim strategies for the concentrator, a single aim-point

alignment was selected. The heliostat mirrors are aligned flat. Figure F-5 is a CIRCE2 prediction of the flux distribution along the top of TR cylindrical section assuming 16 kW delivered to the CR5. CIRCE2 is an optical analysis code for point-focus solar concentrators. [11] Of the 16 kW, 77.5 percent is predicted to directly incident the cylindrical reactant fins. The remainder will fall on the ceramic sidewalls inside the cavity. As we adjust power with the solar furnace attenuator, flux intensities should be proportionally less. The design objective was to minimize aperture diameter and to distribute as evenly as possible the energy along the cylindrical absorber. Based on preliminary estimates of the optical characteristics of the new mirrors, a 9 cm diameter aperture will be used on the receiver. Beam characterization confirmed the predicted performance.

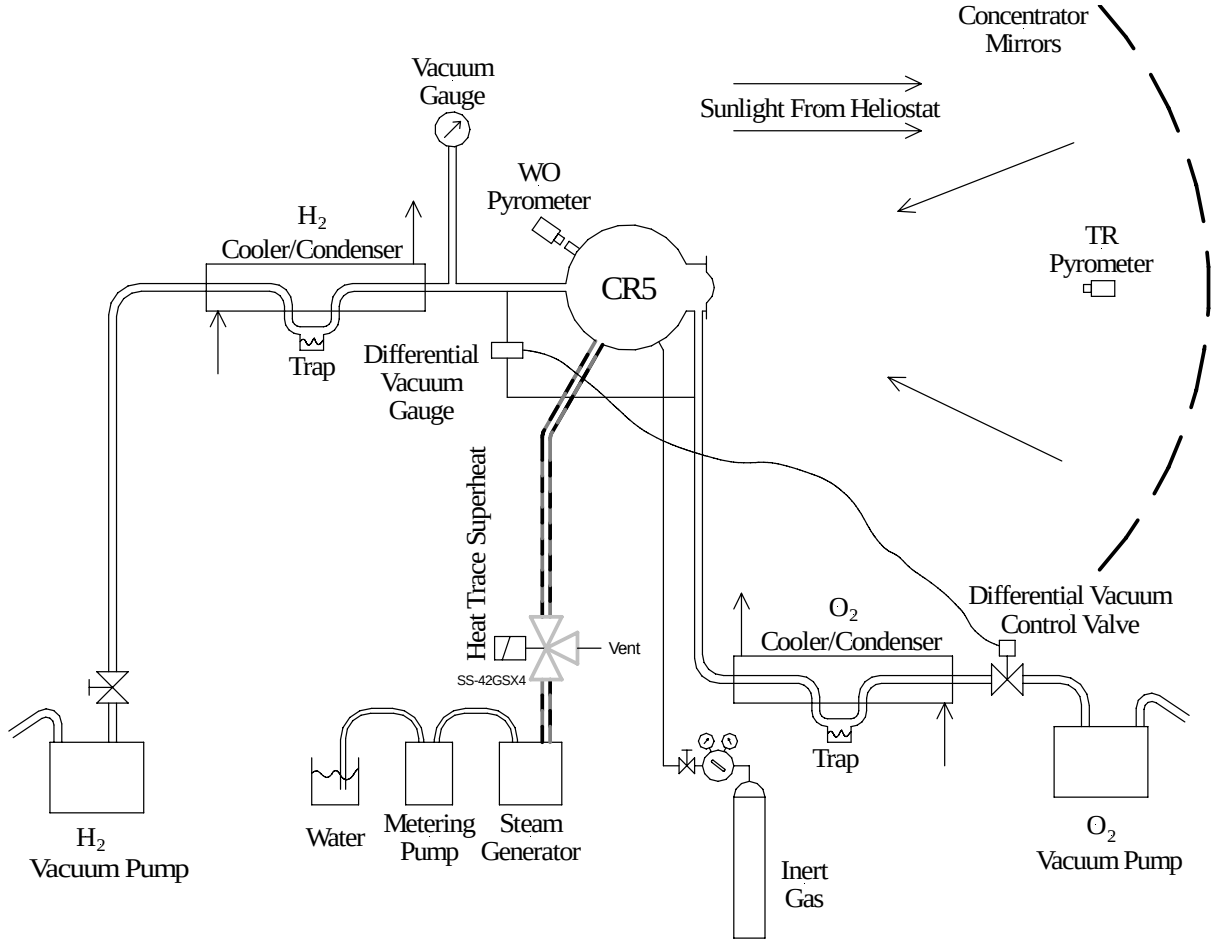

Figure F-4. System schematic for CR5 prototype testing.

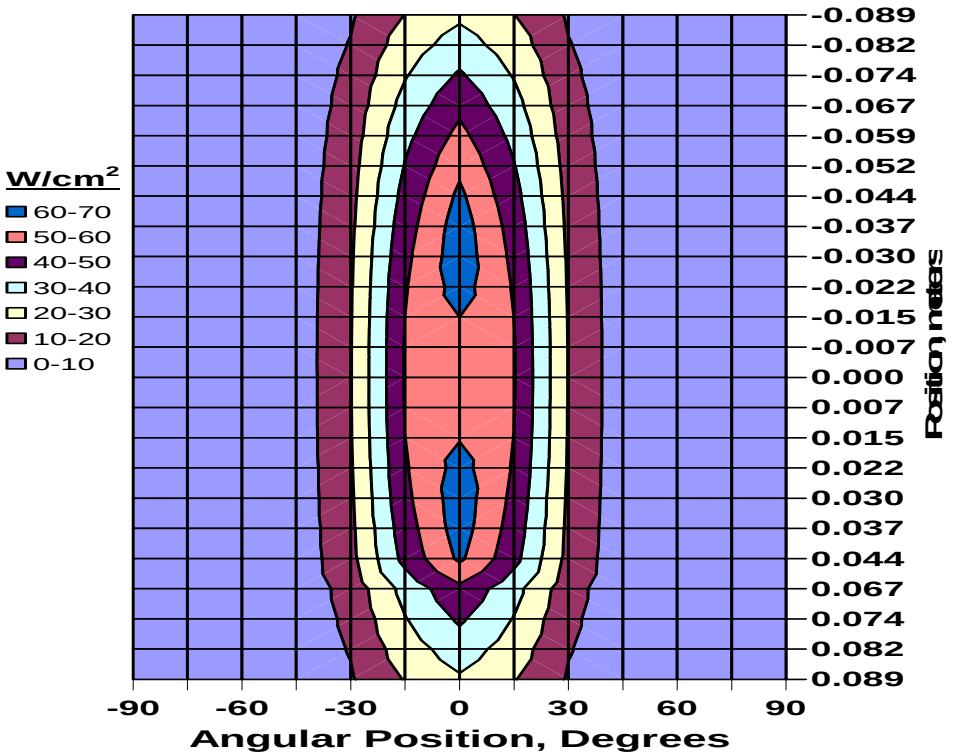

Figure F-5. Predicted flux distribution on the surface of the cylindrical reactant fin absorber in the TR reactor with 16 kW from the furnace. This map depicts flux on an "unrolled" cylinder. Zero degrees correspond to top dead center.

References

F-1 Romero, V.J, 1994, "CIRCE2/DEKGEN2: A Software Package for Facilitatied Optical Analysis of 3-D Distributed Solar Energy Concentrators," Sandia National Laboratories, SAND91-2238, Albuquerque, NM.

APPENDIX G

PREDICTED CR5 PROTOTYPE PERFORMANCE

Appendix G – Predicted CR5 Prototype Performance

Predicted performance maps for the prototype CR5 are presented in figures G-1 and G-2. In these performance maps hydrogen production rate, net solar input into the reactor, and thermal efficiency are presented as functions of reaction extent and ring speed. Reaction extent is defined as the number of moles of hydrogen generated per mole of ferrite ($Fe_{2.33}Co_{0.67}O_4$ in this case), per round trip of ferrite. A reaction extent of 0.1, for example, corresponds to 9.56 standard cm^3/gm ferrite. Hydrogen generation rate, figure G-1, is directly proportional to ferrite mass flow rate (speed) and reaction extent. Net solar input and efficiency were calculated using the CR5 thermal performance model presented in Appendix B. For these calculations a WO temperature and a TR temperature of 1300K and 1900K, respectively, were assumed. The model determines the amount of preheating in the recuperator assuming radiation heat transfer between counter-rotating fins with an emissivity of 0.90. For these calculations, it is conservatively assumed that recuperation only occurs in the recuperator sections. Thermodynamic calculations indicate an equilibrium oxygen pressure of over 0.8 atm. at 1900K, significantly higher than the 0.2 atm. operational pressure assumed. (See figure 2 in the main report.) The amount of solar input required is simply the heat of reaction for the calculated hydrogen generation rate plus the additional power needed for sensibly heating the reactant exiting the recuperator to the TR reactor temperature. As described in Appendix B, thermal efficiency is the higher heating value (HHV) of the hydrogen divided by the sum of the solar input and the equivalent thermal energy needed to drive the pumps. Isothermal pump efficiencies of 40% and a 40% thermal-to-mechanical conversion efficiency for driving the pumps are assumed. The power needed for driving the rings is assumed to be negligible and parasitic power for steam generation and preheat is neglected in these calculations. A reactor pressure of 0.2 atmospheres (atm.) and outlet pressures of 1 atm. and 15 atm., for the oxygen and hydrogen, respectively, were also assumed. These curves show that both power (hydrogen production rate) and efficiency improve with increased reaction extents, but that efficiency is highest at low speeds while power increases with speed. Efficiency is higher at low speeds because recuperator effectiveness increases with more time available for transferring heat between fins.

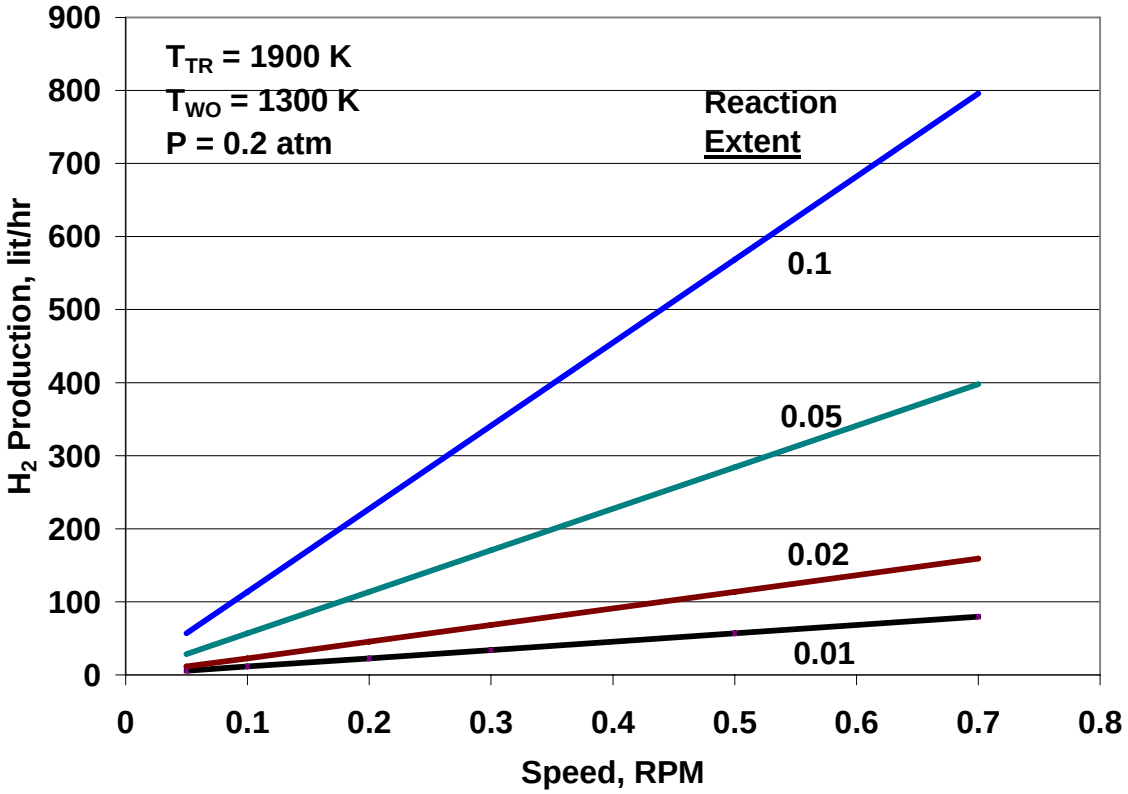

Figure G-1. Predicted hydrogen production as functions of speed and reaction extent.

Because of kinetics the expected reaction extents should be higher at lower ring speeds. The CR5 prototype performance is, therefore, not likely to follow the lines of constant reaction extent in figures G-1 and G-2. However, measured hydrogen production rates and how it changes as a function of speed could be useful in providing information needed to measure kinetics. Performance measurements as functions of the other operational variables such as pressure, TR and WO temperatures, and steam flow rates could also be helpful for establishing design and system optimization information.

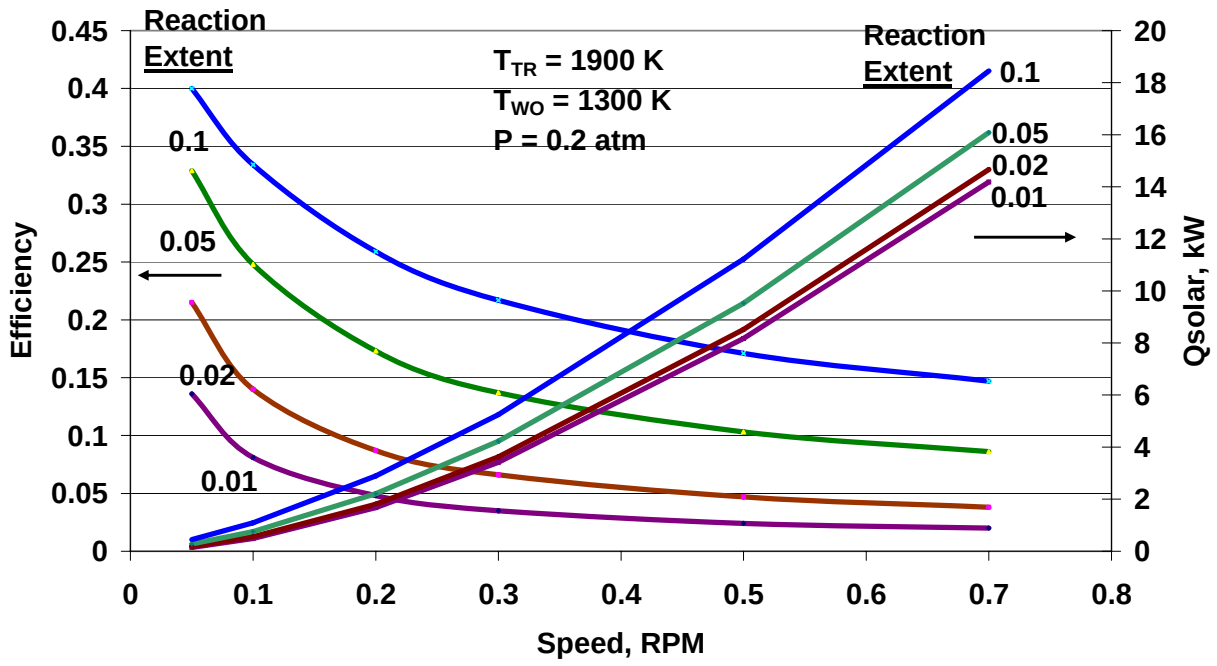

Figure G-2. Predicted HHV efficiency and solar power requirements as functions of speed and reaction extent.

DISTRIBUTION:

1 U.S. Department of Energy
R. Farmer
Hydrogen and Fuel Cell Program
1000 Independence Avenue, SW
Washington, DC 20585

1 Robocasting Enterprises
J.N. Stuecker
4501 Bogan #B4
Albuquerque, NM 87109

3 General Atomics
L.C. Brown
G. Besenbruch
B. Wong
P.O. Box 85608
San Diego, CA 92186

1 Los Alamos Renewable Energy
Reed Jensen
19 Industrial Park Rd
Pojoaque, NM 87506

1 Dave Patterson
1240 Gilbert Ave
Downs Grove, IL 60515

1 Edward A. Fletcher
3909 Beard Ave. S.
Minneapolis, MN 55410

1 R.F.D. Perret
3004 Hawksdale Drive
Las Vegas, NV 89134

1 TIAX LLC
K.W. Roth
15 Acorn Park
Cambridge, MA 02140

1 Niigata University.
Dr. Tatsuya Kodama
Department of Chemistry & Chemical Engineering
8050 Ikarashi 2-nocho, Niigata 950-2181
Japan

2 Texas Tech University
D.L. James
Department of Mechanical Engineering
Box 41021
Lubbock, TX 79409

2 DLR
Christian Sattler
Martin Roeb
Linder Hoche
51147 Cologne
Germany

1 ETH Zurich
Aldo Steinfeld
ETH Zentrum ML-J42.1
8092 Zurich

Switzerland

1 University of Colorado
Al Weimer
Chemical Engineering Department
Boulder, CO 80309-0424

4 University of Nevada, Las Vegas
Sean Hsieh
Taide Tan
Yitung Chen
Roger Rennels
4505 Maryland Parkway, Box 4027
Las Vegas, NV 89052

2 MS0836 R.E. Hogan, 1516

1 MS1110 J.S. Nelson, 6337

8 MS1127 R.B. Diver, 6337

2 MS1127 NSTTF Technical Library, 6337

2 MS1127 T.A. Moss, 6337

2 MS1127 N.P. Siegel, 6337

1 MS1127 G.J. Kolb, 6335

2 MS1349 C. Apblett, 1815

2 MS1349 E Branson, 1815

2 MS1349 L. Evans, 1815

2 MS1349 J.E. Miller, 1815

1 MS9052 J.O. Keller, 8367

1 MS9054 D.R. Hardesty, 8360

1 MS9291 M.D Allendorf, 8324

1 MS0899 Technical Library, 9536